Model-Based Design and Experimental Validation of Multi-Domain Dynamic Energy Conversion Devices

BY

MARK ELLIOT HOFACKER

Dissertation

Submitted to the Faculty of the

Graduate School of Vanderbilt University

in partial fulfillment of the requirements

for the degree of

DOCTOR OF PHILOSOPHY

in

Mechanical Engineering

May, 2014

Nashville, Tennessee

Approved:

Dr. Eric J. Barth

Dr. Michael Goldfarb

Dr. Pietro Valdastri

Dr. Robert J. Webster III

Dr. Kenneth Pence

Acknowledgements

I would like to thank my advisor Eric Barth for giving me the opportunity to work on fascinating projects and helping me develop as an engineer. The fifth floor of Olin Hall is a place that I will fondly remember due to the unique environment created by Dr. Barth, Dr. Goldfarb, Dr. Webster, Dr. Valdastri, Dr. Withrow, Don Truex, Dr. Frampton, Dr. Sarkar, and many more. The floor is productive and enjoyable, and it has provided me with some of my closest friends. Vanderbilt University employs some of the kindest people that I have met, and I am grateful for the deep consideration of Dr. Pence, Suzanne Weiss, Myrtle Daniels, and Jean Miller.

The Laboratory for the Design and Control of Energetic Systems has an unforgettable, relaxed environment and I am fortunate to have worked with Alex Pedchenko, Chao Yong, Danny Whitney, Andy Willhite, John Tucker, Nithin Kumar, Jose Riofrio, Alia Farhana Abdul Ghaffar, James Kong, Ricardo Reina, and David Comber. They are excellent engineers, and I am glad to have known them.

I would like to thank my undergraduate advisor Dr. Korde and my internship mentor Dr. Kaul. Their joy and deep appreciation of research inspired my decision to pursue graduate school and a career in research and development. Their thoughtful approach to work and life is apparent in every conversation, paper, and email. I often consider things that they have said and I am grateful to have worked under them.

My parents have been extremely supportive of me and have encouraged me to pursue graduate school. It has been a joy to share my research with my father because of his exceptional understanding and appreciation of my work. My mother's passion as teacher has shaped the way I value a graduate education.

I owe a tremendous amount to my biological brother Peter Hofacker as well as non-biological brothers Skyler Dalley, Alex Pedchenko, Chao Yong, Kevin Ha, and Nithin Kumar. This document may not exist if not for their guidance and support. Alex and Nithin made significant contributions to many of the manuscripts in this dissertation. Working closely with them was rewarding and something that I will miss greatly when I leave Nashville. I hope to assist them in their careers as much as they have helped mine.

Finally, I would like to thank Vanessa Li for taking care of me throughout graduate school and for agreeing to marry me next summer. Her artistic skills are chiefly responsible for the more attractive figures in this document. Her generosity and kindness was felt by many in our department by hosting dinner parties, continuously providing treats, and by generally being a wonderful person.

Table of Contents

Acknowledgements ii

Table of Contents iii

List of Figures v

List of Tables ix

Chapter

1. Overview 10

Introduction 10
Background and Significance 11
Project Overview: Bridge Vibration Energy Harvester 17
Project Overview: Free Piston Engine Compressor 20
Project Overview: Controlled Stirling Thermocompressor 24
Document Organization 27
References 29

2. Experimental Research Platform for Structural Health Monitoring 32

Prologue 32
Abstract 33
I. Introduction 33
II. Derivation of Control Law 34
III. Simulation Results 38
IV. Experimental setup and results 40
V. Conclusion 45
References 45

3. Multi-Domain Impedance Matching Applied to a Bridge Vibration Energy Harvester 47

Prologue 47
Abstract 48
I. Introduction 48
II. Dynamic Model of Electromagnetic Vibration Energy Harvester 49
III. Experimental Setup 50
IV. Active Load Adjustment Control 53
V. Broad-Bandwidth Stable Controller 58
VI. Simulated Results 59
VI. Conclusions 61
References 62

4. Design and Validation of a Figure-Eight Free-Liquid-Piston Engine Compressor for Compact Robot Power 64

Prologue 64
I. Introduction 64
II. Evolution of the Device 67
III. Experimental Results 68
Acknowledgment 69
References 69

5. An Experimentally Validated Figure-Eight Free-Liquid Piston Engine Compressor 71

Prologue 71
Abstract 73

I. Introduction 73
II. Experimental Setup 76
III. Piston Inertia Considerations 77
IV. Self-Balancing Figure-Eight Liquid Piston 80
V. Check Valve 83
VI. Onboard Components 85
VII. Controller 87
VIII. Experimental results 89
IX. Conclusion 91
Acknowledgment 91
References 91

6. Dynamic Simulation and Experimental Validation of a Single Stage Thermocompressor for a Pneumatic Ankle-Foot Orthosis 95

Prologue 95
Abstract 97
Nomenclature 97
I. Introduction 98
II. Operation of Thermocompressor 101
III. Design of Thermocompressor 102
IV. Dynamic Model 106
V. Quasi-Static Model 108
VI. Experimental Results 108
VII. Predicted Performance from Dynamic Model 112
VIII. Conclusions 114
Acknowledgement 115
References 115

7. Conclusion 118

Summary 118
Contribution 118
Bridge Vibration Energy Harvester 119
Free-Piston Engine Compressor 119
Controlled Stirling Thermocompressor 120

List of Figures

Figure 1.1 – (a) Circuit diagram with a voltage source and source and load impedances and (b) equivalent bond graph 11

Figure 1.2 - Electrical circuit approximations of the bridge vibration energy harvester as Thevenin equivalent circuit, the free piston engine compressor as a buck converter, and the Stirling thermocompressor as a solid core transformer 16

Figure 1.3 - Bond graphs of the bridge vibration energy harvester, free piston engine compressor, and Stirling thermocompressor with linearized and simplified system dynamics 17

Figure 1.4 – Experimental setup photograph and schematic of bridge vibration energy harvester 18

Figure 1.5 – Power generated by harvester with different control techniques normalized to power generated by passive, resistive control 19

Figure 1.6 – Predicted power generated by active controlled harvester with varying levels of regeneration efficiency in response to an acceleration profile compared to passive control and ideal, unstable control 20

Figure 1.7 – Free piston engine compressors for compact rescue crawler a) first generation b) second generation c) third generation 21

Figure 1.8 - Schematic of free piston engine compressor at effective top dead center 21

Figure 1.9 - Schematic of free piston engine compressor at effective bottom dead center 22

Figure 1.10 – Compressor head pressure and command signals for a single combustion and exhaust event 23

Figure 1.11 - Pressure inside compressor head and reservoir during operation 23

Figure 1.12 - Schematic illustrating the operation of single-stage Stirling thermocompressor 24

Figure 1.13 - CAD drawing of piston-motor assembly 25

Figure 1.14 – Prototype Stirling thermocompressor without heat exchangers or electric heaters 25

Figure 1.15 - Schematic of heat exchanger operation at bottom dead center (left) and top dead center (right) 26

Figure 1.16 - Collapsible, in-piston heat exchangers used in hot side (left) and cold side (right) 26

Figure 1.17 - Cold chamber pressure from experimental data and different models for 2.8 Hz operation and 600°C heater head temperature 27

Figure 2.i - Electrical circuit approximation of the bridge vibration energy harvester 32

Figure 2.1 - Transformation of bridge energy harvester into electrical domain: i) mechanical representation; ii) bond graph representation; iii) electrical equivalent of bond graph; iv) Thevenin equivalent circuit 35

Figure 2.2 - Electrical circuit (i) and mechanical system (ii) representations of ideal energy harvester behavior 37

Figure 2.3 - Position response of several passive, tuned, energy harvesters and the controlled impedance matched energy harvester to a force input 38

Figure 2.4 - The power generated by passive and controlled harvesters vs. frequency 39

Figure 2.5 - Passive and controlled responses of the energy harvester to a force input 40

Figure 2.6 - Experimental setup photograph and schematic 41

Figure 2.7 - Transformation of prototype harvester into electrical domain: i) mechanical representation; ii) bond graph representation; iii) electrical equivalent of bond graph; iv) Thevenin equivalent circuit..... 42

Figure 2.8 - Experimental magnitude response of controlled harvester mass to vibrations compared to the response of passive harvester and the ideal response of a controlled harvester..... 43

Figure 2.9 - Experimental phase response of controlled harvester mass to vibrations compared to the response of passive harvester and the ideal response of a controlled harvester..... 44

Figure 2.10 - Experimental response of harvester mass to vibrations with and without active control..... 44

Figure 3.i – Electrical circuit approximation of the bridge vibration energy harvester with electrical and mechanical components..... 47

Figure 3.1 – Lumped parameter representation of a vibration energy harvester's components: i) mechanical components; ii) electrical components..... 50

Figure 3.3 – Electromagnetic vibrational energy harvester experimental setup..... 51

Figure 3.4 – Photograph of top portion of the vibrational energy harvester..... 52

Figure 3.5 – Bode plot of the relationship between input excitation displacement and the relative position of the proof mass..... 53

Figure 3.6 – Circuit with a voltage source and a load and source impedance..... 54

Figure 3.6 – Thévenin equivalent circuit representation of harvester..... 55

Figure 3.7 – Frequency-dependent behaviors of the power maximizing load based on the complex conjugate of the source impedance ($\boldsymbol{Zload, ideal}$) and based on maximizing (17) denoted as "Derived $\boldsymbol{Zload}$"..... 58

Figure 3.8 – Power generated by harvester with different control techniques normalized to power generated by passive, resistive control..... 60

Figure 3.9 – Predicted power generated by active controlled harvester with varying levels of regeneration efficiency in response to an acceleration profile compared to passive control and ideal, unstable control..... 61

Figure 4.i – Electrical circuit approximation of the free piston engine compressor as a buck converter..... 64

Figure 4.1 - Schematic of the FPEC at (a) effective TDC, and (b) effective BDC..... 66

Figure 4.2 - (a) Compressor head while pumping (b) Compressor head at BDC (c) Compressor head during breathe-in..... 67

Figure 4.3 - a) Straight Configuration, b) Loop Configuration, c) Figure-8 Configuration. (a, b and c not to scale relative to each other)..... 67

Figure 4.4 - Schematic of the FPEC represented energetically as a buck converter..... 68

Figure 5.i – Electrical circuit approximation of the free-piston engine compressor as a buck converter..... 71

Figure 5.1 - Picture of Free Piston Compressor Engine with figure-8 high inertance liquid piston and onboard electronics and control..... 76

Figure 5.2 - Schematic [37] of free piston engine compressor at effective top dead center showing relaxed elastomers, a small combustion chamber, and a pump chamber with atmospheric air..... 76

Figure 5.3 - Schematic [37] of free piston engine compressor at effective Bottom Dead Center with elastomers fully stretched, a fully expanded combustion chamber, and an emptied pump chamber 77
Figure 5.4 - (a) Compressor head while pumping (b) Compressor head at BDC (c) Compressor head during breathe-in [37]..... 77
Figure 5.5 - Schematic of the free-piston engine compressor represented as circuit diagram of a buck converter..... 78
Figure 5.6 - Schematic [38] of liquid piston with converging and diverging nozzles and diaphragms on both ends 79
Figure 5.7 - a) Straight Configuration b) Loop Configuration c) Figure-8 Configuration 80
Figure 5.8 - Force exerted on engine support due to fluid motion during combustion and piston expansion 82
Figure 5.9 - (a) Previous Compressor Head Check Valve (b) Current Compressor Head Check Valve..... 84
Figure 5.10 - Picture of Compressor Head 85
Figure 5.11 - a) On Board Electronics b) Athena Single Board Microprocessor 86
Figure 5.12 - a) Injector Manifold with Integrated Actively Regulated Propane Buffer Tank b) Exhaust Solenoid 87
Figure. 5.13 - Reservoir pressure and command signals for a single combustion and exhaust event..... 88
Figure 5.14 - Pressure inside compressor head and reservoir during run 1 89
Figure 5.15 - Pressure inside compressor head and reservoir during run 2 89
Figure 5.16 - Pressure inside compressor head and reservoir during runs 3 and 4 90
Figure 6.i – Electrical circuit approximation of the Stirling thermocompressor as a solid core transformer 95
Figure 6.1 - Schematic illustrating the operation of single-stage thermocompressor 102
Figure 6.2 - Mass-temperature and temperature-entropy diagrams of Stirling thermocompressor operation..... 102
Figure 6.3 - CAD drawing of piston-motor assembly..... 103
Figure 6.4 - Cross section of thermocompressor showing internal components 104
Figure 6.5 - Schematic of heat exchanger operation at BDC (left) and TDC (right)..... 105
Figure 6.6 - Collapsible, in-piston heat exchangers used in hot side (Left) and cold side (right) 105
Figure 6.7 - Prototype thermocompressor without heat exchangers 106
Figure 6.8 - Cold chamber pressure from experimental data and different models for 2.8 Hz operation and 600°C heater head temperature 109
Figure 6.9 - Cold chamber pressure from experimental data and different models for 2.8 Hz operation and 600°C heater head with no heat exchangers present.....110
Figure 6.10 - Cold chamber pressure from experimental data at different operational frequencies and different models with heat exchangers 111
Figure 6.11 - Cold chamber pressure from experimental data at different operational frequencies and different models without heat exchangers 112
Figure 6.12 - Pressure increase from atmosphere for different heat transfer rates and

operational frequency.....113

Figure 6.13 - Pneumatic power delivered as a function of the ratio of reservoir pressure (pumping pressure) to the low presure of the engine (suction pressure), for different heat transfer rates and operational frequencies.....114

List of Tables

Table 1.1 – Criteria to satisfy various impedance matching techniques 12

Table 1.2 - Bridge vibration energy harvester, free piston engine compressor, and Stirling thermocompressor with primary dynamics separated by type and dominant energetic domains 15

Table 3.1 – Vibration Energy Harvester Parameters 52

Table 4.1 - Reactions for various liquid piston configurations 68

Table 5.1 - External Effects for Various Liquid Piston Configurations 82

Table 5.2 - Efficiency, power, and pressure for reservoir pressure for the runs presented in this paper 90

Table 6.1 - Values of significant parameters 107

1. Overview

Introduction

The delivery of power can be greatly enhanced by properly matching an energetic source to its intended destination. With dynamic, nonlinear systems, it is often not intuitive what the appropriate load should be to maximize properties such as efficiency or power. Furthermore, it is not always clear which components and phenomena constitute sources and loads. The matching of sources to loads is known as impedance matching and has been explored in electronics with techniques such as power factor correction and the maximum power transfer theorem. This dissertation demonstrates the application of impedance matching to three different, multi-domain, dynamic systems.

The first application of this framework is the control of a bridge vibration energy harvester. A novel prototype device was constructed and fully instrumented using an optical encoder, accelerometer and linear motor. An unstable, canonical controller that harvests the maximum power at every frequency was developed using the maximum power transfer theorem. A stable controller was developed that approximates this ideal behavior in the frequency range of interest and simulated results are presented.

The second application of this approach is the design and control of a free-piston engine compressor. The design, construction, and operation of this device is described in a model-based context and experimental data is presented. The engine-compressor is a novel configuration that combines a free-piston engine with an air compressor. This device includes a liquid piston trapped between elastomeric diaphragms, controlled air and fuel injection valves, and high-speed check valves. Impedance matching considerations were applied to a) the liquid piston's inertance and configuration, b) the check valve of the compressor section of the engine-compressor, and c) the controller that governs the timings of the valves and the spark. The necessity to increase piston inertia was discovered through circuit analysis. The advantages of the check valve's dynamics and the figure-8 piston configuration are proven mathematically.

The third application describes a controlled Stirling thermocompressor intended as a mobile power supply that utilizes a high energy-density source of heat and produces high pressure air for use in pneumatic components. An experimental apparatus was constructed using a reciprocating lead screw to move the displacer piston, and novel in-cylinder heat exchangers. It is shown that the heat exchangers lead to increased power production by increasing the rate of heat transfer. A model-based consideration of the system shows maximum power is produced at a particular frequency of operation for a given output pressure.

This dissertation has two primary goals. The first goal is to present the unique designs and control schemes of three energy conversion devices. The second goal of this dissertation is to cast widely different energy conversion devices into a common impedance matching framework such that lessons learned from the three applications considered in this dissertation can be applied to future devices. This

approach is meant to be general enough so that insight regarding other energy conversion devices can be gained even though they may be quite different in terms of their dynamics, energy domains, or energy transduction mechanisms. A bond graph and circuit equivalent of each device is presented, with the components separated into power sources, source impedances, and load impedances. The energetic bottlenecks are identified, and the design and control steps needed to mitigate the bottlenecks by modifying the dynamics of the source and/or load, are discussed.

Background and Significance

In electronics, impedance matching is used to accomplish a variety of goals when pairing a source of power or a signal source with a destination load or signal receiver. The schematics below in Figure 1.1 will aid in the description of several impedance matching techniques. The two impedances (Z_S and Z_L) consist of resistive, dissipative components (R_S and R_L), capacitive components (C_S and C_L), and inductive components (L_S and L_C). The capacitive and inductive components are energetically conservative elements and are referred to collectively as reactive components (X_S and X_L). Reactive elements comprise the load's complex impedance and are therefore frequency dependent. The series configuration of the source and load in the figure is merely representative and could more generally be of any dynamic order or include nonlinear elements.

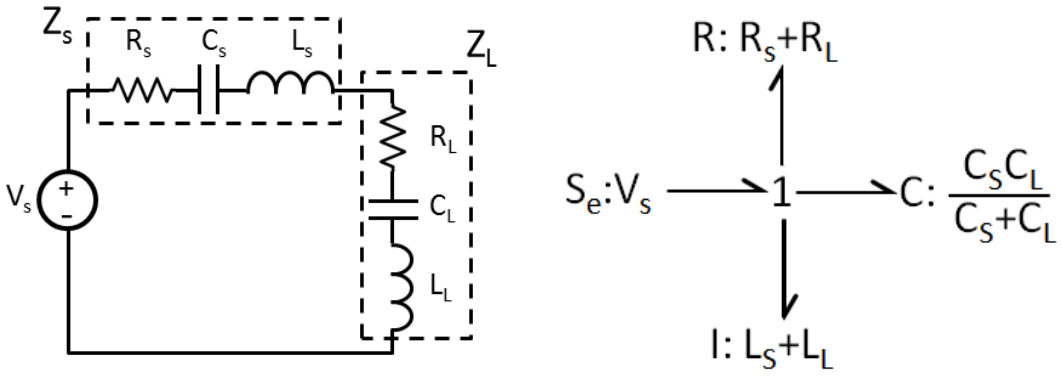

Figure 1.1 – (a) Circuit diagram with a voltage source and source and load impedances and (b) equivalent bond graph

Four common goals of impedance matching are impedance bridging, minimizing reflection, maximizing power transfer, and power factor correction. To accomplish impedance bridging, the load impedance of the source is set much higher than that of the load to minimize the current drawn and maximize the voltage drop across the load. This is useful in microphones because increasing the voltage drop also increases the signal level. Minimizing reflection refers to the practice of minimizing the amount of power that is sent back to the source from the load. When minimizing reflection, the source and load impedance are made purely resistive and set equal to each other. Maximizing power transfer through the load requires setting the load impedance equal to the complex conjugate of the source impedance to

satisfy the maximum power transfer theorem (MPTT). Power factor correction is concerned with matching the phase of the source voltage with that of the load current so that power transfer to the load is maximized while current is minimized. This is achieved through a variety of means, but in its simplest implementation the load reactance (the capacitive and inductive impedance) is set to have the opposite sign of the source reactance. Minimizing reflections, applying the maximum power transfer theorem and power factor correction are similar in that they reduce the amount of power reflected back to the source. A brief summary of these techniques is shown below in Table 1.1.

Table 1.1 – Criteria to satisfy various impedance matching techniques

Impedance Matching Technique	Criteria
Impedance Bridging	$Z_L >> Z_S$
Minimize Reflections	$R_S=R_L, X_S=X_L=0$
Maximum Power Transfer Theorem	$Z_S=Z_L^*$
Power Factor Correction	$X_S=-X_L$

This dissertation is primarily concerned with the maximum power transfer theorem and power factor correction. A derivation of the maximum power transfer theorem will aid in understanding this work. The maximum power transfer theorem can be quickly derived by calculating the power dissipated by the load ,R_L, given a sinusoidal voltage input to the circuit of Figure 1.1 as shown in Equation 1. In this equation, I represents the current through the circuit, and P_L represents the power dissipated by R_L .

$$P_L = {I_{rms}}^2 R_L = \frac{1}{2}|I|^2 R_L = \frac{1}{2}\left(\frac{|V_S|}{|Z_S+Z_L|}\right)^2 R_L = \frac{1}{2}\left(\frac{|V_S|^2}{(R_S+R_L)^2+(X_S+X_L)^2}\right) R_L \quad (1)$$

By inspection, it is clear that the power can be maximized by setting the sum of the reactive impedances to zero ($X_L = -X_S$). It is possible for the terms to cancel each other because the two reactive elements have opposite signs; capacitance presents negative impedance while the inductance presents positive impedance as demonstrated in Equation 2.

$$X_S + X_L = L_S j\omega - \frac{j}{C_s\omega} + L_L j\omega - \frac{j}{C_L\omega} = \left((L_S + L_L)\omega - \frac{C_L+C_S}{C_L C_S \omega}\right) j \quad (2)$$

In this equation, ω represents the frequency of the current flowing through the components which is necessarily equal to the frequency of the voltage source. By setting the sum of the complex impedance to zero and solving for ω, it can be seen that the complex impedance equals zero only when the natural frequency, ω_n, of the circuit matches the frequency of the voltage source ω. This observation is demonstrated below in Equation 3.

$$\omega_n = \sqrt{\frac{C_L+C_S}{(L_S+L_S)C_L C_S}} = \sqrt{\frac{1}{(L_S+L_S)\frac{C_L C_S}{C_L+C_S}}} = \sqrt{\frac{1}{L_{equiv}C_{equiv}}} \quad (3)$$

If the frequency of the source is fixed, the natural frequency of the circuit can be modified by changing the reactive elements of the load (C_L and L_L). At the natural frequency of the system, the inductive and capacitive elements mathematically cancel each other, and physically exchanging energy with each other without sending power back to the source. By matching the systems natural frequency to the source frequency and therefore eliminating the reactance, Equation 1 can be rewritten as shown below in Equation 4:

$$P_L = \frac{1}{2}\left(\frac{|V_s|^2}{\frac{{R_S}^2}{R_L}+2R_S+R_L}\right) \quad (4)$$

Power can then be maximized by minimizing the denominator of Equation 4. Differentiating the denominator with respect to the load resistance shows that maximum power is achieved by setting the load resistance equal to the source resistance($R_L = R_S$). It can be observed that the conditions $R_L = R_S$ and $X_L = -X_S$ are both true if and only if $Z_L = \mathrm{Z_s}^*$ where both the load and source impedance are of the form:

$$Z = R + \left(L\omega - \frac{1}{C\omega}\right)j \quad (5)$$

The efficiency of the circuit is a ratio of the power dissipated by the load and the total power dissipated as shown in Equation 6. With equal source and load resistances, a circuit that fulfills the maximum power transfer theorem necessarily has an efficiency of 50%. This is an important distinction from power factor correction, which does not specify efficiency.

$$\eta = \frac{R_L}{R_S+R_L} \quad (6)$$

The power factor is defined as the ratio of active power (P) and apparent power (S). Active power is the power delivered to the load. Apparent power is the power available from the source. These are not always equivalent because power delivered from the source can be stored in reactive elements, this stored power is known as reactive power (Q). With a sinusoidal voltage supply, the active power, apparent power, and reactive power are related as follows:

$$S^2 = P^2 + Q^2 \quad (7)$$

Reactive power is stored in reactive elements, transferred between reactive elements, and reflected

back to the source. During the transfer to the source, it undergoes otherwise unnecessary parasitic line losses as the reactive power moves through the source resistance. Power factor correction is therefore concerned with reducing the reactive power. Achieving a higher power factor is therefore beneficial in two ways - more power is delivered to the load and it is delivered more efficiently. With a unity power factor, the maximum amount of power is delivered for a given efficiency.

There are a number of methods for maximizing power factor. One method is matching the phase of the real power to that of the apparent power which results in power only flowing out of the source. The relationship between the real power, and apparent power can be expressed as a function of the phase between them, φ, as shown in Equation 8.

$$|P| = |S| \cos \varphi \tag{8}$$

Minimizing the phase angle can be achieved in design or through active control depending on the application. During the design phase, passive elements such as inductors can be selected to match predicted operating conditions [1]. Closed loop control techniques such as feedback linearization, PI, and PID are used to control active elements such as buck-boost converters which minimize the phase angle [2-4]. Some active systems identify the frequency of the incoming energy and modify system parameters to alter the device's natural frequency [5].

Some techniques utilize a discrete phase-locked loop [6, 7]. A phase-locked loop is a control loop which matches frequencies with the help of a variable frequency oscillator and a phase detector. It adjusts the frequency of the oscillator until its phase matches that of the input so that the output of the oscillator matches the frequency of the input. The drawback of determining the frequency in order minimize phase angle is that there is an inherent delay in this approach and multiple frequencies cannot be considered simultaneously.

In other work, when this ideal operating behavior is difficult to define, parametric analysis is used to find ideal operating conditions [1, 8, 9]. In these studies, a variable such as switching frequency or a closed loop scaling factor was varied and an ideal operating point was chosen. It is necessary to create these controllers based upon parametric studies because many of the devices they are applied to use highly non-linear components such as switching DC-DC converters [2, 5, 8, 10, 11]; these components are often difficult to model linearly and are difficult to make analytical calculations with. This dissertation does not consider detailed, non-linear components; the novelty and contribution of this work is to present a more unifying impedance matching framework to multi-domain energetic devices. In turn, the work seeks to describe how this framework can benefit the control and design of such multi-domain energetic devices.

There is a large body of work that describes multi-domain impedance matching in systems that contain dominant thermal components [12-14]. Apertat showed how thermal impedance was applied to the interface of a thermoelectric generator and a non-ideal heat exchanger in an attempt to approximate Carnot efficiency [12]. Tijani describes an effort to match the impedance between a mechanical resonator

and a thermoacoustic Stirling engine [15]. Lossec studied the conversion of thermal energy from a human body through thermo-electric converters to its electrical destination [13]. These works are similar in nature to the work presented in this dissertation, but the components are not separated into energetic sources, source impedances, and load impedances.

Active impedance matching considerations are often applied to RF circuitry. Although there are conceptual similarities to this work, it is different because noise is a primary concern which often conflicts with the transmission of power [16]. Work related to actively matching impedances in RF circuits most often focuses detailed on electronic design [17, 18], and is therefore not directly applicable to the design of devices that contain significant mechanical or thermal components.

Without a common language to describe design and control goals, it is difficult to apply the approach used on one project to another. By describing three different energy conversion devices with a common framework, it can be seen how these projects can be logically separated into common components and addressed. In the case of the harvester, the source impedance dictated the physical design and the load impedance dictated the control design. In the case of the free piston engine-compressor, the load impedance was fixed as the compression and pumping of air and a consideration of both, the energetic source and the source impedance, dictated the physical design and control of the engine-compressor. In the case of the Stirling thermocompressor, the source and load impedances had few design degrees of freedom but a consideration of their interaction dictated the correct frequency of the energetic source. This separation of components for the three projects into an energetic source, carrier (or source impedance), and destination (or load impedance) is shown in Table 1.2.

Table 1.2 - Bridge vibration energy harvester, free piston engine compressor, and Stirling thermocompressor with primary dynamics separated by type and dominant energetic domains

	Bridge Vibration Energy Harvester	**Free Piston Engine Compressor**	**Thermocompressor**
Source	Bridge Vibration	Injection / Combustion / Exhaust	Heater Head / Displacer
Domain	Mechanical	Chemical / Thermal	Thermal
Carrier / Source Impedance	Sprung Mass / Coil Inductance	Combustion Products / Liquid Piston / Pump Chamber Air	Heat Exchangers / Working Fluid
Domain	Electro-Mechanical	Pneumatic / Mechanical / Pneumatic	Thermal / Pneumatic
Destination / Load Impedance	Load Impedance	Reservoir	Reservoir
Domain	Electrical	Pneumatic	Pneumatic

All three projects can be represented as multi-domain, Thevenin type circuits with an exogenous energy source, a source impedance containing components that dissipate (resistive) and temporarily store energy (reactive), and a destination or load impedance also containing reactive and resistive elements to which the energy is delivered. A circuit representation of each system is shown in Figure 1.2.

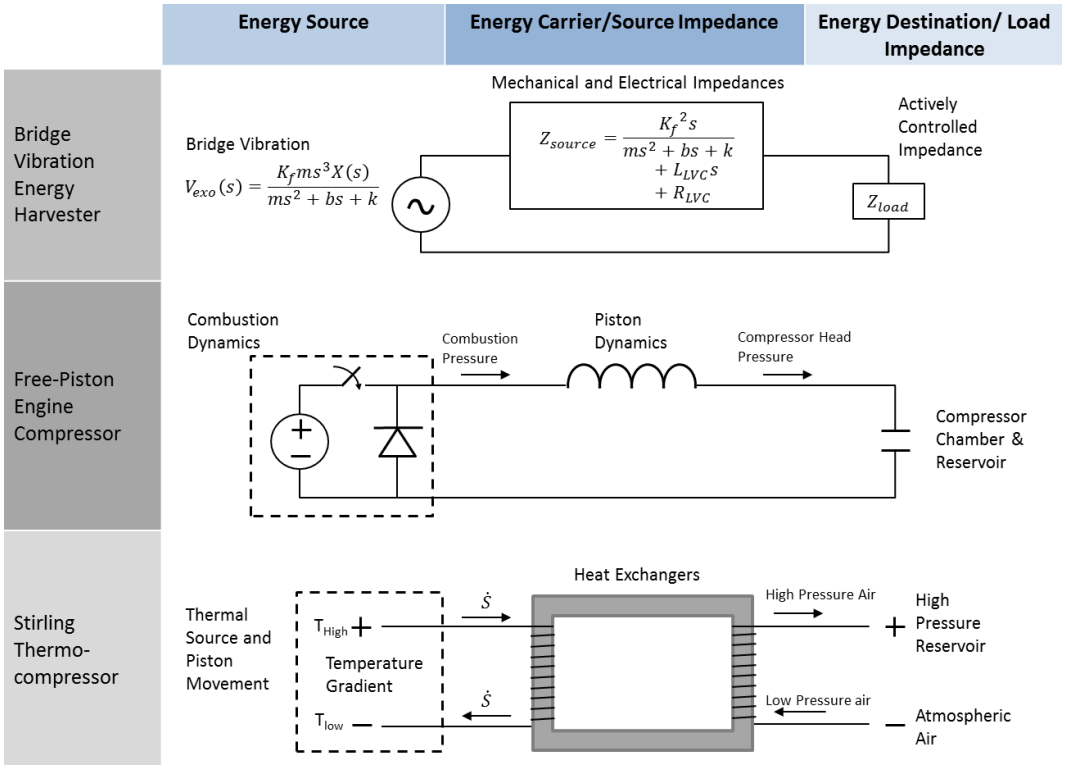

Figure 1.2 - Electrical circuit approximations of the bridge vibration energy harvester as Thevenin equivalent circuit, the free piston engine compressor as a buck converter, and the Stirling thermocompressor as a solid core transformer

In this representation, the major conceptual similarities and differences between the projects become clear. All three sources are analogous to a fluctuating voltage sources from which energy is extracted. With all three projects, the outputs of these energetic sources was increased through design and/or control decisions. With the bridge vibration energy harvester, the energy source contained reflected mechanical elements and was maximized through the minimization of mechanical damping and through the maximization of the proof mass. With the free piston engine-compressor, the energetic source was made periodic via the control of the air/fuel injectors, spark and exhaust valve. The energy from combustion delivered to the load was increased by manipulating the inertance of the source impedance to increase compression and present a loading profile that allowed a large expansion ratio and matched the load impedance. With the Stirling thermocompressor, the energy extracted from the thermal gradient was maximized through actively controlling the displacer piston and through the addition of in-cylinder heat exchangers.

Major bottlenecks in all three systems were found at the points where energy is transferred across domains. For instance, with both the Stirling thermocompressor and the free piston engine compressor the transfer of energy from the thermal/chemical domain to the pneumatic domain was a major difficulty which required unique design solutions. Both the bridge vibration energy harvester and the Stirling thermocompressor have an interface between the electrical and mechanical domains. In both of these

devices, transferring energy to the mechanical domain was a necessary parasitic loss that needed to be minimized to make these projects practical.

To illustrate the cross domain energy transfer a bond graph of each system was created. Although converting the system dynamics into bond graph form required linearization and simplification of complex dynamics, this form is useful because the barriers to fast and efficient energy transfer can be quickly identified. Bond graphs showing the overall energy transfer goals and major components of each project are shown in Figure 1.3.

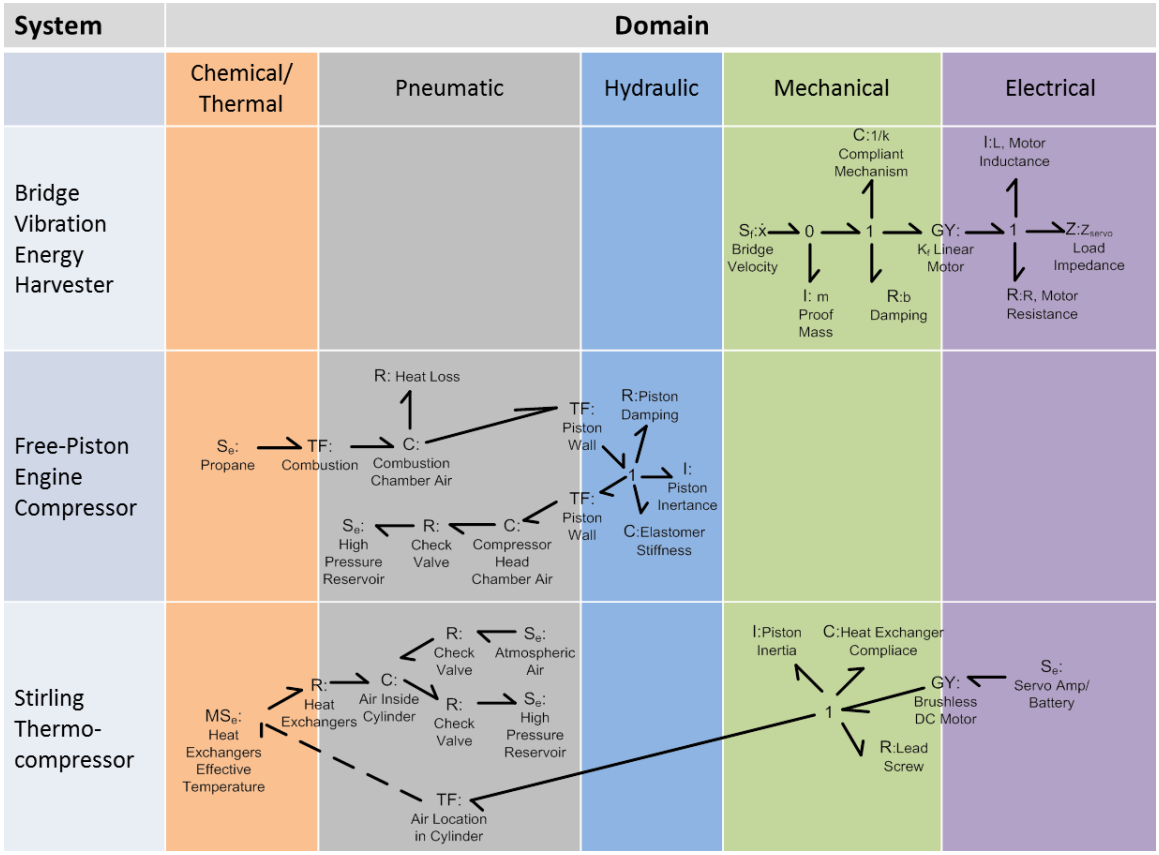

Figure 1.3 - Bond graphs of the bridge vibration energy harvester, free piston engine compressor, and Stirling thermocompressor with linearized and simplified system dynamics

The design and control decisions used to address the intra-domain and inter-domain energy transfer are discussed in the following project overviews and in more detail in the ensuing manuscripts.

Project Overview: Bridge Vibration Energy Harvester

The first system addressed with this framework is an electromagnetic bridge vibration energy harvester meant to be an untethered power supply to bridge health monitoring equipment. In this class of harvester, a proof mass is connected to a bridge with a spring, and a damping element serves to harvest energy. The amount of power available from bridge vibration is usually in the milliwatt range, so it is

important to minimize parasitic losses. With this consideration, the prototype shown in Figure 1.4 was designed to minimize friction by eliminating bearing surfaces. This was achieved by combining the spring and alignment elements into a series of compliant structures.

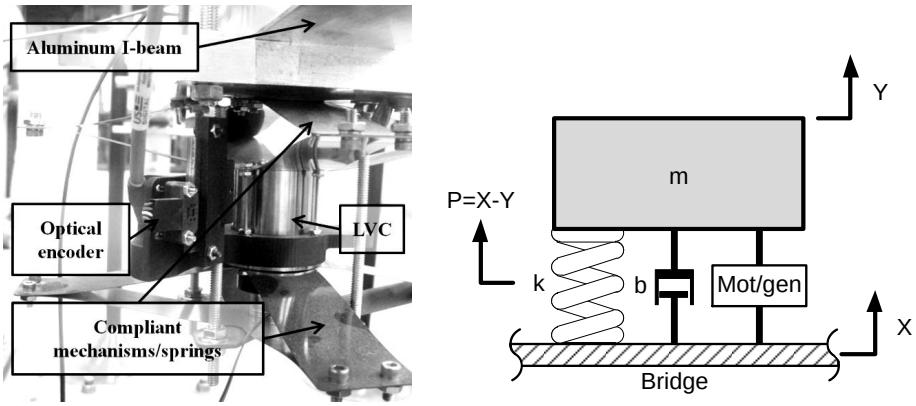

Figure 1.4 – Experimental setup photograph and schematic of bridge vibration energy harvester

Bridges' dominant modes of oscillation are typically in the range of 3-12 Hz. The width, length, and thickness of the compliant mechanisms were designed so that the harvester would have a natural frequency of 8.0 Hz so that energy could be captured from the more energetic, higher frequencies in the range of interest. To aid in testing and active control, there is an optical encoder to measure the movement of the linear motor relative to the bridge and an accelerometer to measure the movement of the bridge itself. The harvester is mounted to an aluminum I-beam that is actuated by an electromagnetic shaker, which simulates bridge vibration.

A linear motor was implemented as both a motor and a generator so that the harvester could be actively controlled to alter the load impedance. Active control was necessary because conventional, passive harvesters only harvest appreciable power at their mechanical natural frequency. This is because the power harvested is proportional to the velocity of the proof mass and an appreciable velocity only occurs when the bridge oscillates at the natural frequency of the mass spring damper system. Only extracting power in a narrow frequency range is a considerable obstacle of passive harvesters because different bridges oscillate at different frequencies, the same bridge will oscillate at different frequencies at different times, and bridge oscillations often contain multiple frequencies. Using active control modifies the load impedance and allows for energy harvesting at frequencies other than a narrow band around the natural frequency.

Work on the bridge vibration energy harvester described in this document demonstrates how satisfying the maximum power transfer theorem increased net energy yield. This was accomplished by determining the ideal loading and then using a closed-loop controller to augment the harvester's dynamic behavior so that this ideal loading could be achieved or approximated.

A detailed analysis that includes the electrical dynamics of the harvester reveals that the ideal load impedance determined using the maximum power transfer theorem results in an unstable closed-loop system. To overcome this challenge, a load impedance that approximates the ideal load was found

through constrained optimization to yield a closed-loop stable system. To the best of the author's knowledge, this approach has not been reported in the literature. Brafau applies a similar technique by attempting to passively cancel the complex impedances of a bridge vibration energy harvester [19]. This is similar to the approach described in this dissertation, but differs because the cancelation is passive instead of active.

The power generated by the harvester utilizing the load (which can be viewed as a stable active controller) is normalized with respect to the power generated using the conventional approach of a passive, tuned load. Additionally, the proposed control scheme's power generation is compared to the power that would be generated by the upper bound of the unstable, ideal controller if it was implementable. This comparison is depicted in Figure 1.5.

It's important to note that the effectiveness of the active controller to surpass the power generation yield of the traditional passively tuned approach is dependent on the regenerative efficiency of the servo amplifier and the capacitor bank. That is to say that in comparing the passive load impedance case to active control, it is important to note that whereas power flows from the harvester to the load in both cases, power flows from the load to the harvester only during active control. Therefore the actively controlled case is adversely affected by an associated efficiency of regeneration, but the passive case is not. In comparing the performance of the active case to the passive in Figure 1.5, regeneration efficiencies were applied only when power was flowing from the load to the harvester during control.

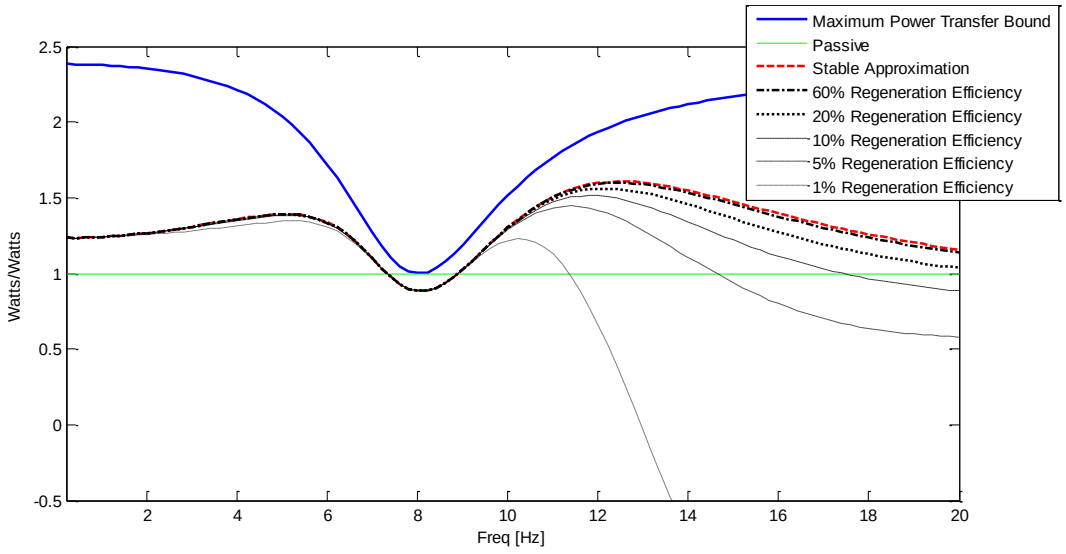

Figure 1.5 – Power generated by harvester with different control techniques normalized to power generated by passive, resistive control

To further demonstrate the benefits of this controller, the harvester's response to realistic bridge vibrations was simulated. Data recorded from an accelerometer on a real bridge was used to create a representative acceleration profile. This profile contained appreciable frequency components at 5, 7, 12, and 20 Hz. The predicted power generation results are shown in Figure 1.6. As in Figure 1.5, the power

generated for varying levels of regeneration efficiency is shown for the proposed control law case.

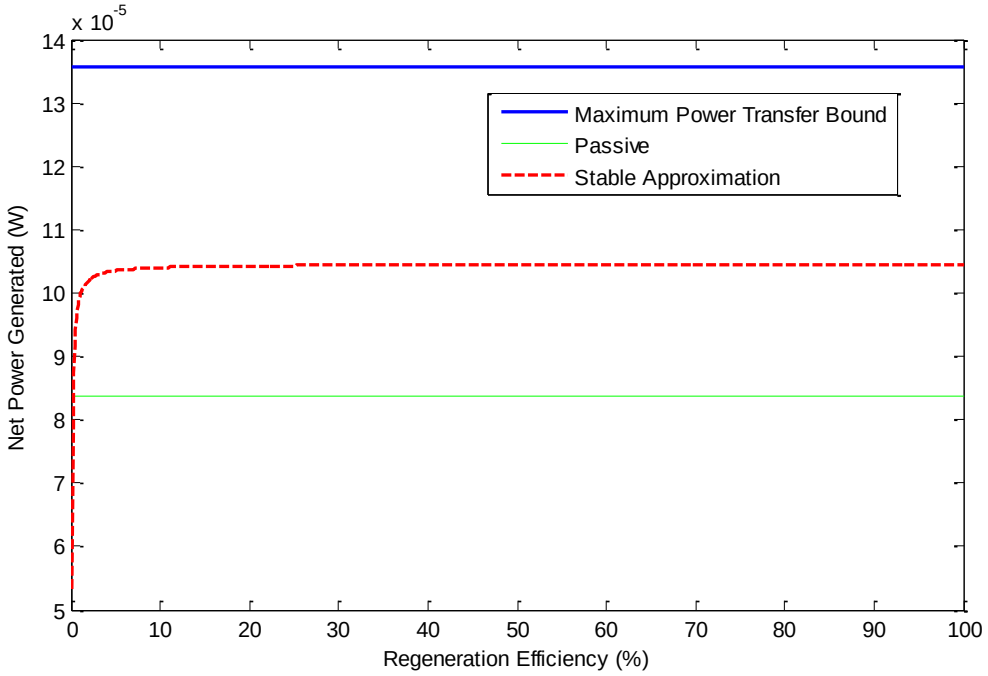

Figure 1.6 – Predicted power generated by active controlled harvester with varying levels of regeneration efficiency in response to an acceleration profile compared to passive control and ideal, unstable control

It can be seen from Figure 1.6 that even at single digit regeneration efficiencies, the proposed active control law surpasses the power generation of the harvester using the conventional passive tuned load approach.

Project Overview: Free Piston Engine Compressor

A free piston engine compressor was designed and constructed. Functionally similar to the device constructed by Willhite [20], the free piston engine compressor described in this document is a continuation of work done by Willhite, Yong, and Riofrio [20-22] in creating an internal combustion, single cylinder, free piston engine compressor. The free piston engine compressor has progressed through three distinct prototypes as shown in Figure 1.7. New developments in the current prototype, shown in Figure 1.7 c, include a self-balancing figure-8 configuration, a high efficiency compressor head, and on board control and electronics.

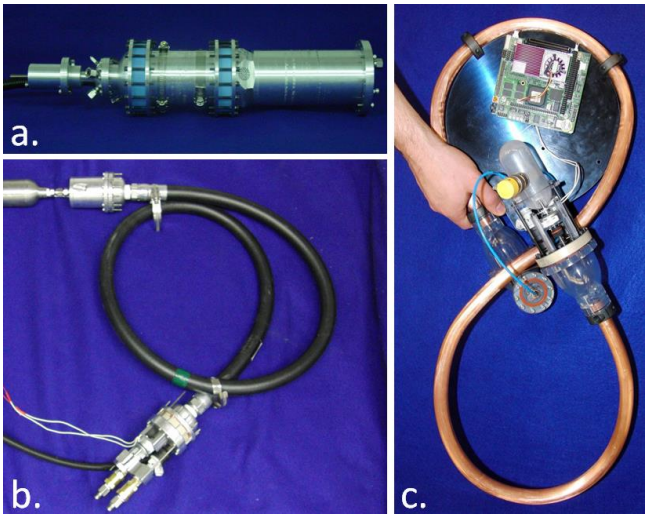

Figure 1.7 – Free piston engine compressors for compact rescue crawler a) first generation b) second generation c) third generation

The engine compressor operates on an “inject and fire” cycle that differs from the 2-stroke and 4-stroke cycles used by many internal combustion engines. Although there are only 2 strokes in the cycle, intake, compression, and expansion are combined into one stroke while the second stroke is used only for exhaust. This operation is made possible by the inclusion of a pressure reservoir to provide compressed air, a compressed fuel source, and a free piston with significant inertia. The free piston in this engine is comprised of water trapped between two elastic membranes. The term “free piston” refers to an engine in which the piston is not kinematically constrained and can therefore respond dynamically to pressure forces.

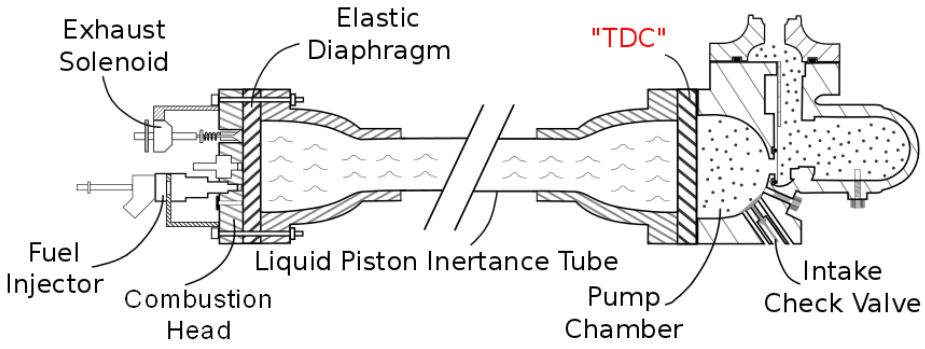

Figure 1.8 - Schematic of free piston engine compressor at effective top dead center

In the first stroke, compressed air from the reservoir and propane from the buffer tank (shown in Figure 1.8) are injected into the combustion chamber. The combustion chamber is the volume that is bound on one side by a face of the free piston and on the other side by the aluminum combustion head. The “piston” consists of a section of water trapped between elastic diaphragms. Compression is dynamically maintained during injection because the inertia of the piston prevents the piston from moving

quickly when the combustion chamber is pressurized. Immediately following injection, a spark plug ignites the air/fuel combination. Combustion forces the piston to move which in turn forces the air contained in the compressor head into the reservoir chamber.

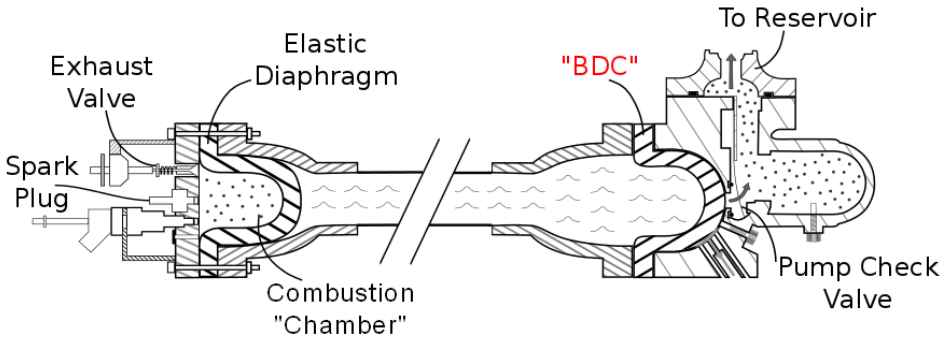

Figure 1.9 - Schematic of free piston engine compressor at effective bottom dead center

When the combustion products are fully expanded, an exhaust valve on the combustion head opens, and the second stroke begins as the elasticity of the membranes returns the piston back to its original location. The compressor head's outlet check valve closes and atmospheric air breathes in through another check valve to refill the chamber. The combustion products are expelled from the combustion head through the open exhaust valve and the second stroke concludes with the closing of the exhaust valve.

The free piston engine compressor was difficult to operate for extended periods of time, so the injection and exhaust timings could not be optimized. Nevertheless, consistent combustion was achieved through the use of a closed loop controller that modifies injection, spark, and exhaust timing through estimating the position of the liquid piston. The pressure in the compressor head is shown in Figure 1.10 overlaid with command signals given by the controller.

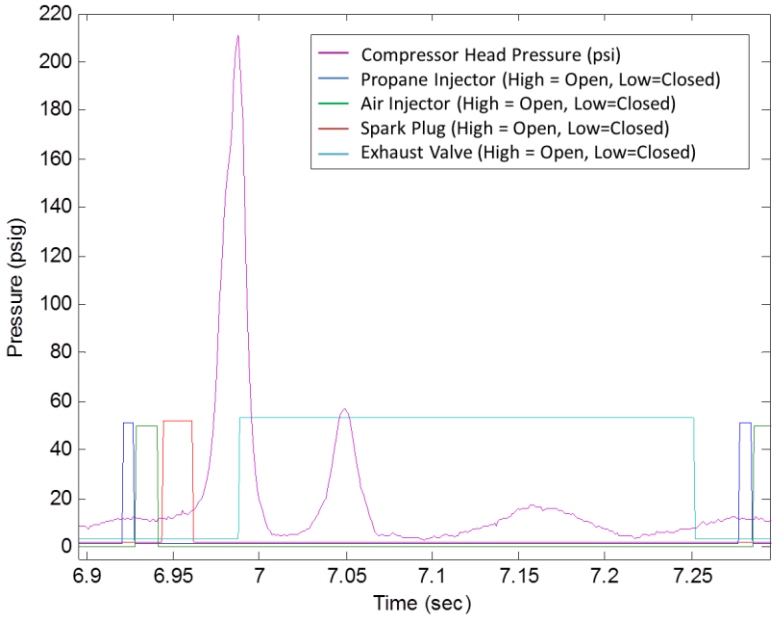

Figure 1.10 – Compressor head pressure and command signals for a single combustion and exhaust event

The reservoir pressure and compressor head pressure are shown in Figure 1.11 during a run that contained a misfire. This run is shown to demonstrate that without consistent combustion, pressure inside the reservoir head decreases because air is used for injection but none is delivered to the reservoir.

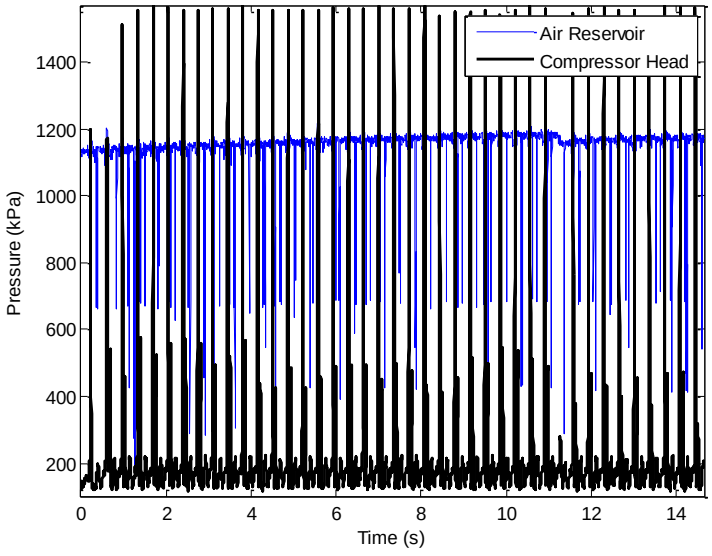

Figure 1.11 - Pressure inside compressor head and reservoir during operation

Through design improvements, the engine compressor was able to increase the pressure of a reservoir to 1187 kPa (157 psig), which is 60% higher than that of previous iterations of this device.

Project Overview: Controlled Stirling Thermocompressor

A prototype miniature Stirling thermocompressor was designed, constructed, modeled, and experimentally validated. The thermocompressor is intended to serve as a compact and quiet, untethered 50 W, pneumatic power supply for an ankle foot orthosis. Ankle-foot orthosis (AFOs) function as gait assisting devices for individuals suffering from ankle impairment.

A thermocompressor directly uses thermal energy of a heat source to increase the pressure of its working fluid, without any mechanical work output (such as conventional IC engines powering a compressor). By storing the output of the thermocompressor in a high-pressure reservoir, this power supply and storage system would potentially extend the operating time of the AFO by converting thermal energy of a high energy density hydrocarbon fuel source to pneumatic energy in the form of high-pressure air.

The proposed Stirling thermocompressor shuttles air between its heat source and a room temperature heat sink using a displacer piston. This cyclical of heating and cooling of the working fluid results in the conversion of thermal energy to pneumatic energy. As the working fluid is exposed to the heat source, its temperature and pressure increases and conversely, they decrease when the piston moves the air closer to the heat sink. Check valves enable the transfer of atmospheric air into the thermocompressor and out of the thermocompressor into the high pressure reservoir. Figure 1.12 illustrates this process.

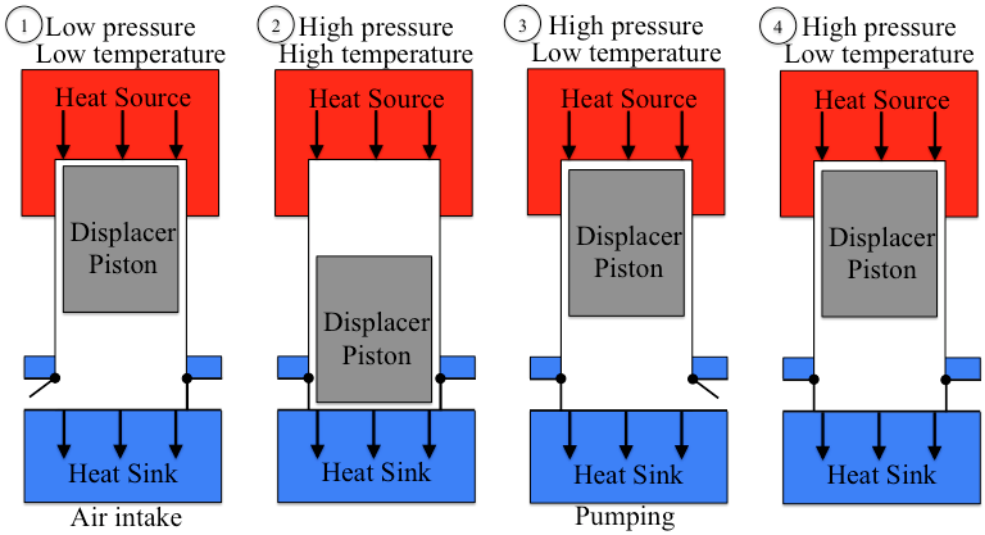

Figure 1.12 - Schematic illustrating the operation of single-stage Stirling thermocompressor

For the proposed thermocompressor, a brushless DC motor is used to drive a continuous linear reciprocating screw, onto which the displacer piston is affixed. The reciprocating screw is similar to a lead screw but differs in that the screw has a left-handed and right-handed thread to enable reciprocating motion of the nut with unidirectional screw rotation. This enables the reciprocating screw to be driven at constant velocity, while the piston position-time graph resembles a triangle wave profile. This is beneficial

since the use of the reciprocating screw reduces motor power consumption (a conventional lead screw would require accelerating and decelerating the motor shaft every cycle) and is easy to control. This arrangement is shown in Figure 1.13.

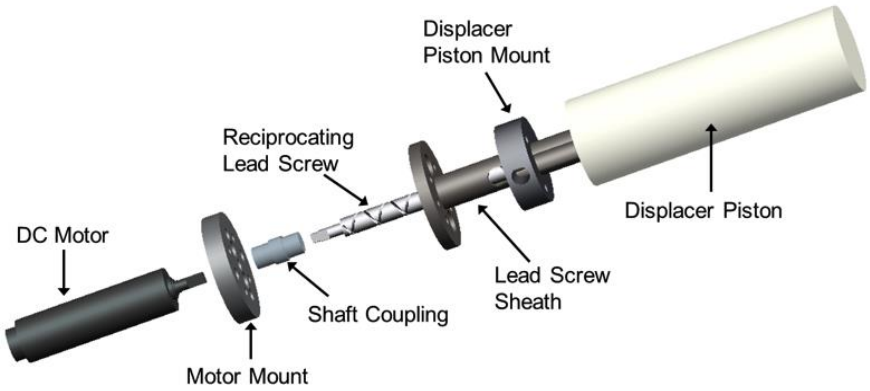

Figure 1.13 - CAD drawing of piston-motor assembly

The heat source for the final thermocompressor device will be hydrocarbon fuel. For this prototype, miniature high-temperature cartridge heaters were utilized for easy implementation. There was no pumping of working fluid into or out of the thermocompressor so that heat transfer and pressure dynamics could be isolated. A photograph of the assembled thermocompressor without heat exchangers and electric heaters is shown in Figure 1.14.

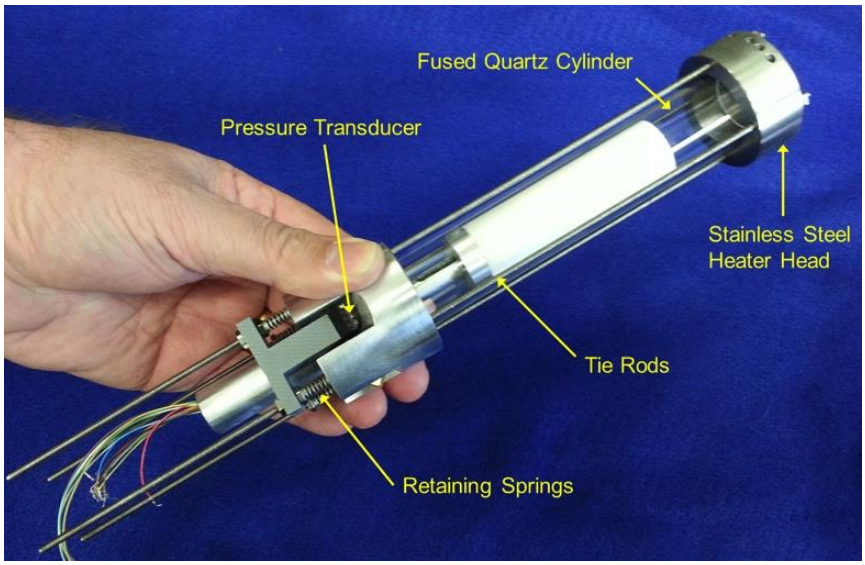

Figure 1.14 – Prototype Stirling thermocompressor without heat exchangers or electric heaters

The primary energetic bottlenecks addressed in this project are the interrelated issues of low operating frequency and limited rate of heat transfer to the working fluid. This was addressed through the inclusion of in-cylinder heat exchangers which make high operational frequencies possible while still

maintaining a high pressure ratio without significant additions to dead volume. When the heat exchangers are stretched at bottom dead center, there is increased surface area for air to gain thermal energy and increase its temperature and conversely, at top dead center, the stretched heat exchangers below the displacer piston effectively increase the contact area between the hot, high-pressure air and the room temperature metal discs, which causes the working fluid to rapidly decrease its temperature. The operation of these heat exchangers is illustrated below in Figure 1.15.

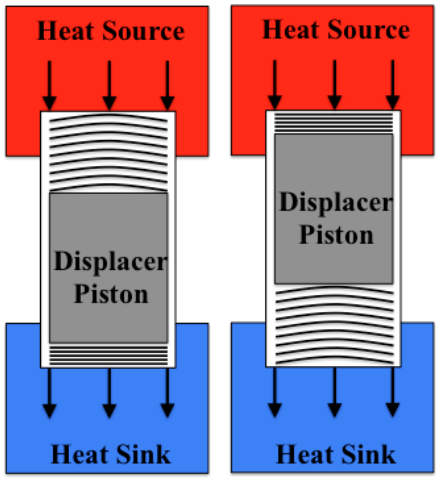

Figure 1.15 - Schematic of heat exchanger operation at bottom dead center (left) and top dead center (right)

The hot side heat exchangers are simply circular discs, but the cold side heat exchangers have a hole to accommodate the reciprocating screw housing piece (Figure 1.16).

Figure 1.16 - Collapsible, in-piston heat exchangers used in hot side (left) and cold side (right)

Two models were developed and validated using the experimental setup shown in Figures 1.14. One model is dynamic and takes mass flow restrictions and heat transfer limitations into account. The other model is quasi-static, derived from the ideal gas law, and assumes that mass flow is unrestricted and that the control volumes inside the thermocompressor are isothermal. Figure 1.17 shows measured data from the thermocompressor compared to both of these models.

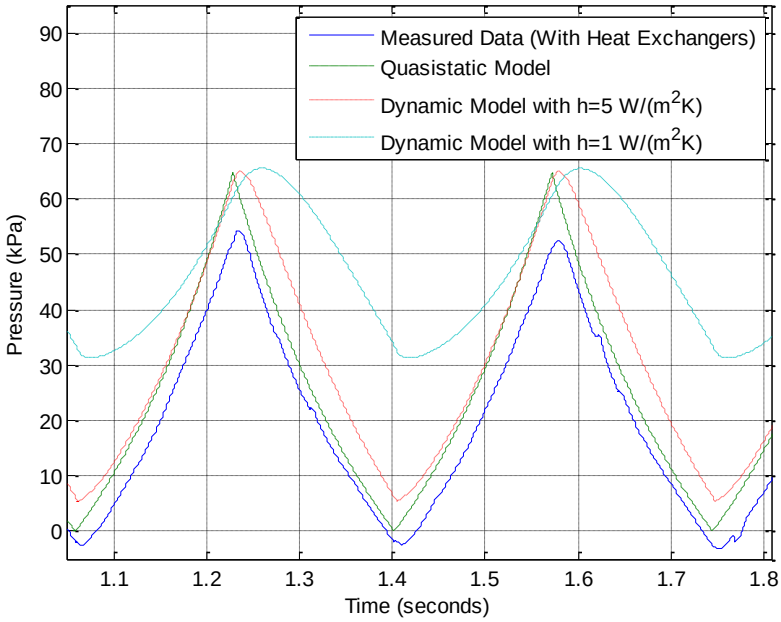

Figure 1.17 - Cold chamber pressure from experimental data and different models for 2.8 Hz operation and 600°C heater head temperature

To test the effectiveness of the heat exchangers and the accuracy of the model, the thermocompressor was operated both with and without the heat exchangers. Heat transfer was significantly enhanced by the addition of the heat exchangers. It was demonstrated that higher rates of heat transfer are capable of producing larger pressure swings in the working fluid which in turn lead to higher operational frequencies and power densities.

Document Organization

The dissertation is comprised of seven chapters. Chapter 2 describes the application of the maximum power transfer theorem to a bridge vibration energy harvester and provides experimental validation. Chapter 3 expands upon the idea by considering electrical components and therefore incorporates multiple energetic domains. Chapters 4 and 5 describe the construction of a free piston engine compressor and present experimental results. Chapter 6 presents a Stirling thermocompressor with experimentally validated quasi-static and dynamic models. Chapter 7 summarizes the dissertation and lists key contributions. Summaries of the manuscripts included in this dissertation are as follows:

Manuscript 1 (Chapter 2): From: *Experimental Research Platform for Structural Health Monitoring*, Babjak, B., Szilvasi, S., Pedchenko, A., Hofacker, M., Barth, E. J., Volgyesi, P., & Ledeczi

Abstract: A controlled vibration energy harvester is designed to power a node of a bridge condition monitoring sensor network. A control law for the harvester is derived using the maximum power transfer theorem. The derived controller possesses the novel feature of canceling the complex part of harvester's

impedance by eliminating inertial and stiffness elements. This enables the collection of the maximum amount of available power across a broad spectrum of frequencies. The controller does not contain the delay or the computational overhead of a fast Fourier transform because the excitation frequency is never explicitly calculated. This control approach is validated in simulation and experimentally using a prototype bridge energy harvester.

Manuscript 2 (Chapter 3): *Multi-Domain Impedance Matching Applied to a Bridge Vibration Energy Harvester*, Hofacker, M, Pedchenko, A, Barth, E. J.

Abstract: A controlled vibration energy harvester is designed to power a node of a bridge condition monitoring sensor network. Typically such vibration energy harvesting is done by matching a passive electrical network using impedance matching. This results in excellent power harvesting at the natural frequencies of the system, but power harvested from other frequencies present is negligible. The approach presented here formulates an active load impedance to broaden the spectrum of frequencies harvested. A multi-domain impedance matching technique is derived from the maximum power transfer theorem. This approach results in a canonically maximum power harvesting load but results in an unstable closed-loop system and cannot be implemented. Constrained optimization is used to find a controller that results in a stable closed-loop system while approximating the broad spectrum properties of the canonical load impedance. The controller has advantages over other approaches because the component excitation frequencies are not found explicitly using the Fourier transform, thereby allowing fast real-time implementation. Additionally, the proposed approach allows for the harvesting of energy from multiple frequency components simultaneously that is typically not seen in the literature. This control approach is validated in simulation and a prototype bridge energy harvester is presented as a platform for experimental validation. The results of this validation will be presented in the second portion this two-part paper.

Manuscript 3 (Chapter 4): *Design and Validation of a Figure-Eight Free-Liquid-Piston Engine Compressor for Compact Robot Power*, Barth, E. J., Hofacker, M, Kumar, N,

Abstract: This paper presents a brief overview of the free piston engine compressor for a compact rescue crawler robot. The evolution of the device from utilizing straight piston with a separated combustion chamber to a figure-eight piston with an integrated combustion chamber is described and explained. The necessity of a high-inertance piston is demonstrated via an analogy to a buck converter.

Manuscript 4 (Chapter 5): *An Experimentally Validated Figure-Eight Free-Liquid-Piston Engine Compressor*, Hofacker, M, Kumar, N, Barth, E. J.

Abstract: This paper presents the design and control of a free-piston engine compressor. Internal combustion with a propane-air mixture in the engine combustion chamber is used to displace a liquid piston and efficiently compress air. This results in low temperature, high-pressure air for use as a high

energy density power supply for untethered, compact robots. Traditional intake and compression strokes of a four-stroke engine are avoided by injecting compressed air and propane and by exploiting the dynamic loading of a high inertance, low mass liquid piston. Self-balancing of the single cylinder is achieved through the use of a liquid piston in a figure-8 configuration. The benefits of this configuration are demonstrated using simulated data and the Reynolds transport theorem. A closed loop controller is utilized to make intelligent decisions regarding the timing of air and fuel injection, the spark plug and the exhaust valve. The pumping pressure of the device is increased through improvement to the nozzles and to the pump chamber's outlet check valve. Experimental results are presented that demonstrate an increased pumping pressure over previous versions of this device.

Manuscript 5 (Chapter 6): *Dynamic Simulation and Experimental Validation of a Single Stage Thermocompressor for a Pneumatic Ankle-Foot,* Hofacker, M, Kumar, N, Barth, E. J.

Abstract: The mechanical design, modeling, and partial experimental validation of a prototype Stirling thermocompressor is presented in this paper. The thermocompressor is intended to serve as a compact and quiet, untethered 50 W, pneumatic power supply for an ankle foot orthosis. The goal of high efficiency at the target power density is pursued through the use of novel heat exchangers and high operating temperature and frequency. The motion of the displacer piston is controlled utilizing a brushless DC motor driving a continuous linear reciprocating screw. This paper presents the experimental validation of the heat transfer and pressure dynamics portions of the thermocompressor, leaving the modeling and validation of mass transfer to future work.

References

[1] Chen, Yeong-Chin, Sean Wu, and Ping-Cheng Chen. "The Impedance-matching Design and Simulation on High Power Elctro-acoustical Transducer." *Sensors and Actuators A: Physical* 115, no. 1 (September 15, 2004)

[2] Lim, Jee-Woo, and Bong-Hwan Kwon. "A Power-factor Controller for Single-phase PWM Rectifiers." *IEEE Transactions on Industrial Electronics* 46, no. 5 (October 1999): 1035 –1037. doi:10.1109/41.793353.

[3] De Paor, A., and B. Cogan. "Making a Connection: PI and PID Controller Tuning by Analogy with the Maximum Power Transfer Theorem of Circuit Theory." *Journal of Electrical Engineering* 55, no. 9–10 (2004): 277–80.

[4] Le Bunetel, J.C., and M. Machmoum. "Control of Boost Unity Power Factor Correction Systems." In *The 25th Annual Conference of the IEEE Industrial Electronics Society, 1999. IECON '99 Proceedings*, 1:266 –271 vol.1, 1999

[5] Kong, Na, Dong Sam Ha, Alper Erturk, and Daniel J. Inman. "Resistive Impedance Matching Circuit for Piezoelectric Energy Harvesting." *Journal of Intelligent Material Systems and Structures* 21, no. 13 (September 1, 2010): 1293–1302.

[6] Calleja, H., and R. Ordofiez. “Control Circuit for an Induction Heating Inverter with Active PFC.” In *29th Annual IEEE Power Electronics Specialists Conference, 1998. PESC 98 Record*, 1:485 –490 vol.1, 1998.

[7] Murray, Aengus. “Digital Controller Makes Power Factor Correction Feasible in AC Adapters.” *Power Electronics Technology* 31, no. 5 (2005): 10.

[8] Akbaba, Mehmet. “Optimum Matching Parameters of an MPPT Unit Used for a PVG-powered Water Pumping System for Maximum Power Transfer.” *International Journal of Energy Research* 30, no. 6 (2006): 395–409.

[9] Li, Weixing, Tongwen Chen, and Wilsun Xu. “On Impedance Matching and Maximum Power Transfer.” *Electric Power Systems Research* 80, no. 9 (September 2010): 1082–1088.

[10] Le Bunetel, J.C., and M. Machmoum. “Control of Boost Unity Power Factor Correction Systems.” In *The 25th Annual Conference of the IEEE Industrial Electronics Society, 1999. IECON ’99 Proceedings*, 1:266 –271 vol.1, 1999.

[11] Reza Brufau-Penella, J., and M. Puig-Vidal. “Piezoelectric Energy Harvesting Improvement with Complex Conjugate Impedance Matching.” *Journal of Intelligent Material Systems and Structures* 20, no. 5 (March 1, 2009): 597–608.

[12] Apertet, Y., et al. "Optimal working conditions for thermoelectric generators with realistic thermal coupling." *EPL (Europhysics Letters)* 97.2 (2012): 28001.

[13] Lossec, Marianne, Bernard Multon, and Hamid Ben Ahmed. "Sizing Optimization with Thermal and Electrical Matching of a Thermogenerator placed on the Human Body." *Proc. of International Conference on Renewable Energy and Eco-Design in Electrical Engineering*. 2011.

[14] Lawson, D. I., and J. H. McGuire. "The Solution of Transient Heat-flow Problems by Analogous Electrical Networks." *Proceedings of the Institution of Mechanical Engineers* 167.1 (1953): 275-290.

[15] Tijani, M. E. H., Srinivas Vanapalli, and Simon Spoelstra. "Design of a mechanical resonator to be coupled to a thermoacoustic stirling-engine." (2010).

[16] Cassan, David J., and John R. Long. "A 1-V transformer-feedback low-noise amplifier for 5-GHz wireless LAN in 0.18-μm CMOS." *Solid-State Circuits, IEEE Journal of* 38.3 (2003): 427-435.

[17] Branner, G.R.; Johnson, J.E., "Harmonic balance analysis of input impedance matching in active RF/microwave frequency multipliers," Circuits and Systems, 2004. MWSCAS '04. The 2004 47th Midwest Symposium on , vol.1, no., pp.I,201-4 vol.1, 25-28 July 2004

[18] Godara B., Fabre A., “The First Active Tuneable Wideband Impedance Matching Network”, in Electroscope Online Journal, University of West Bohemia, 2008.

[19] Brufau-Penella, J., and M. Puig-Vidal. “Piezoelectric Energy Harvesting Improvement with Complex Conjugate Impedance Matching.” *Journal of Intelligent Material Systems and Structures* 20, no. 5 (March 1, 2009): 597–608.

[20] Willhite, J. A. (2010). Dynamic Model-Based Design, Validation, and Characterization of a Compact, High-Inertance Free Liquid Piston Engine Compressor. Dissertation, Vanderbilt University.

Retrieved from Vanderbilt University Electronic Theses and Dissertations (etd -12102010-11502)

[21] Yong, C. (2011). *A Virtual-Cam Based Control Methodology for Free-Piston Engines*. Dissertation, Vanderbilt University. Retrieved from Vanderbilt University Electronic Theses and Dissertations (etd – 07282011-114037)

[22] Riofrio, J. A. (2008). *Design, Modeling and Experimental Characterization of a Free Liquid-Piston Engine Compressor with Separated Combustion Chamber*. Dissertation, Vanderbilt University. Retrieved from Vanderbilt University Electronic Theses and Dissertations (etd - 12102010-11502)

2. Experimental Research Platform for Structural Health Monitoring

Babjak, Benjamin, Sandor Szilvasi, Alex Pedchenko, Mark Hofacker, Eric J. Barth, Peter Volgyesi, and Akos Ledeczi

Vanderbilt University

Nashville, TN

Excerpt From: *Advancement in Sensing Technology*. Springer Berlin Heidelberg, 2013. 43-68

Status: Published 2013

Prologue

This paper describes a prototype controlled bridge vibration energy harvester and presents its experimental results. The impedance view of the harvester is shown in Figure 2.i. With regard to the overall impedance framework proposed by this dissertation, the work presented on the harvester considers both the source impedance and the load impedance. This resulted in mechanical design implications from considering the source impedance and control design implications from considering the load impedance.

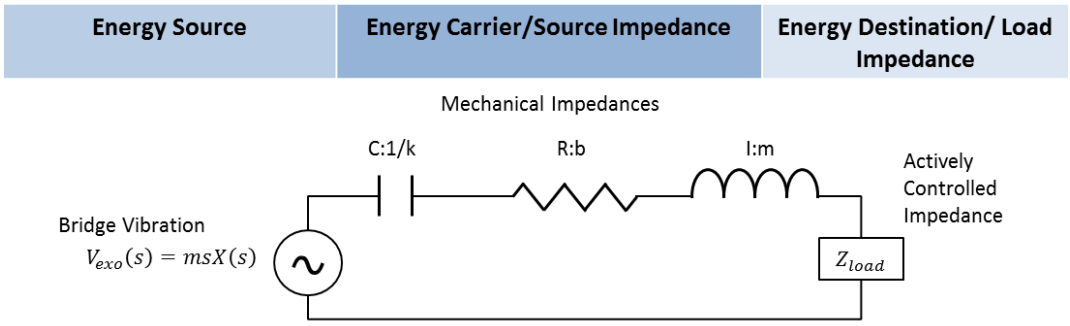

Figure 2.i - Electrical circuit approximation of the bridge vibration energy harvester

The bridge vibration energy harvester is the most straightforward application of the impedance matching framework because the system contains mostly linear components and an exogenous input. The bridge vibration is the energy source, it is considered exogenous because bridge excitation is independent of harvester motion since the bridge is very large relative to the size of the harvester. The proof mass and spring elements in this represent the harvester's energy carrier because they temporarily store energy before it is converted to electrical current through the linear motor/generator. Electrical

output is desired in this project, making the load impedance the energetic destination.

To simplify the problem, initial experiments and calculations were performed under the assumption of no electrical losses. Additionally, the physical mounting of the harvest was modified such that the harvester was connected to both to the bridge and the ground. This arrangement differs from a practical vibration energy harvester but it was utilized for ease of construction.

In this project, the primary energetic bottleneck was the frequency dependency of the uncontrolled mechanical components and mechanical frictional losses. These challenges were minimized through mechanical design by employing compliant mechanisms and through active control of the proof mass. A closed loop controller was found by determining the ideal closed loop behavior based on the maximum power transfer theorem. This controller enabled the bridge vibration energy harvester to capture energy from a broad band of bridge vibrational frequencies.

Most work regarding the active modification of impedance is related to the reception of an RF signal [1i]. The work in this document differs conceptually because the transmission of RF signals is concerned with noise minimization as opposed to strictly addressing power delivery.

Brafau applies a similar technique by attempting to passively cancel the complex impedances of a piezoelectric bridge vibration energy harvester [2i]. This is similar to the approach described in this dissertation, but differs because the cancelation is passive instead of active. Galchev, Peigney, and Kong utilized passive control and modified mechanical design parameters so that the ideal operating frequency of the harvester matches the most prominent vibrational frequencies of the intended bridge [3i-5i]. The unique aspect of this work is the application of active control to create a generic device that can harvest significant power from a broad frequency range.

Abstract

A controlled vibration energy harvester is designed to power a node of a bridge condition monitoring sensor network. A control law for the harvester is derived using the maximum power transfer theorem. The derived controller possesses the novel feature of canceling the complex part of harvester's impedance by eliminating inertial and stiffness elements. This enables the collection of the maximum amount of available power across a broad spectrum of frequencies. The controller does not contain the delay or the computational overhead of a fast Fourier transform because the excitation frequency is never explicitly calculated. This control approach is validated in simulation and experimentally using a prototype bridge energy harvester.

I. Introduction

In August of 2007, the I-35 W Mississippi River Bridge collapsed during rush hour, causing numerous fatalities and injuries. Structural deficiency in the region of failure was noted in the bridge inspection report in March 2001, but was not considered severe enough to warrant bridge replacement. However, the report was accompanied by research which recommended the use of strain gauges to monitor the

condition of this bridge, as well as other bridges similar to it, in order to detect signs of approaching failure. [1] This recommendation was not followed for this particular bridge, but the suggestion remains pertinent because the U.S. Department of Transportation has found that 25% of bridges are “functionally obsolete” or “structurally deficient” [2]. All bridges are currently only visually inspected biennially [3]. To avoid the catastrophic consequences of bridge failure, more frequent bridge monitoring is necessary. Fortunately, technology which allows monitoring and evaluation of bridge health is currently available. Measurement from strain gauges placed at key points on the bridge [4] as well as pattern recognition of bridge acceleration data [5] are two techniques currently used for assessing the structural condition of bridges. Other prediction methods of material failure include the monitoring of acoustic emissions [6].

Whichever method is chosen to monitor the health of a bridge, sensing and transmitting the bridge’s condition requires electrical power. Wiring the bridge health monitoring device(s) to power and data networks would be difficult and expensive [7], so ideally data would be transmitted wirelessly and power would be generated locally. Power generation is preferable to using batteries, as the latter would require regular replacement. Solar and wind power should be avoided, as both are not guaranteed to generate power when it is most needed, i.e., during heavy traffic conditions; additionally, mounting options would be limited depending on bridge configuration.

In this paper, an electromechanical generator that harvests power from bridge vibrations will be investigated. This kind of device does not require external wiring, and has little need for maintenance during long periods of operation. The three most commonly used techniques for electromechanical generation are electrostatic, piezoelectric, and electromagnetic [8, 9, 10]. Out of these three options, an electromagnetic generator was chosen for this application due to its robustness and controllability properties (for an in depth explanation of the advantages of electromagnetic generation in bridge vibration energy harvesting please refer to [11]).

Electromagnetic generators operate in a similar manner to a mass-spring-damper system, where power is extracted from the damping element. The drawback of these devices is that they are only able to collect an appreciable amount of power when the bridge oscillates at or close to the generator’s natural frequency [8]. This poses a significant problem because different bridges oscillate at different frequencies [3], a particular bridge will oscillate differently depending on traffic [5], and the oscillation of any given point on a bridge usually contains multiple frequencies [12].

This paper describes a method of overcoming these challenges by actively controlling the motion of the harvester to maximize the amount of power harvested. A controller is derived utilizing the maximum power transfer theorem. This approach allows power to be harvested from the entire spectrum of frequencies present. This control methodology is validated using a low-friction prototype electromechanical harvester and the results are presented.

II. Derivation of Control Law

The motivation behind the controller is to extract the maximum amount of power from all frequency

components of bridge oscillation utilizing a harvester of the form shown in Fig. 2.1-i. This concept has been fully explored in the electrical domain with the maximum power transfer theorem, which dictates the necessary load to transfer the most power from a specific source to the said load. To apply this theorem to the vibrational energy harvester, the mechanical system is converted to its dynamic equivalent in the electrical domain as shown in Fig. 2.1. The bond graph shown in Fig. 2.1-ii is an intermediate step used to preserve the system's dynamics during conversion into the electrical domain. The equivalent electrical circuit (Fig. 2.1-iii) is then converted to its Thevenin form (Fig. 2.1-iv) so that the maximum power transfer theorem can be easily applied.

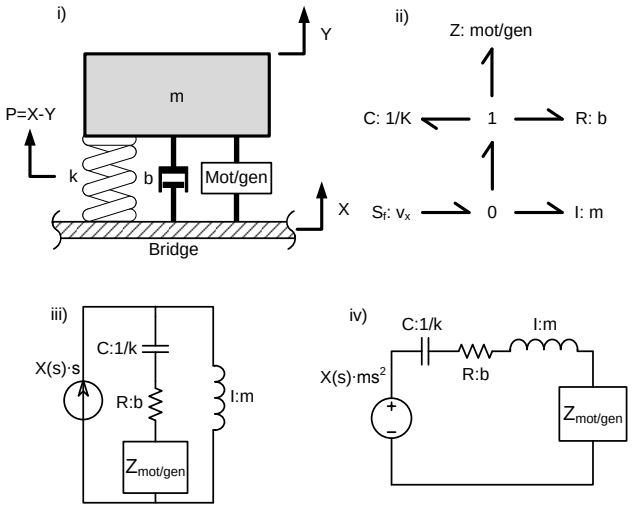

Figure 2.1 - Transformation of bridge energy harvester into electrical domain: i) mechanical representation; ii) bond graph representation; iii) electrical equivalent of bond graph; iv) Thevenin equivalent circuit

In the mechanical domain, the vibrational bridge energy harvester can be represented by a conventional mass-spring-damper (where the damper represents an un-avoidable parasitic dissipation associated with the mechanism) with an additional element in parallel with the spring and the damper components (see Fig. 2.1-i). In passive electromagnetic harvesters, this component is a generator that harvests power by siphoning kinetic energy from the mass, *m*. In an actively controlled harvester, this component functions as both a generator and a motor. In casting the system from Fig. 2.1-i into bond graph form, as shown in Fig.2.1-ii, the motor/generator is represented by a generalized impedance, $Z_{mot/gen}$. In the circuits shown in Fig. 2.1-iii and Fig. 2.1-iv, the current flowing through a component is equivalent to the velocity of the component (flow variable) and the voltage across a component is equivalent to the force exerted by said component (effort variable). Although all of the representations of the system have identical dynamic behaviors, the Thevenin equivalent circuit allows direct application of the maximum power transfer theorem. Additionally it allows the relationship between current and voltage of the harvester to be clearly seen as described below in (1),

$$\frac{P(s)s}{ms^2X(s)} = \frac{1}{\left(\frac{k}{s}+b+ms+\mathrm{Z_{mot/gen}}\right)} \quad (1)$$

where $ms^2X(s)$ is the equivalent voltage source, $P(s)s$ is the current running through the circuit components, $\frac{k}{s}$, b, and ms are the impedances of the equivalent capacitor, resistor and inductor respectively.

In applying the maximum power transfer theorem to the electrical system depicted in Fig. 2.1-iv, we note that parameters *k*, *m*, and *b* cannot be changed as they represent the physical characteristics of the energy harvester. Since in the Thevenin equivalent circuit, the component is analogous to the load, the combined impedance of mass, spring, and damper can be defined as the source impedance. The frequency-dependent behavior of this complex impedance, $\mathrm{Z_{SRC}}$, can be described by:

$$\mathrm{Z_{SRC}} = \frac{k}{s} + b + ms\Big|_{s=j\omega} = b + j\left(m\omega + \frac{k}{\omega}\right) \quad (2)$$

Knowledge of the source impedance, $\mathrm{Z_{SRC}}$, in (2) and the dynamic response of the system (1) allows the designer to formulate a controller capable of satisfying the maximum power transfer theorem. The theorem states that maximum power transfer to the load occurs when the load impedance is the complex conjugate of the source impedance as shown in (3)

$$\mathrm{Z_{LOAD}} = \mathrm{Z_{SRC}^*} \leftrightarrow \mathrm{Z}_{mot/gen} = \mathrm{Z_{SRC}^*} \quad (3)$$

When this condition is satisfied, the sum of the load and source impedance contains double the resistance/damping of the source and no complex component. Successful load matching defined

By (3) when applied to (1) reduces it to

$$\frac{P(s)s}{ms^2X(s)} = \frac{1}{(Z_{SRC}+\mathrm{Z_{mot/gen}})} = \frac{1}{2b} \quad (4)$$

The electrical and mechanical equivalents of the above transfer function are shown below in Fig. 2.2:

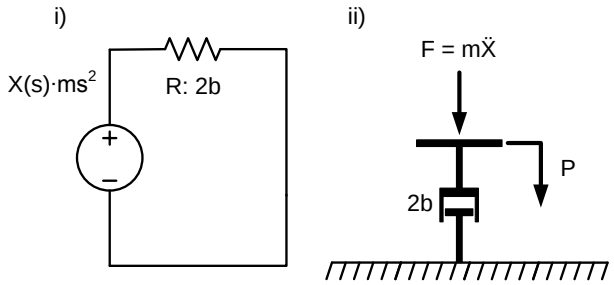

Figure 2.2 - Electrical circuit (i) and mechanical system (ii) representations of ideal energy harvester behavior

This ideal behavior is logical because both systems are composed of only a resistive element, which is the sole component capable of power generation. Physically, inertial components (masses) and capacitive elements (springs) are necessary only because they store and direct the kinetic energy from which power is extracted. This behavior can also be shown to be ideal by noting that it is equivalent to a mass-spring-damper system when its input frequency is equal to the system's natural frequency. Explicitly,

$$\frac{P(s)s}{ms^2X(s)} = \frac{1}{\left(\frac{k}{j\omega}+2b+mj\omega\right)}\Bigg|_{\omega=\omega_n=\sqrt{\frac{k}{m}}} = \frac{1}{2b} \tag{5}$$

This can also be seen in (2), when the forcing frequency (ω) is equal to the system's natural frequency (ω_n), only the real component remains.

To achieve the modeled behavior shown in (4), control must be applied to the motor/generator. The equation of motion derived from Fig. 2.1-i with the motor/generator applying a force u(t) is:

$$m\ddot{y} = b(\dot{y} - \dot{x}) + k(y - x) + u(t) \tag{6}$$

Reorganizing the equation, letting $= (x - y)$, and performing a Laplace transformation, yields:

$$P(s)(ms^2 + bs + k) = X(s)s^2 + U(s) \tag{7}$$

In order to obtain the desired transfer function shown in (4), $U(s)$ must be set equal to the following:

$$U(s) = P(s)(ms^2 - bs + k) \tag{8}$$

which is the controller which satisfies the maximum power transfer theorem as it applies to the vibration energy harvester. Although this controller is acausal it can be implemented practically because relative

acceleration, velocity, position can all be directly measured. In implementation, it also requires regenerative electronics in order to mimic the correct energy storage, return, and extraction behavior required for the impedance match.

III. Simulation Results

Let us compare the frequency behavior of (9) to that of the transfer function of the same system operating passively. The system shown in Fig. 2.1-ii behaves according to the transfer function shown below

$$\frac{\mathrm{P(s)}}{\mathrm{ms^2X(s)}} = \frac{\mathrm{P(s)}}{\mathrm{F(s)}} = \frac{1}{2\mathrm{bs}} \tag{9}$$

where F(s) is used to replace , which is the force imposed on the mass by the vibration of the bridge. If the system shown in Fig. 2.1-i was operating as a passive vibration energy harvester, $\mathrm{Z_{mot/gen}}$would be tuned such that it doubles the parasitic damping (i.e., acts like another damper *b* [3]). This type of system would have the transfer function:

$$\frac{P(s)}{F(s)} = \frac{1}{ms^2+bs+k+Z_{mot/gen}} = \frac{1}{ms^2+2bs+k} \tag{10}$$

where inputs and outputs are the same as those for (9). Figure 2.3 shows the behaviors defined by (10) for several passive energy harvesters with different natural frequencies (f_n = 4Hz, 6Hz, 8Hz, 10Hz), as well as the behavior of the controlled system defined by (9).

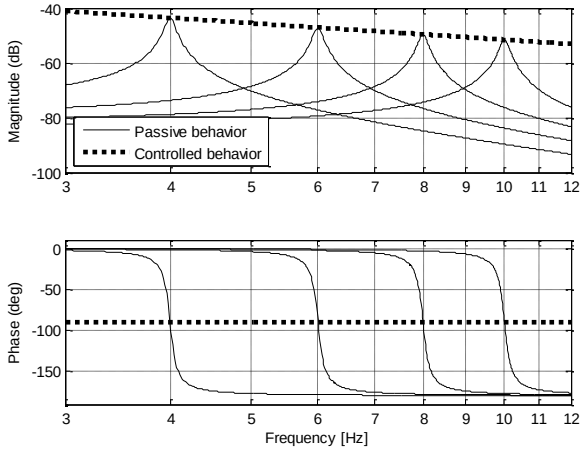

Figure 2.3 - Position response of several passive, tuned, energy harvesters and the controlled impedance matched energy harvester to a force input

The power generated by a passive, tuned, vibrational energy harvester was described by [8] as follows:

$$P_d = \frac{m\delta Y^2\left(\frac{\omega}{\omega_n}\right)^3 \omega^3}{\left(1-\left(\frac{\omega}{\omega_n}\right)^2\right)^2+\left(2\delta\left(\frac{\omega}{\omega_n}\right)\right)^2} \quad (11)$$

where represents the magnitude of the proof mass, is the bridge vibration frequency, and is the natural frequency of the harvester. Figure 2.4 below shows the net power that the harvester demonstrated in Fig. 2.1-i would generate, given that the bridge vibrates sinusoidally at an amplitude of 0.25 mm and each harvester has a mass of 0.55 kg and a damping ratio of 0.013.

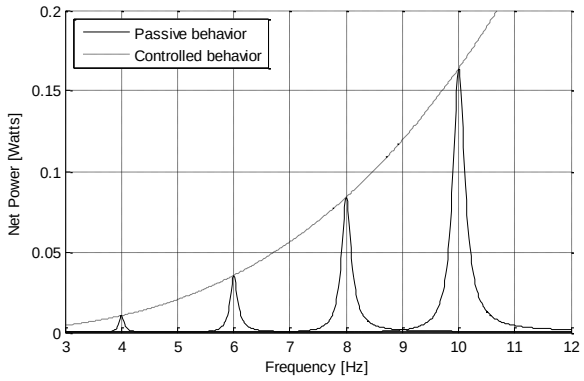

Figure 2.4 - The power generated by passive and controlled harvesters vs. frequency

As seen in Fig 2.4, the controlled device is capable of extracting as much power as a properly tuned passive device when the bridge operates at the passive device's natural frequency, yet the controlled device has much higher bandwidth than any single passive system. Another advantage of having no single natural frequency is that the controller is able to respond intelligently to bridge oscillations that contain more than one frequency component. Bridge vibration data from Shahabadi [12] containing 6Hz, 7Hz, and 12Hz components was reproduced in simulation and used to excite a passive harvester, and an identical harvester with active control. Again, the simulation harvesters had a mass of 0.55 kg and a damping ratio of 0.013. The spring stiffness was chosen to be 975 N/m for a natural frequency of 6.7 Hz. The bridge's position and corresponding responses of the two harvesters is shown below in Fig. 2.5.

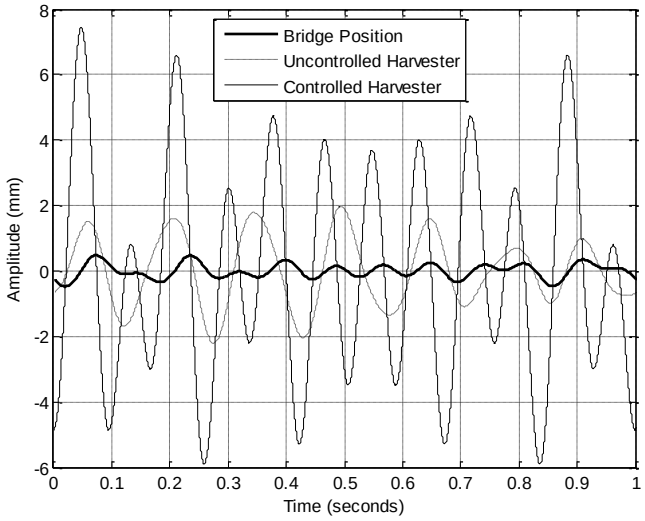

Figure 2.5 - Passive and controlled responses of the energy harvester to a force input

From Figure 2.5 it can be seen that amplitude of oscillation of the controlled harvester is far greater than that of the uncontrolled. For increased clarity, the amplitude of the bridge is shown as opposed to the force exerted on the harvester as used in Fig.2.3. From the figure, we see that the bridge has 90° phase lag on the harvester. Since we know that input force has 180° phase lead on the bridge position, we can infer that the harvester position has 90° phase lag on the input force, as previously demonstrated in Fig. 2.3. This is to say that the controlled harvester behavior shown in Fig. 2.5 exhibits the harvester's ability to maintain 90° phase lag on the incoming force even when excited by more than a single frequency.

The ability to increase amplitude and maintain phase lag increases the power output of the device. Calculations from the simulation show that if the motor and generator were both 100% efficient, the controlled device would generate a net 13.3 mW, while the uncontrolled device would harvest 4.37 mW when both are exposed to the bridge vibrations shown in Fig. 2.5. Even with a more realistic estimate of 70% efficiency of regeneration and actuation, the controlled device would still yield 9 mW of net power.

IV. Experimental setup and results

A small scale harvester was constructed so that a controller based on the maximum power transfer theorem could be tested on a physical device. In this prototype, a linear motor was used as both the proof mass and the motor/generator. Compliant mechanisms were arranged into self-aligning spring elements to eliminate the need of bearing surfaces. It is vital to decrease parasitic losses because the total amount of power available from bridge vibrations is in the sub-watt range. To create this self-aligning spring structure, 16 guided-beam compliant mechanisms were arranged in such a way as to be extremely stiff in translational and rotational modes yet have an appropriate amount of compliance along the axis of the linear motor. The compliant structure had a stiffness of 975 N/m, and an effective mass of 0.55 kg,

yielding a natural frequency of 6.7 Hz. Using frequency response data from the prototype, its damping ratio was measured to be 0.013. The simulated data for Fig. 2.5 used these same parameters such that experimental and simulated results can be compared directly.

A second, larger linear motor was used to simulate actual bridge motion. Acceleration and position of the proof mass and base excitation ("bridge motion") were collected using accelerometers, a potentiometer, and an encoder.

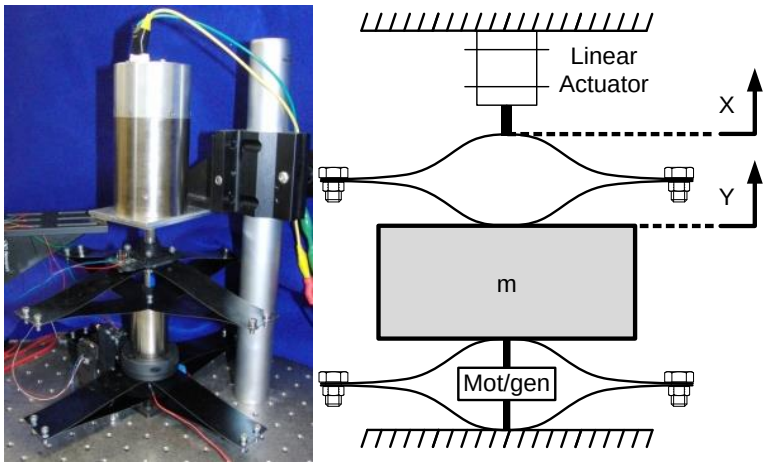

Figure 2.6 - Experimental setup photograph and schematic

There is a notable difference between the experimental device, shown in Fig.2.6, and a device that could be used on a bridge for energy harvesting. The device shown in Fig. 2.6 is connected to an unmoving ground through a spring element, which would not be practical with a real bridge. For the device in Fig. 2.6 to be used on a bridge, a stiff, strong structure needs to be built to connect the top spring to the bottom spring. Mounting such a structure on a bridge would not pose a problem, but in the current setup, the linear motor used to provide bridge motion was not powerful enough to move such a structure precisely.

By converting the experimental setup shown in Fig. 2.6 (represented schematically in Fig. 2.7-i) to its Thevenin equivalent shown in Fig. 2.7-iv, it is seen that the dynamic elements of the experimental apparatus are identical to the elements of the ideal device shown in Fig.2.1. The only difference lies in the way the power from the bridge is transmitted to the harvester.

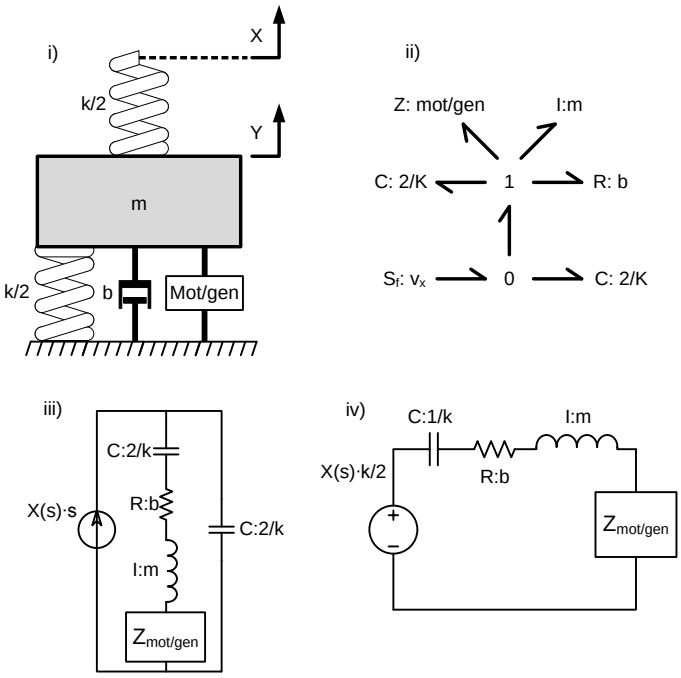

Figure 2.7 - Transformation of prototype harvester into electrical domain: i) mechanical representation; ii) bond graph representation; iii) electrical equivalent of bond graph; iv) Thevenin equivalent circuit

The transfer function of the system depicted in Fig. 2.7, shown below in (7), has the same characteristic equation as that of the original system shown in (10) In other words, the transfer functions only differ in their forcing functions

$$\frac{Y(s)}{X(s)} = \frac{\frac{k}{2}}{ms^2+bs+k+\mathrm{Z}_{\mathrm{mot/gen}}} \tag{12}$$

.

Controlling this apparatus to satisfy the requirements of maximum power transfer theorem is therefore quite similar to controlling the device shown in Fig. 2.1-i. It is only necessary to double the system's damping and eliminate the inertial and stiffness elements, which results in (12) reducing to the following ideal transfer function:

$$\frac{Y(s)}{X(s)} = \frac{\frac{k}{2}}{2bs} \tag{13}$$

This desired behavior is marginally stable, which is problematic because when practically implemented it causes the proof mass to drift. To eliminate this problem, the desired behavior needs to contain a filter that attenuates the lower frequencies. Combining such a filter with (13) yields the transfer function shown in (14), which exhibits stable desired behavior of the harvester.

$$\frac{Y(s)}{X(s)} = \frac{\frac{k}{2}}{2bs} \frac{\tau^2 s^2}{(\tau s+1)^2} \quad (14)$$

In the above equation, τ is the time constant that determines which frequencies are attenuated. For the data shown in this paper τ = 0.57 was used which gives a knee of 3.57 Hz. The desired transfer function shown in (14) can be achieved by implementing the following control law through the linear motor.

$$u = \ddot{y}(m - 2b\tau^2) + \dot{y}(b - 4b\tau) + (k - 2b) + \dot{x}\frac{k}{2}\tau^2 - x\frac{k}{2} \quad (15)$$

In the experimental data shown in Fig. 2.8 and Fig. 2.9, the artificial bridge was excited at several different frequencies. The control law shown in (15) was applied to the harvester and its experimental response was recorded and compared to the modeled responses of Damping Only Control (12), Unfiltered implementation of the maximum power transfer theorem (MPTT) controller (13), and Implementation of the MPTT controller with filter (14).

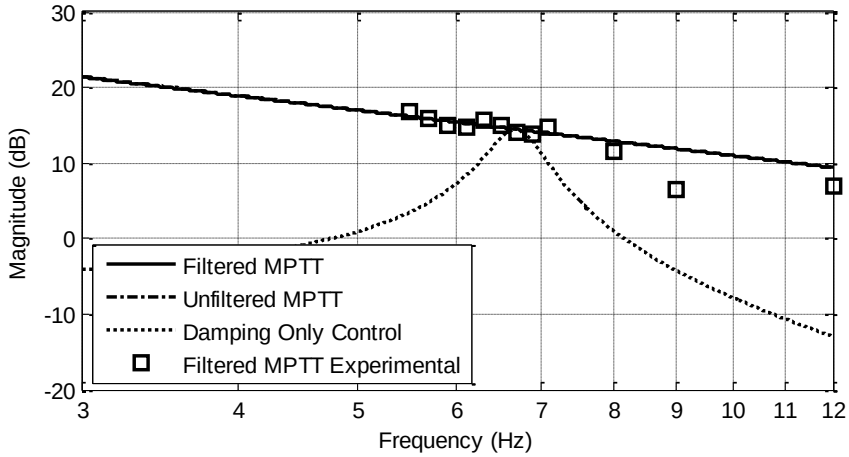

Figure 2.8 - Experimental magnitude response of controlled harvester mass to vibrations compared to the response of passive harvester and the ideal response of a controlled harvester.

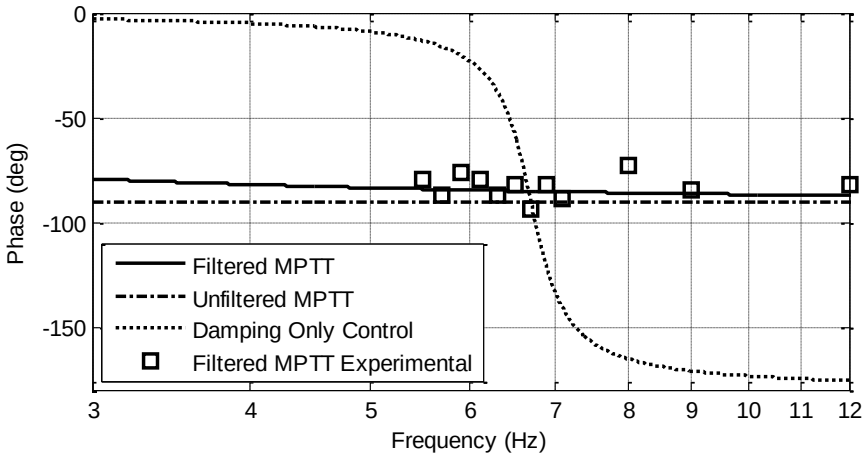

Figure 2.9 - Experimental phase response of controlled harvester mass to vibrations compared to the response of passive harvester and the ideal response of a controlled harvester.

These figures show that the filter applied to the ideal behavior does not have a significant effect at the frequencies of interest. Also shown is that the actively controlled harvester closely follows the desired behavior in both magnitude and phase, which implies that it is capable of collecting power across a broad spectrum of frequencies. The controller also demonstrates its ability to simultaneously harvest power from multiple frequencies. This is an important characteristic for a practical harvester because bridges usually move in multiple modes, which means there is potential for harvesting much more power than can be contained in a single frequency component. To demonstrate this ability, the artificial bridge was excited with 6Hz, 7Hz, and 12Hz components simultaneously. The position of the harvester was recorded while the harvester was actively controlled. The bridge was excited with the same frequencies without the controller. The results of these tests are shown in Fig. 2.10:

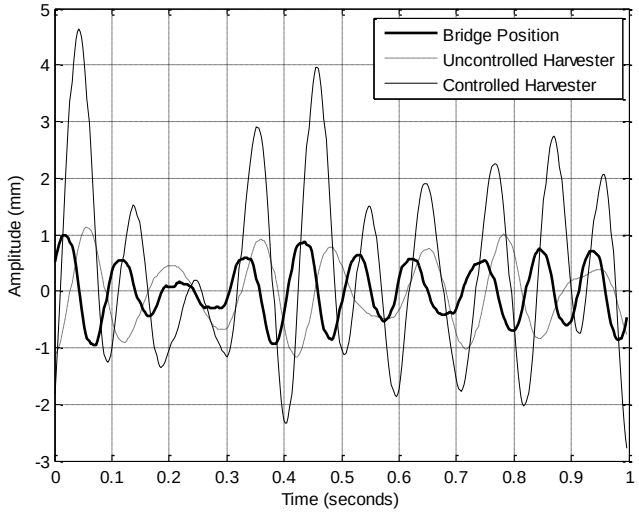

Figure 2.10 - Experimental response of harvester mass to vibrations with and without active control.

Two of the harvester's important characteristics are demonstrated in Fig.2.10. First, even though the uncontrolled harvester has only half of the damping of the actively controlled harvester, the controlled harvester has much higher amplitudes of oscillation. Secondly, the controller causes the harvester to have approximately 90° phase lag, which is evidence that the controller is performing as predicted in simulation, shown in Fig. 2.5.

V. Conclusion

Practical bridge health monitoring requires a self-contained power source to power sensors and transmit bridge health data wirelessly. It is possible to harvest power from bridge vibrations by connecting a mass to a bridge via a spring and converting some of the mass's kinetic energy into useful electrical power with a generator.

In this paper it was shown that by applying the principles of the maximum power transfer theorem to the control of the power extraction element, more power can be extracted from given bridge vibrations than is possible passively. By considering the Thevenin electrical equivalent of the harvester it becomes clear that in order to satisfy the maximum power transfer theorem, the controller must satisfy two criteria: (1) Complex impedance elements (the mass and spring components) of the source must be cancelled by the load, and (2) the real component of the impedance (the systems internal damping) must be matched by the load's damping for energy harvesting.

By accomplishing these goals, the harvester is able to maximize the magnitude of its motion and, as required by the maximum power transfer theorem, keep it 90° out of phase with the source motion across a wide range of vibration frequencies. There is no single natural frequency of the controlled harvester, which allows for appreciable power to be extracted from multiple frequency components simultaneously. With the control methodology presented in this paper, the dominant frequency of the bridge does not need to be computed, so there is no delay or computational overhead inherent to fast Fourier transforms. Furthermore, because the controller is composed of entirely linear computations, it could be implemented with low computational overhead and power requirements, or with analog circuitry. Taken together, the characteristics of this controller could increase the power output of a bridge vibration energy harvester and make locally powered bridge health monitoring systems more viable.

References

[1i] Balwant Godara, Alain Fabre, The First Active Tuneable Wideband Impedance Matching Network, in Electroscope Online Journal, University of West Bohemia, 2008.

[2i] Brufau-Penella, J., and M. Puig-Vidal. "Piezoelectric Energy Harvesting Improvement with Complex Conjugate Impedance Matching." *Journal of Intelligent Material Systems and Structures* 20, no. 5 (March 1, 2009): 597–608.

[3i] T. Galchev, J. McCullagh, R. L. Peterson, K. Najafi, "Harvesting Traffic-Induced Bridge Vibrations," Conf. Rec. 2011 IEEE Transducers' 11, pp 5-9, June 2011.

[4i] Kong, Na, Dong Sam Ha, Alper Erturk, and Daniel J. Inman. “Resistive Impedance Matching Circuit for Piezoelectric Energy Harvesting.” *Journal of Intelligent Material Systems and Structures* 21, no. 13 (September 1, 2010): 1293–1302.

[5i] Peigney, Michaël, and Dominique Siegert. "Piezoelectric energy harvesting from traffic-induced bridge vibrations." Smart Materials and Structures 22.9 (2013): 095019.

[1] O'Connell, Heather M.; Dexter, Robert J.; Bergson, Paul.; , "Fatigue Evaluation of the Deck Truss of Bridge 9340 - CTS Research Reports." Center for Transportation Studies. University of Minnesota, 2007. Web.

[2] U.S. Dept. of Transportation. “Our Nation’s Highways: 2010,” Web. <http://www.fhwa.dot.gov/policyinformation/pubs/hf/pl10023/fig7_3.cfm>.

[3] T. Galchev, J. McCullagh, R. L. Peterson, K. Najafi, “Harvesting Traffic-Induced Bridge Vibrations,” Conf. Rec. 2011 IEEE Transducers’ 11, pp 5-9, June 2011.

[4] Sazonov, E., Haodong Li, Curry, D.; Pillay, P. "Self-Powered Sensors for Monitoring of Highway Bridges,"Sensors Journal, IEEE, vol.9, no.11, pp.1422-1429, Nov. 2009

[5] Williams, C. B., A. Pavic, R. S. Crouch, and R. C. Woods. "Feasibility study of vibration-electric generator for bridge vibration sensors," Vibration Engineering Research Section, University of Sheffield. Society for Experimental Mechanics. Web. <http://vibration.shef.ac.uk/pdfs/IMAC_XVI_3.pdf>.

[6] R. K. Miller, “Acoustic Emission Testing”, Nondestructive testing handbook, 3rd edition, vol. 6, American Society for Non-destructive Testing, Columbus, OH, 2006

[7] J.P. Lynch, et al., “Design and performance validation of a wireless sensing unit for structural monitoring applications,” *Structural Engineering and Mechanics,* vol 17, no. 3-4, 2004, pp. 393-408.

[8] Beeby, S. P., M. J. Tudor, and N. M. White. "Energy Harvesting Vibration Sources for Microsystems Applications." Meas. Sci. Technol.17 (2006): 175-95. IOPscience. Web.

[9] Chalasani, S.; Conrad, J.M.; "A survey of energy harvesting sources for embedded systems, "Southeastcon, 2008. IEEE, vol., no., pp.442-447, 3-6 April 2008

[10] Moghe, R.; Yi Yang; Lambert, F.; Divan, D.; "A scoping study of electric and magnetic field energy harvesting for wireless sensor networks in power system applications," Energy Conversion Congress and Exposition, 2009. ECCE 2009. IEEE, vol., no., pp.3550-3557, 20-24 Sept. 2009

[11] Pedchenko A.V., Hoke J. W., and Barth E. J. “A Control Approach for Broadening the Operating Frequency Range of a Bridge Vibration Energy Harvester,” Paper accepted for the 2011 ASME Dynamic Systems and Control Conference, in press. Nov. 2011

[12] A. Shahabadi, (1977). Bridge Vibration Studies: Interim Report. Purdue e-Pubs [Online] pp. 108-130 Available: http://docs.lib.purdue.edu/cgi/viewcontent.cgi?article=2303

3. Multi-Domain Impedance Matching Applied to a Bridge Vibration Energy Harvester

Mark E. Hofacker, Alexander V. Pedchenko, and Eric J. Barth

Vanderbilt University

Nashville, TN

From: Journal of Applied Energy

Status: To Be Submitted January 2014

Prologue

This second paper on the bridge vibration energy harvester extends considerations of the source impedance to include electrical dynamics and modifies the mechanical mounting configuration. The resulting ideal matched load impedance contained unstable poles resulting in an unstable and therefore not implementable system. A stable load was developed to approximate the unstable ideal load while still matching the source impedance in the frequency range of interest. The impedance view of the harvester is shown in Figure 3.1.

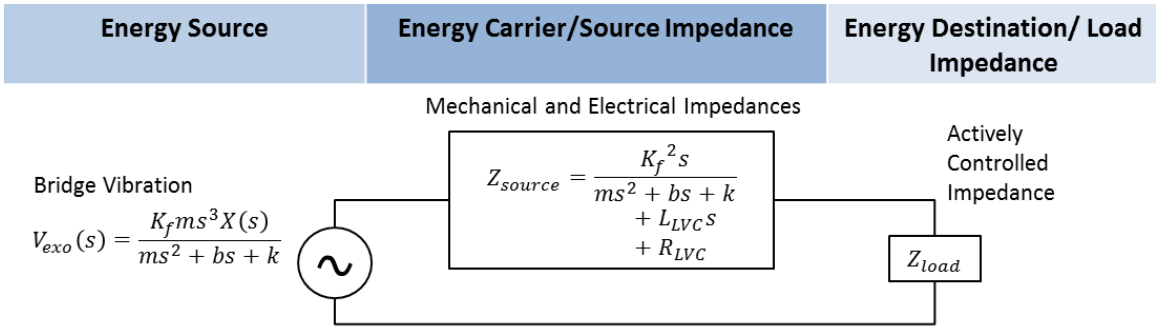

Figure 3.i – Electrical circuit approximation of the bridge vibration energy harvester with electrical and mechanical components

By considering the electrical resistance, the nature of the problem changes significantly. In Chapter 2, the harvester's ideal load could be directly implemented because the complex conjugate of the source impedance was stable. When electrical resistance is considered, however, the source's complex conjugate becomes unstable and direct implementation becomes impossible. This paper describes a method of addressing this challenge through constrained optimization.

A key observation in this manuscript is that the load must be matched inside the energy domain where power is delivered. In this project, the energetic destination is electrical impedance which necessitated the conversion of mechanical bridge vibration into an exogenous voltage input. Simulated results are presented that demonstrate benefits of active control even in the presence of regeneration inefficiencies.

Abstract

A controlled vibration energy harvester is designed to power a node of a bridge condition monitoring sensor network. Typically such vibration energy harvesting is done by matching a passive electrical network using impedance matching. This results in excellent power harvesting at the natural frequencies of the system, but power harvested from other frequencies present is negligible. The approach presented here formulates an active load impedance to broaden the spectrum of frequencies harvested. A multi-domain impedance matching technique is derived from the maximum power transfer theorem. This approach results in a canonically maximum power harvesting load but results in an unstable closed-loop system and cannot be implemented. Constrained optimization is used to find a controller that results in a stable closed-loop system while approximating the broad spectrum properties of the canonical load impedance. The controller has advantages over other approaches because the component excitation frequencies are not found explicitly using the Fourier transform, thereby allowing fast real-time implementation. Additionally, the proposed approach allows for the harvesting of energy from multiple frequency components simultaneously that is typically not seen in the literature. This control approach is validated in simulation and a prototype bridge energy harvester is presented as a platform for experimental validation. The results of this validation will be presented in the second portion this two-part paper.

I. Introduction

In 2009 the U.S. Department of Transportation rated 71,179 bridges as structurally deficient and 78,468 bridges as functionally obsolete; in combination, these numbers represents about 25% of all the bridges in the United States [1]. Additionally, bridges are currently visually inspected only biennially [2]. It is well recognized that the current state of bridge monitoring needs improvement, as noted by a 2001 report which recommended that many at risk bridges should be actively monitored utilizing bridge health sensing equipment to detect approaching failure [3]. There are multiple methods used to monitor bridge health including the use of strain gauges at key locations, monitoring acoustic emissions from the bridge, and pattern recognition of bridge acceleration data.

These methods all require electrical power to enable sensing and data transmission. Wiring electrical power and communication lines to the sensors would be difficult and expensive [4], so ideally power would be provided locally. Although batteries are an option, the need to replace or recharge them periodically motivates a more maintenance-free solution, such as local power generation. Solar and wind

power generation options are avoided, as their application limits the mounting options available on the bridge, and the available power does not necessarily coincide with power demands for sensing.

Thus an electromechanical harvester that harvests energy from the bridge's vibrations was chosen as the power source. Conceptually, this device needs little maintenance, decreases the length of necessary electrical leads to the sensing elements possibly to zero, and is guaranteed to generate power during periods when the bridge sees large dynamic loading. The three most prevalent forms of electromechanical harvesting are electrostatic, piezoelectric, and electromagnetic [5, 6, 7]. For the presented application, an electromagnetic harvester was chosen due to its relatively greater robustness and controllability [8]

Electromagnetic generators are similar in behavior to a mass-spring-damper system. Vibrational energy is transmitted through spring elements to the proof mass which moves relative to the bridge. A damping element is used to extract power from this relative movement. The inherent disadvantage is that they are typically only able to harvest significant power near the system's natural frequency [5]. This is problematic because different bridges vibrate at different frequencies [9], frequencies present in the vibration of a particular bridge will vary depending on traffic conditions [10], and because at a given harvester mounting point, the bridge will oscillate at several frequencies simultaneously [9].

This paper describes a method to overcome these challenges through actively controlling the movement of the proof mass. Cross domain impedance matching techniques are used with the maximum power transfer theorem to determine the ideal controller to increase the bandwidth in which appreciable energy harvesting occurs. Although the ideal control law was found to be unstable, a practical, stable controller was derived and is presented in this paper. This control methodology is validated using simulation. A custom low-friction prototype electromagnetic harvester is presented; it will serve as the platform for experimental validation, which will be the subject of the 2nd part of this paper.

II. Dynamic Model of Electromagnetic Vibration Energy Harvester

A schematic of a typical electromagnetic vibration energy harvester with linear components is shown below in Figure 3.1. In Figure 3.1-i, *x(t)* represents the input excitation (i.e., bridge displacement) , *m* represents the effective proof mass of the harvester, *b* represents parasitic mechanical viscous damping, *k* represents the overall stiffness responsible for suspending the proof mass, *y(t)* represents absolute displacement of the proof mass, and *p(t)* represents the relative displacement of the proof mass with respect to the bridge. The "Linear mot/gen" represents a linear motor/generator used to collect power as well as affect the position of the proof mass during active control, it has a back emf/motor constant K_f.

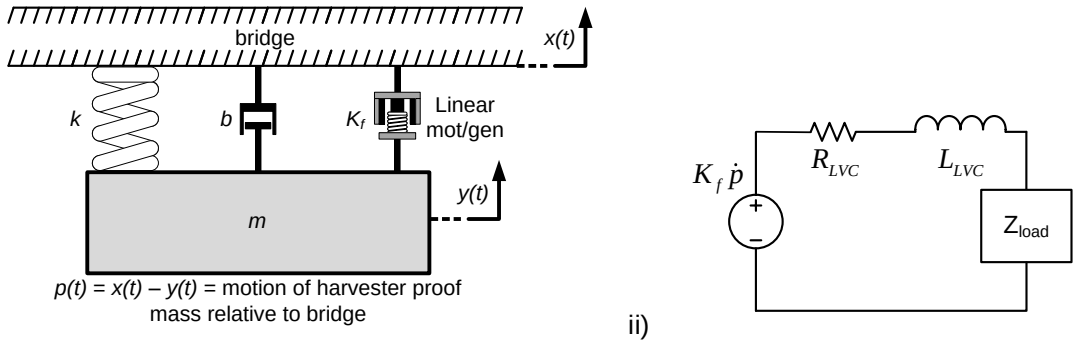

Figure 3.1 – Lumped parameter representation of a vibration energy harvester's components: i) mechanical components; ii) electrical components

The electrical components are shown in Figure 3.1-ii. These components include the voltage generated by the motion of the proof mass $K_f\dot{p}$, the motor/generator's winding resistance and inductance, R_{LVC} and L_{LVC} respectively (LVC subscript stands for linear voice coil), and the complex impedance used to extract power and control the harvester Z_{load}. The dynamics governing the mechanical and electrical domains are described by (1) and (2).

$$m\ddot{x} = m(\ddot{x} - \ddot{y}\,) + b(\dot{x} - \dot{y}) + k(x - y) + K_f\, I = m\ddot{p} + b\dot{p} + kp + K_f I \tag{1}$$

$$K_f\dot{p} = L_{LVC}\dot{I} + R_{LVC}I + Z_{load}I \tag{2}$$

Laplace transforms of (1) and (2) are shown in (3) and (4) respectively.

$$(ms^2 + bs + k)P(s) = ms^2X(s) - K_fI(s) \tag{3}$$

$$V(s) = sP(s)K_F = (L_{LVC}s + R_{LVC} + Z_{load})I(s) \tag{4}$$

Equations (1)-(4) describe the behavior of the harvester in terms of its mechanical and electrical system parameters, the attached electrical impedance, and the bridge excitation. These equations were verified on the experimental platform presented in the next section. They are then subsequently used to develop an active control scheme to increase the harvester's power generation.

III. Experimental Setup

An electromagnetic harvester as shown in Figure 3.3 was designed and built to serve as an experimental platform. It was designed to minimize parasitic, frictional losses through the use of compliant

mechanisms that suspend and align a magnet within a coil. In this manner the linear motor (linear voice coil: LVC) is constrained to translate along its intended axis without rubbing against the coil which is rigidly attached to the bridge. The alignment is accomplished without the use of a bearing surface and its associated parasitic loss. In this configuration, the housing of the LVC also serves as a proof mass, the relative motion of which provides power.

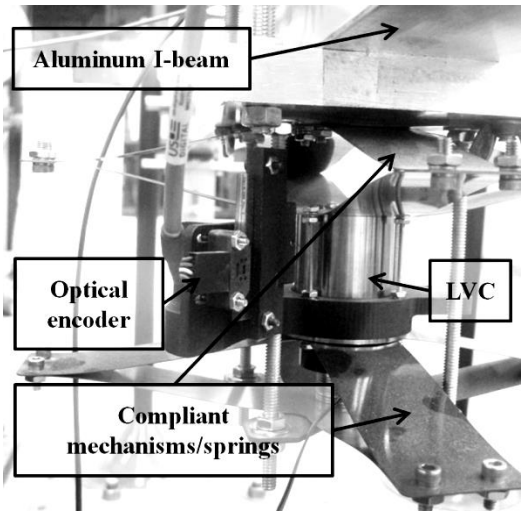

Figure 3.3 – Electromagnetic vibrational energy harvester experimental setup

The compliant mechanisms were approximated as beams that are cantilevered at one end and constrained to translate in the vertical direction at the other so that their stiffness could be calculated [11]. The width, length, and thickness of the compliant mechanisms were designed such that, when used with the measured proof mass, the harvester would have a natural frequency close to the upper bound of the frequency range of interest. Bridges dominant modes of oscillation are typically in the range of 3-12 Hz [12, 13, 14].

To enable actively controlled harvesting, the harvester was instrumented with two sensors: an optical encoder to measure the movement of the proof mass (housing of the LVC) relative to the bridge and an accelerometer to measure the excitation of the bridge. The harvester is mounted on a simply supported aluminum I-beam, which is rigidly attached to an electromagnetic shaker at its midpoint. Operation of the shaker causes the beam to oscillate, thereby emulating bridge vibration. To efficiently store energy captured by the harvester and to actively adjust the load, a circuit board with a bank of supercapacitors and a servo amplifier were also mounted to the aluminum beam. This board and the accelerometer circuit are shown attached in Figure 3.4.

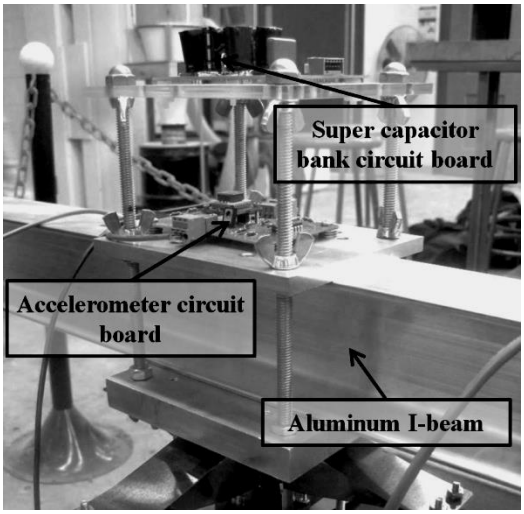

Figure 3.4 – Photograph of top portion of the vibrational energy harvester

Parameters of Equations (3) and (4) were measured or determined experimentally and are shown below in Table 3.1.

Table 3.1 – Vibration Energy Harvester Parameters

Parameter	Value
m	0.668 kg
b	7.074 N/(m/s)
k	1700 (N/m)
K_f	17.8 (N/A) or (V/(m/s))
L_{LVC}	0.0031 H
R_{LVC}	7 Ohms

The linear voice coil's motor constant K_f, and inductance L_{LVC}, were taken directly from its data sheet (BEI Kimco LA17-28-000A). The motor's resistance R_{LVC}, was directly measured. The proof mass m, mechanical parasitic damping b, and equivalent stiffness k were determined from the second order linear model of Equation (3) where the electrical leads were left open to remove the $K_f I(s)$ term. The system was then subjected to a chirp excitation, and the measured bridge acceleration and relative position were used as inputs and outputs to determine m, b, and k using a standard parameter estimation approach.

Once the parameters were determined, the coupled system (3) and (4) was validated. To do this Z_{load} was selected as purely resistive by attaching a resistor measured as 50.6 Ohms. The choice of the resistance value was not arbitrary and will be discussed further in the paper. Equations (3) and (4) can be used to obtain a transfer function between the excitation displacement and the relative position of the proof mass as shown in (5):

$$\frac{P(s)}{X(s)} = \frac{ms^2\left(L_{LVC}s+(R_{LVC}+R_{load})\right)}{(ms^2+bs+k)\left(L_{LVC}s+(R_{LVC}+R_{load})\right)+K_f^2 s} \tag{5}$$

Note that in obtaining (5), Z_{load} was replaced by R_{load} to reflect the purely resistive nature of the attached load. Substituting the values from Table 3.1 and the 50.6 Ohm R_{load} into (5) above, yields the theoretical response of the harvester shown as the Bode plot depicted in Figure 3.5 below. Experimentally obtained data is plotted on the same plot; it shows good agreement with the model and its parameters, within the frequency range of interest.

With experimental data validating the model, the use of equations (1)-(4) in the derivation of a control scheme to maximize power generation for the harvest is justified.

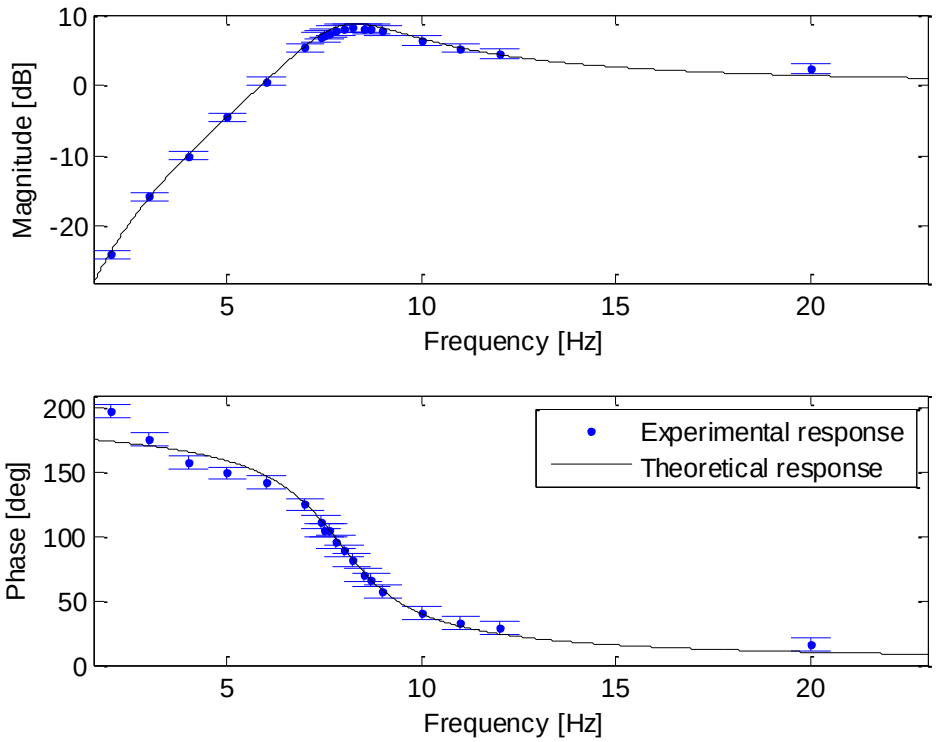

Figure 3.5 – Bode plot of the relationship between input excitation displacement and the relative position of the proof mass

IV. Active Load Adjustment Control

Impedance matching principles from the maximum power transfer theorem were utilized to determine the Z_{load} which would maximize the power harvested from bridge motion. A brief overview of the maximum power transfer theorem will aid in understanding the control techniques used in this paper.

The application of the theorem is most common in single domain systems, such as the example circuit shown in Figure 3.6. The voltage source V_S is exogenous, such as the bridge being an exogenous source of displacement. That is to say that in the depicted circuit, as well as in the case of the harvester, the energy source is considered ideal. The internal dynamics of the circuit can exert no influence on the voltage supplied by the voltage source as the displacement of the bridge to which the harvester is

attached is not appreciably affected by the behavior of the harvester.

The circuit is divided into a source and a load impedance, with components belonging to the former being denoted with a subscript S, and components that are part of the latter being denoted by a subscript L. All of the circuit components belong to one of two impedances (Z_S and Z_L), These impedances consist of resistive, dissipative components (R_S and R_L), capacitive components (C_S and C_L), and inductive components (L_S and L_C). The capacitive and inductive components are conservative elements and are referred to collectively as reactive components (X_S and X_L). Reactive elements represent complex impedance and are therefore frequency dependent. The source and load impedances are both shown as second order for purposes of illustration, but in general could be of any dynamic order.

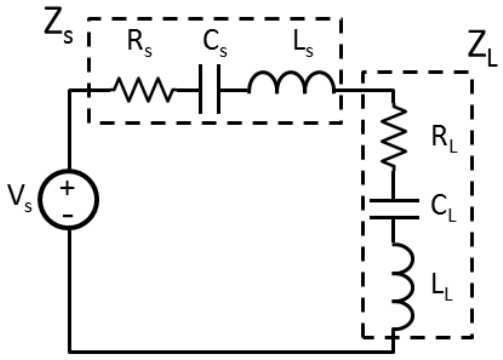

Figure 3.6 – Circuit with a voltage source and a load and source impedance

By properly matching the load impedance to the source impedance (Z_s), a maximum amount of energy can be transferred to the load impedance (Z_L). According to the maximum power transfer theorem, this is accomplished by setting the load impedance equal to the complex conjugate of the source impedance.

In order to apply this methodology to the harvester to maximize the power it delivers to the attached load, the components from its governing dynamics shown in (3) and (4) were separated into an exogenous effective voltage input, $V_{exo}(s)$, a source impedance, Z_{source}, and a load impedance, Z_{load}. This form of the harvester's dynamics is shown in (6).

$$V_{exo}(s) = \frac{K_f m s^3 X(s)}{ms^2+bs+k} = \left(\frac{{K_f}^2 s}{ms^2+bs+k} + L_{LVC}s + R_{LVC} + Z_{load}\right) I(s) = (Z_{source} + Z_{load}) I(s) \qquad (6)$$

In purely electrical systems, (6) describes a Thévenin equivalent circuit. Figure 3.6 shows (this circuit.

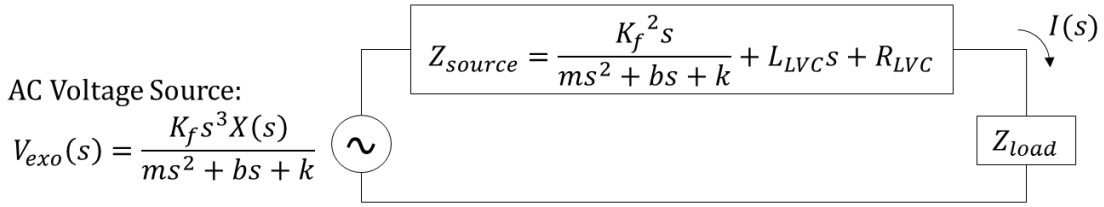

Figure 3.6 – Thévenin equivalent circuit representation of harvester.

This organization of components by representing the system entirely in the electrical domain and equating the voltage source (effort source) to the product of the system's impedance and current (flow) may at first seem arbitrary. Stephan, however, noted that it is necessary to perform load matching in the domain where power is being delivered [15]. In the case of the harvester, power is delivered to an electrical load/electrical impedance, so it is necessary to perform impedance matching in the electrical domain.

The ideal load, $Z_{load,ideal}$, was obtained by taking the complex conjugate of the source impedance Z_{source}, i.e., replacing every "s" term with "-s" as shown in (7).

$$Z_{load,ideal} = \frac{{K_f}^2(-s)}{m(-s)^2+b(-s)+k} + L(-s) + R_C = \frac{-{K_f}^2 s}{ms^2+b(-s)+k} - Ls + R_C \quad (7)$$

This load is unstable itself and, when incorporated into the overall system model, results in an unstable closed-loop system. Although this means that the load from (7) is impossible to practically implement, its equation yielded the magnitude and phase of a power maximizing electrical load. Using this information allowed the calculation of the harvester's upper bound of power generation. This upper bound was used to help derive a practically implementable control law and to evaluate that control law's performance by comparing its power generation to that of $Z_{load,ideal}$ case, which is the theoretical maximum.

As an additional comparison, the power generation for an ideal resistive load, $Z_{load,ideal,passive}$ was calculated. $Z_{load,ideal,passive}$ was found by setting it equal to the resistive portion of the source impedance as shown in (8). This agrees with the findings of Stephan for calculating the ideal passive load for a system that has reached steady state [15]. $Z_{load,ideal,passive}$ can be viewed as the current technique used for load matching in conventional harvesters. It guarantees maximum power transfer from the excitation source to the harvester at natural frequency. Its lack of a frequency-dependent portion to the load is what makes traditional electromagnetic vibrational energy harvesters so dependent on their excitation frequency being at or very close to the natural frequency of the harvester.

$$Z_{load,ideal,resistive} = \frac{{K_f}^2}{b} + R_c \quad (8)$$

Since the derivation of the control law was dependent on (7), it was important to confirm that the complex load described by (7) is in fact the ideal electrical load that results in maximum power generation across the harvester leads. To do this, an analytic expression for average generated power was derived. The derivation was accomplished under the assumptions that the effect of the inductor is negligible in the chosen frequency range of interest (3-12 Hz) and that the electrical load should respond with a sinusoidal voltage of the same frequency as that of the input excitation. The inductor assumption was based on the component's relatively very small value of 3.1 mH. The validity of the assumption was also confirmed in simulation. The harvester's relative proof mass motion, the current across its windings and its average generated power showed negligible difference in their simulation frequency response behaviors between the case when the inductor term was included and the case when it was neglected for frequencies up to 1000 Hz. The sinusoidal voltage response of the load assumption is based on the fact that the behavior of the harvester is quite linear. This fact will also allow the complex load of the harvester to be implemented via a linear control law. Under the assumption of a linear system, the voltage across the load can be assumed to be composed of the same frequencies as the excitation frequency components, where the magnitude and phase of the load voltage are altered by a frequency dependent amount. For the theoretical confirmation below, it was more convenient to express this amplitude and phase as the sum of a sine and a cosine term. Therefore the equation governing the harvester's electrical dynamics in response to each excitation frequency component ω becomes the following:

$$K_f\dot{p} = R_{LVC}I + V_{load} = R_{LVC}I + M\sin(\omega t) + N\cos(\omega t) \tag{9}$$

where V_{load} is the sinusoidal voltage developed across the harvester load, and M and N are voltage amplitudes, the values of which depend on the frequency (or frequencies) of vibration to which the harvester is subjected. The frequency dependent values of M and N uniquely prescribe the linear load impedance. Finding the values of these variables that maximize the power harvested at each frequency will result in an overall load impedance, which can then be compared to that given by the maximum power transfer theorem. If (9) is then substituted into (1), the harvester's mechanical dynamics take the form of (10).

$$m\ddot{x} + \frac{K_f}{R_{LVC}}(M\sin(\omega t) + N\cos(\omega t)) = m\ddot{p} + \left(b + \frac{K_f^2}{R_{LVC}}\right)\dot{p} + kp \tag{10}$$

The input excitation ultimately allowing the harvester to generate power will be in a sinusoidal form shown in (11):

$$x(t) = -A\sin(\omega t) \tag{11}$$

where A is the amplitude of the excitation's displacement and ω is the excitation's frequency in radians

per second. It is important to note here that although it is quite possible that the input excitation will consist of several frequency components (i.e., several inputs having the form of (11) added together), the following derivations and conclusions still hold because the harvester's behavior is represented by a linear system, meaning that the principle of superposition applies. Because the harvester's input is sinusoidal in nature and the harvester is a linear system, the average power generated by the harvester can be found by averaging the power flowing into the harvester's electrical load over a period of excitation. This is shown in (12):

$$\overline{\mathbb{P}} = \frac{\omega}{2\pi}\int_0^{2\pi/\omega} V_{load} I dt = \frac{\omega}{2\pi}\int_0^{2\pi/\omega} \frac{K_f \dot{p}(t) V_{load}(t) - V_{load}^2(t)}{R_{LVC}} dt \tag{12}$$

In order to obtain a solution for (12) given a specific input excitation in the form of (11) and a V_{load} dictated by choosing some values for M and N, it is first necessary to obtain $\dot{p}(t)$. $\dot{p}(t)$ is obtained by finding the closed form solution to the second order ODE in $p(t)$ formed by substituting in the second derivative of (11) into (10):

$$m\ddot{p} + \left(b + \frac{K_f^2}{R_{LVC}}\right)\dot{p} + kp = \left(mA\omega^2 + \frac{MK_f}{R_{LVC}}\right)\sin(\omega t) + \left(\frac{NK_f}{R_{LVC}}\right)\cos(\omega t) \tag{13}$$

In obtaining the closed form solution to $p(t)$ from (13), only the steady-state part of the solution is kept. This assumption corresponds to a constantly moving, regular flow of traffic traversing the bridge to maintain steady-state excitation. This solution is shown in (14), where ψ and λ are defined by (15) and (16) respectively.

$$p(t) = \psi \sin(\omega t) - \lambda \cos(\omega t) \tag{14}$$

$$\psi = \frac{(k - m\omega^2)\left(mA\omega^2 + \frac{MK_f}{R_{LVC}}\right) + \omega\left(b + \frac{K_f^2}{R_{LVC}}\right)\left(\frac{NK_f}{R_{LVC}}\right)}{(k - m\omega^2)^2 + \left(b + \frac{K_f^2}{R_{LVC}}\right)^2 \omega^2} \tag{15}$$

$$\lambda = \frac{-\omega\left(b + \frac{K_f^2}{R_{LVC}}\right)\left(mA\omega^2 + \frac{MK_f}{R_{LVC}}\right) + (k - m\omega^2)\left(\frac{NK_f}{R_{LVC}}\right)}{(k - m\omega^2)^2 + \left(b + \frac{K_f^2}{R_{LVC}}\right)^2 \omega^2} \tag{16}$$

Differentiating (14) with respect to time and substituting the result into (13) yields the closed-form solution of the harvester's average generated power as a function of the excitation input $x(t)$ and the chosen voltage amplitude coefficients M and N:

$$\overline{\mathbb{P}} = \frac{K_f N\psi\omega - K_f M\lambda\omega - M^2 - N^2}{2R_{LVC}} \quad (17)$$

Using the Matlab R2013a minimization function 'fminsearch' (unconstrained minimization of a multi-variable function based on the Nelder-Mead simplex algorithm described in Lagarias et al. [16]), the frequency dependent values for M and N were solved for such that (17) was maximized. Their magnitudes determine the frequency response behavior of the voltage of the ideal electrical load; this load would result in maximum average power generation for a given harvester. Plotting the frequency response of this load as an impedance (voltage response to current) on the same plot as the load defined by (7) confirms that the latter is in fact the ideal load (in terms of power generation) for the system. This confirmation validated the use of (7) in the derivation of a stable and practically implementable control law to maximize the achievable power generation of the harvester.

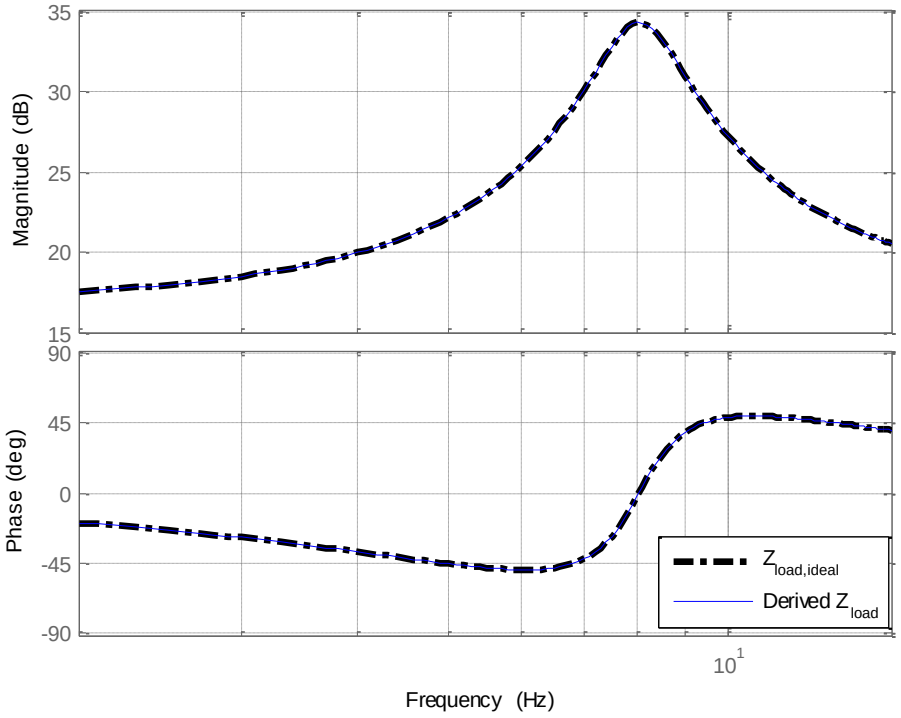

Figure 3.7 – Frequency-dependent behaviors of the power maximizing load based on the complex conjugate of the source impedance ($\boldsymbol{Z_{load,ideal}}$) and based on maximizing (17) denoted as "Derived $\boldsymbol{Z_{load}}$"

V. Broad-Bandwidth Stable Controller

Using the 'fminsearch'-based algorithm, a stable alternative to $Z_{load,ideal}$ from (7) was sought to accomplish the goal of broad bandwidth power generation. This was accomplished by modifying the

constrained optimization algorithm that maximized power generation in the frequency range of interest. The algorithm was constrained in its search for the ideal impedance's gain, poles, and zeros. To ensure causality, the impedance was constrained to have a relative order of zero or greater. To ensure stability, the poles of the closed-loop load voltage in response to the exogenous voltage source (18) were constrained the left half plane.

$$V_{load}(s) = \frac{Z_{load}}{Z_{source}+Z_{load}} V_{exo}(s) \tag{18}$$

For the parameters listed in Table 3.1, the following load was found to produce the maximum amount of power for the frequency range of interest (between 3 and 12 Hz).

$$Z_{load,stable} = 67.9 \frac{(s^2+67.46s+4688)}{(s^2+181s+8192)} \tag{19}$$

VI. Simulated Results

The power generated by the harvester utilizing the load (which can be viewed as a stable active controller) (19) is normalized with respect to the power generated using the conventional approach of a passive, tuned load described by (8). Additionally, the proposed control scheme's power generation is compared to the power that would be generated by the upper bound of the unstable, ideal controller (7) if it was implementable. This comparison is depicted in Figure 3.8.

It's important to note that the effectiveness of the active controller to surpass the power generation yield of the traditional passively tuned approach is dependent on the regenerative efficiency of the servo amplifier and the capacitor bank. That is to say that in comparing the passive load impedance case to active control, it is important to note that whereas power flows from the harvester to the load in both cases, power flows from the load to the harvester only during active control. Therefore the actively controlled case is adversely affected by an associated efficiency of regeneration, but the passive case is not. In comparing the performance of the active case to the passive in Figure 3.8, regeneration efficiencies were applied only when power was flowing from the load to the harvester during control.

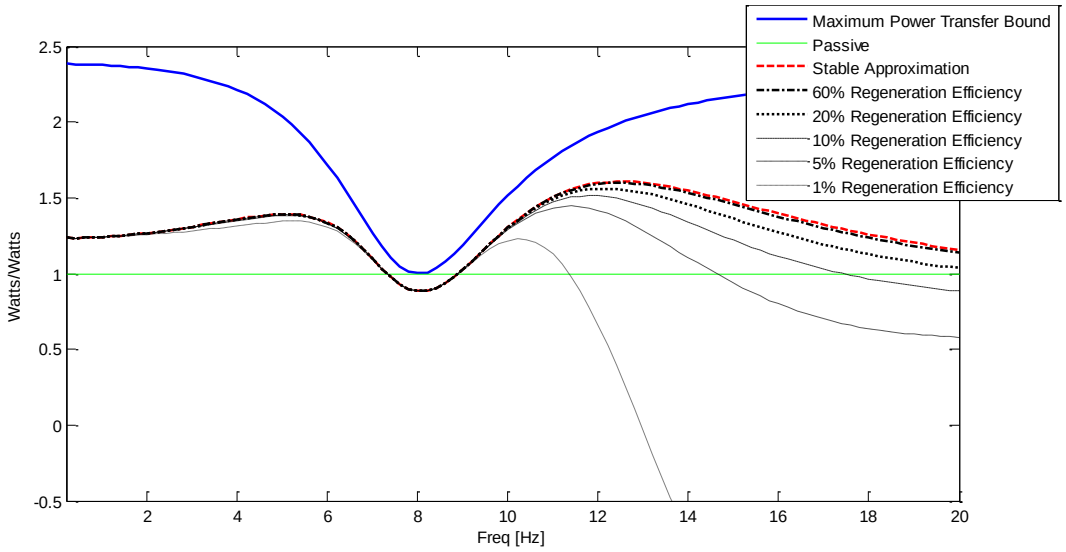

Figure 3.8 – Power generated by harvester with different control techniques normalized to power generated by passive, resistive control

To further assess the increase in power generation from the use of the proposed controller, the harvester's response to realistic bridge vibrations was simulated. Data recorded from an accelerometer on the bridge spanning Howe Ditch on US 231 represented in fast Fourier transform from [9] was used to create a representative acceleration profile to be used as excitation input. This profile contained appreciable frequency components at 5, 7, 12, and 20 Hz. Using this input data in conjunction with the control performance data presented in Figure 3.9, it was possible to calculate the theoretically maximum amount of power that could be harvested if it was possible to use$Z_{load,ideal}$. Using simulation, the power generated from this same acceleration profile was calculated using $Z_{load,stable}$ and $Z_{load,ideal,resistive}$. The predicted power generation results are shown in Figure 3.9. As in Figure 3.8, the power generated for varying levels of regeneration efficiency is shown for the proposed control law case.

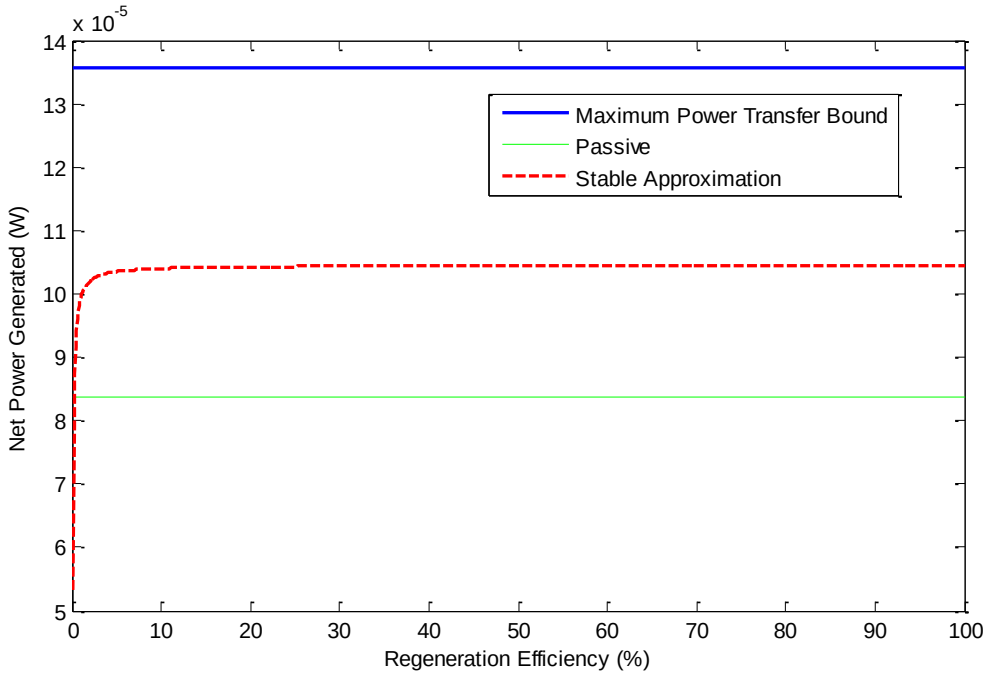

Figure 3.9 – Predicted power generated by active controlled harvester with varying levels of regeneration efficiency in response to an acceleration profile compared to passive control and ideal, unstable control

It can be seen from Figure 3.9 that even at single digit regeneration efficiencies, the proposed active control law surpasses the power generation of the harvester using the conventional passive tuned load approach.

VI. Conclusions

This paper presents an electromagnetic bridge vibration energy harvester intended to power bridge health sensing and communications electronics. By connecting a proof mass to the bridge through a compliant mechanism, energy can be captured from the relative movement between the bridge and this proof mass. This extraction of power from inherent bridge vibrations allows to a bridge's health to be actively monitored without the difficulty and expense of wiring additional electrical power lines to the bridge, or the need for periodic battery replacement in the sensors. Unlike conventional vibration energy harvesters, active control allows the proposed harvester to capture appreciable energy in a certain bandwidth of frequencies, as opposed to a narrow frequency range around a single pre-determined frequency value.

This paper presents the design of a harvester that utilizes compliant mechanisms to eliminate the need of bearing surfaces and to reduce frictional losses. A linear motor was utilized as a proof mass, a means of harvesting electrical energy, and an actuator which can be used to actively control the harvester.

An unstable, canonical control law for the harvester was derived using multi-domain impedance matching techniques from the maximum power transfer theorem. This controller was confirmed to

produce maximum power for the given harvester by analytically determining the harvester's power generated given a particular linear control law/electrical load. An implementable, stable controller was then derived using constrained optimization. Power generation for this controller is simulated and compared to the power generated using the conventional load matching technique and the power that could theoretically be calculated with the unstable, ideal controller. Simulation results indicate that the proposed control law yields superior harvester power generation when compared to a harvester using conventional, passive load matching. This result holds even for quite low regeneration efficiencies. Experimental validation of the presented simulation results will be presented in the second part of this two-part paper.

References

[1] U.S. Dept. of Transportation. "Our Nation's Highways: 2010," Web. <http://www.fhwa.dot.gov/policyinformation/pubs/hf/pl10023/fig7_3.cfm>.

[2] T. Galchev, J. McCullagh, R. L. Peterson, K. Najafi, "Harvesting Traffic-Induced Bridge Vibrations," Conf. Rec. 2011 IEEE Transducers' 11, pp 5-9, June 2011.

[3] O'Connell, Heather M.; Dexter, Robert J.; Bergson, Paul.; , "Fatigue Evaluation of the Deck Truss of Bridge 9340 - CTS Research Reports."Center for Transportation Studies. University of Minnesota, 2007. Web.

[4] J.P. Lynch, et al., "Design and performance validation of a wireless sensing unit for structural monitoring applications," *Structural Engineering and Mechanics,* vol 17, no. 3-4, 2004, pp. 393-408.

[5] Beeby, S. P., M. J. Tudor, and N. M. White. "Energy Harvesting Vibration Sources for Microsystems Applications."Meas. Sci. Technol.17 (2006): 175-95. IOPscience. Web.

[6] Chalasani, S.; Conrad, J.M.; "A survey of energy harvesting sources for embedded systems, "Southeastcon, 2008. IEEE, vol., no., pp.442-447, 3-6 April 2008

[7] Moghe, R.; Yi Yang; Lambert, F.; Divan, D.; "A scoping study of electric and magnetic field energy harvesting for wireless sensor networks in power system applications,"Energy Conversion Congress and Exposition, 2009. ECCE 2009. IEEE, vol., no., pp.3550-3557, 20-24 Sept. 2009

[8] Pedchenko, A.V., Hoke J. W., and Barth E. J. "A Control Approach for Broadening the Operating Frequency Range of a Bridge Vibration Energy Harvester," Paper accepted for the 2011 ASME Dynamic Systems and Control Conference, in press. Nov. 2011

[9] A. Shahabadi, (1977) . Bridge Vibration Studies: Interim Report. Purdue e-Pubs [Online] pp. 108-130 Available:http://docs.lib.purdue.edu/cgi/viewcontent.cgi?article=2303

[10] Williams, C. B., A. Pavic, R. S. Crouch, and R. C. Woods. "Feasibility study of vibration-electric generator for bridge vibration sensors," Vibration Engineering Research Section, University of Sheffield. Society for Experimental Mechanics. Web. <http://vibration.shef.ac.uk/pdfs/IMAC_XVI_3.pdf>.

[11] Howell, L.L., *Compliant Mechanisms*, John Wiley & Sons, New York, NY, 2001. pp. 410

[12] Sazonov, E.; Haodong Li; Curry, D.; Pillay, P.; "Self-Powered Sensors for Monitoring of Highway Bridges,"Sensors Journal, IEEE, vol.9, no.11, pp.1422-1429, Nov. 2009

[13] Gioffrè, M., et. al., "Comparison Between Accelerometer and Laser Vibrometer to Measure Traffic Excited Vibrations on Bridges", *Shock and Vibration* Vol. 9, Issue: 1-2, pp. 11-18. 2002

[14] Wang, M. *Embedded Strain Sensor With Power Scavenging From Bridge Vibration,* M.S. Thesis, University of Maryland. pp. 13. 2004.

[15] Stephan, N.G., "On the maximum power transfer theorem within electromechanical systems", *Journal of Mechanical Engineering Science*, vol. 220 no. 8, pp. 1261-1267. Aug. 1, 2006.

[16] Lagarias, J.C., et. al., "Convergence Properties of the Nelder-Mead Simplex Method in Low Dimensions", *SIAM Journal on Optimization*, Vol. 9, No. 1, pp. 112-147. 1998.

4. Design and Validation of a Figure-Eight Free-Liquid-Piston Engine Compressor for Compact Robot Power

Eric J. Barth, Mark E. Hofacker, Nithin Kumar

Vanderbilt University

Nashville, TN

From: ASME Dynamic Systems and Control Vol. 1 No. 2

Status: Published June 2013

Prologue

The impedance view of the free piston engine compressor is shown in Figure 4.i. Within the scope of the overall impedance framework proposed by this dissertation, the work presented on the free piston engine compressor primarily concerns the energetic source and the source impedance. The goal of matching the source impedance led to design consideration regarding the inertance of the liquid piston and its balanced configuration. A consideration of establishing a periodic energy source influenced the design and control of injection and exhaust valves.

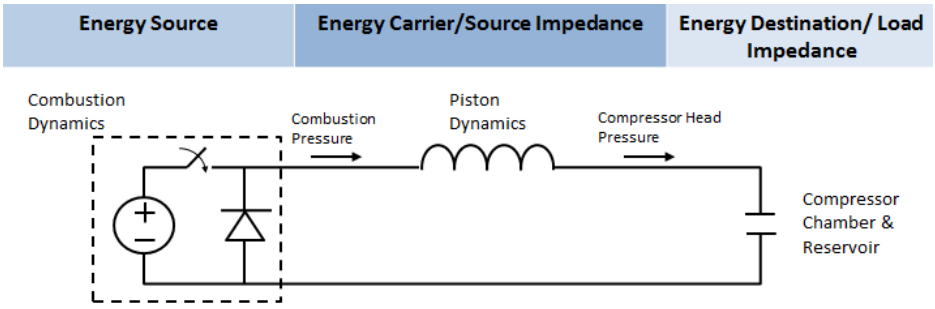

Figure 4.i – Electrical circuit approximation of the free piston engine compressor as a buck converter

This manuscript is a brief overview of the free piston engine compressor project. It shows how the device has evolved over three generations and the logic behind the changes. Chapter 5 presents a more detailed account of this project.

I. Introduction

Human scale robots operating below 1 kW are commonly powered by batteries. Given the low energy density of state-of-the-art rechargeable batteries, operational times of these systems are on the order of

15 to 30 minutes [1]. The low energy density problem of such systems is often compounded by low power density actuation, resulting in a heavy system that consumes the potential to perform tasks beyond basic mobility. What is needed to break this technological barrier is a system with a high energy density portable power source coupled to a high power density form of actuation.

One such system with an alternative energy source and actuation is seen on Boston Dynamic's BigDog, which utilizes an internal combustion engine/hydraulic pump and hydraulic actuation system. BigDog's engine provides about 10kW of power for over 2.5 hours [2]. However, it is difficult to scale this approach down due to the mass of the working fluid as well as components such as return lines, accumulators, control valves, and hosing.

An energy source that provides pneumatic power presents an appealing alternative that alleviates many of the scalability problems of hydraulics while preserving a high actuation power density. Current small scale engines coupled to compressors present an unreasonably low system efficiency and resulting low energy density. The free piston engine/compressor (FPEC) presented here combines the engine and the compressor into a single unit. This approach achieves an adequately efficient transduction from chemical potential to pneumatic potential energy by presenting a dynamic load provided by the liquid piston while reducing the overall mass of the conversion system relative to a conventional solution. The system also presents additional advantages such as power-on-demand with no idle. By achieving even a modest efficiency and a reasonable FPEC mass, the high energy density of hydrocarbon fuels (~45 MJ/kg) results in a system energy density many times that of the best batteries (~700 kJ/kg).

Free piston engine compressors operate by separating a combustion chamber from a compressor head with a "free-piston" which moves in response to the pressure forces on either side. Although this compact means of combining the engine and compressor was invented in 1928 [3], difficulties in control prevented widespread adoption. Controlling the intake and exhaust timings of free-piston engines is challenging because the stroke is not kinematically constrained and the piston position is often difficult to measure. The typical cam-based control seen in non-free-piston engines is therefore not typically available. The FPEC overcomes these challenges by measuring the pressure state in the compressor head [4, 5].

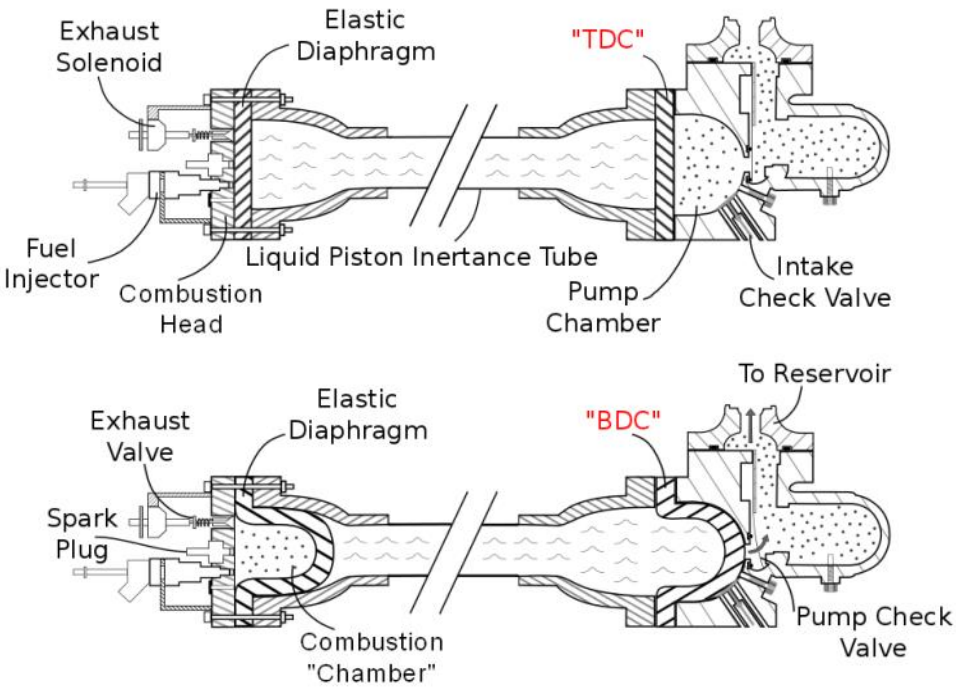

Figure 4.1 - Schematic of the FPEC at (a) effective TDC, and (b) effective BDC

The liquid piston of the FPEC is constructed by trapping water in a pipe between two elastic membranes (high temperature silicone), thereby combining a mass and spring element in a compact package. This arrangement is shown schematically in Fig. 4.1. The liquid piston's cross section is larger at the ends and smaller in the intermediate region, which increases the inertance of the piston while reducing the mass.

Taking advantage of the high inertance piston, high pressure air and high vapor-pressure fuel enables the engine to operate in an "inject and fire" cycle, which differs significantly from 4-stroke or 2-stroke engines. In this inject-and-fire mode of operation, compressed air and fuel is injected against the wall of the piston. The inertia of the piston presents a high dynamic load such that compression is maintained until injection has finished and the spark can ignite the mixture. The combustion pressure accelerates the water through the pipe, expanding the opposite membrane into the compressor head, forcing air into the high pressure air reservoir as shown in Fig. 4.2. The exhaust valve on the combustion head is then opened, the elastic membranes return the piston to its original position, and atmospheric air is breathed into the compressor head. Some of the compressed air is then utilized in the next cycle.

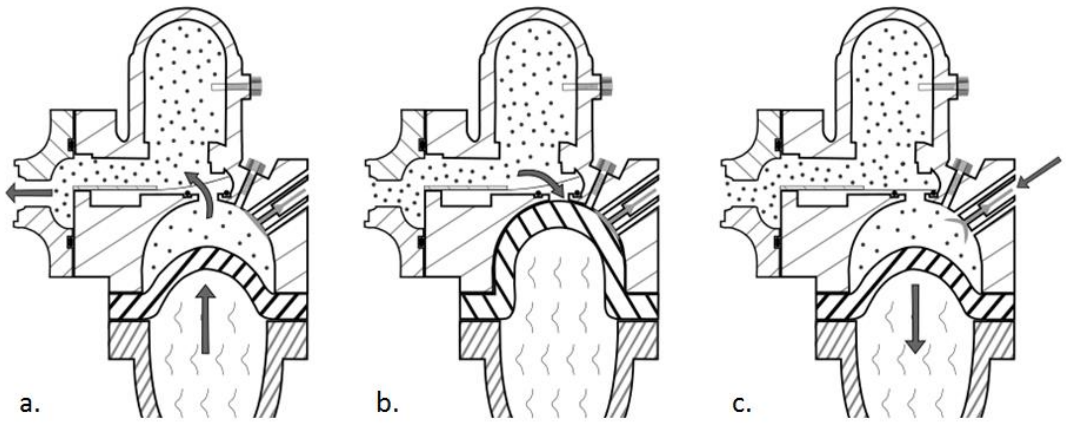

Figure 4.2 - (a) Compressor head while pumping (b) Compressor head at BDC (c) Compressor head during breathe-in

II. Evolution of the Device

The free-piston engine compressor has progressed through three distinct prototypes as shown in Fig. 4.3. Each prototype was modeled and then experimentally validated [6-16]. The validated model of each version was used to guide and refine the design of the next prototype. The main refinement between prototypes one (Fig. 4.3a) and two (Fig. 4.3b) was an increased piston inertance and lower piston mass. The first prototype had a separate combustion chamber that would open to the elastic piston wall in response to combustion pressure. This separated combustion chamber was not necessary in prototype two due to the high dynamic load presented by the inertance to maintain pre-combustion pressure.

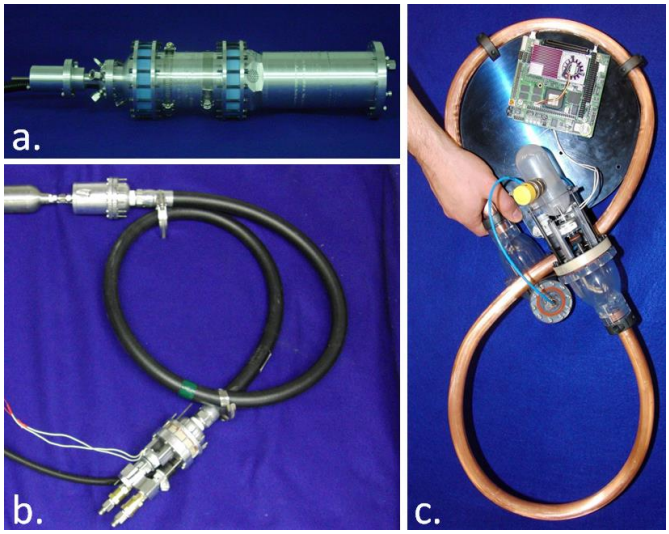

Figure 4.3 - a) Straight Configuration, b) Loop Configuration, c) Figure-8 Configuration. (a, b and c not to scale relative to each other)

The main refinement between the second and third prototype (Fig. 4.3c) was a figure-8 piston configuration to reduce dynamic reaction forces during operation. Distinct from solid piston engines, the liquid piston enables engine balancing in a single piston engine. Table 4.1 shows a comparison of computed force, moment, impulse, and angular impulse for each of the three prototype configurations.

Table 4.1 - Reactions for various liquid piston configurations

Reaction Metric	Straight	Loop	Figure-8
Maximum Force (N)	894	159	103
Maximum Moment (N*m)	0	116	0
Maximum Impulse (N*s)	4.61	1.02	0.533
Max. Angular Impulse (N*m*s)	0	0.567	0

Dynamically, the FPEC is similar to a buck converter circuit (shown in Fig. 4.4) in that the flow is amplified and the high-inertance piston plays the same energetic role as the inductor.

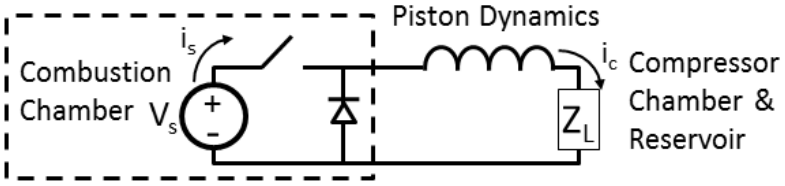

Figure 4.4 - Schematic of the FPEC represented energetically as a buck converter.

In a buck converter, a high voltage/low current source is converted to a low voltage/high current across a load at a high efficiency using an inductor, diode, and a switch. In the FPEC, more mass leaves the compressor head than enters the combustion head. The admitted air and fuel, when combusted, present a high pressure akin to the source voltage of the buck converter. This source then loads the high inertance piston as is done to the inductor in the buck converter. The kinetic energy stored in the piston is then converted to a higher delivered mass at a lower pressure than the source.

III. Experimental Results

The majority of the experimental results presented below are from the second prototype, which contained more extensive instrumentation in order to validate the dynamic system model and fully energetically characterize the device. Mass and size are best characterized by prototype three. As a self-contained device, prototype three included an on-board microcontroller and all supporting electronics, but contained minimal instrumentation. With regard to prototype two, the measured efficiency (lower heating value of propane fuel to pneumatic potential energy) ranged from 3.45% to 6.63% with an output power range of 9.6 W to 17.9 W [16]. A virtual-cam control approach applied to this prototype yielded an improved efficiency range of 4.4% to 8.1% with a pressure output range from 380 kPa to 720 kPa (40 to 90 psig) and slightly higher output power [4, 14]. Prototype three had a mass of 5.9 kg and was able to deliver compressed air up to 1.2 MPa (157 psig), an improvement over prototype two due largely to model-guided design changes in the compressor head check valve and inertance nozzles [17].

Although these efficiencies seem low, it must be remembered that this is the combined efficiency of

an internal combustion engine and a compressor, all in a relatively small package. The data suggests that pneumatic systems using the FPEC as a power source would exhibit system energy densities comparable to, if not better than, the best electromechanical systems. The experimentally demonstrated energy density of the FPEC ranges from 2040 kJ/kg to 3750 kJ/kg (resulting stored pneumatic potential energy per kilogram of fuel) compared to about 700 kJ/kg for Li-ion batteries. Accounting for roughly 50% efficiency of the actuation (pneumatic actuators or motors with gearheads), this translates to a specific work of 1020 kJ/kg to 1875 kJ/kg for the FPEC powered system with pneumatic actuators, compared to about 350 kJ/kg for a Li-ion battery powered system with DC servomotors. Combined with the inherent power-density and therefore weight advantages of pneumatic actuators over DC servomotors, devices like the FPEC position pneumatically actuated systems as an attractive option for human-scale, untethered robotic systems. Further design and control optimization of the FPEC is also possible.

Acknowledgment

This work was supported by the Center for Compact and Efficient Fluid Power, an NSF Engineering Research Center, grant EEC-0540834.

References

[1] Dunn-Rankin, D., Leal, E. M., and Walther, D. C., (2005) “Personal Power Systems”. *Progress in Energy and Combusion Scence*, vol. 31, pp. 422–465.

[2] Raibert, M. (2008) “BigDog, the Rough-Terrain Quadruped Robot”. *Proceedings of the 17th World Congress, International Federation of Automatic Control (IFAC)*, vol. 17, no. 1, part 1.

[3] Pescara, R. P., (1928) “Motor Compressor Apparatus,” *U.S. Patent No. 1,657,641*.

[4] Yong, C.; Riofrio, J. A. and Barth, E. J. (2008) “Modeling and Control of a Free-Liquid-Piston Engine Compressor,” *Bath/ASME Symposium on Fluid Power and Motion Control (FPMC 2008)*, pp. 245-257, September 10-12, 2008. Bath, U K.

[5] Yong, C. and Barth, E. J. (2011) “A Virtual-Cam Control Methodology for Free-Piston Engines*”. 2011 ASME Dynamic Systems and Control Conference & Bath/ASME Symposium on Fluid Power and Motion Control.* DSCC2011-5988, pp. 1-8, Oct 31- Nov 2, 2011, Arlington, VA.

[6] Barth, E. J. and Riofrio, J. (2004) “Dynamic Characteristics of a Free Piston Compressor”. *2004 ASME International Mechanical Engineering Congress and Exposition (IMECE)*, IMECE2004-59594, November 13-19, 2004, Anaheim, CA.

[7] Riofrio, J. and Barth, E. J. (2005) “Design of a Free Piston Pneumatic Compressor as a Mobile Robot Power Supply,” *Proceedings of the 2005 IEEE International Conference on Robotics and Automation (ICRA)*, pp. 236-241, Barcelona, Spain, April 2005.

[8] Riofrio, J. and Barth, E. J. (2005) “Experimental Operation and Characterization of a Free Piston Compressor,” *2005 ASME International Mechanical Engineering Congress and Exposition (IMECE)*, IMECE2005-81743, November 5-9, 2005, Orlando, Fl.

[9] Riofrio, J. A. and Barth, E. J. (2007) “Design and Analysis of a Resonating Free Liquid-Piston Engine Compressor,” *2007 ASME International Mechanical Engineering Congress and Exposition (IMECE)*, IMECE2007-42369, November 11-15, 2007, Seattle, WA.

[10] Riofrio, J. A. and Barth, E. J. (2008) “Experimental Assessment of a Free Elastic-Piston Engine Compressor with Separated Combustion Chamber,” *Bath/ASME Symposium on Fluid Power and Motion Control (FPMC 2008)*, pp. 233-244, September 10-12, 2008. Bath, U K.

[11] Willhite, J. A. and Barth, E. J. (2009) “Reducing Piston Mass in a Free Piston Engine Compressor by Exploiting the Inertance of a Liquid Piston”. *2009 ASME Dynamic Systems and Control Conference & Bath/ASME Symposium on Fluid Power and Motion Control.* DSCC2009-2730, pp. 1-6, October 12-14, 2009, Hollywood, CA.

[12] Yong, C. and Barth, E. J. (2009) “Modeling and Control of a High Pressure Combined Air/Fuel Injection System*”. 2009 ASME Dynamic Systems and Control Conference & Bath/ASME Symposium on Fluid Power and Motion Control.* DSCC2009-2769, pp. 1-8, October 12-14, 2009, Hollywood, CA.

[13] Willhite, J. A. and Barth, E. J. (2010) “Optimization of Liquid Piston Dynamics for Efficiency and Power Density in a Free Liquid Piston Engine Compressor,” *Bath/ASME Symposium on Fluid Power and Motion Control (FPMC 2010)*, pp. 461-473, September 15-17, 2010. Bath, U K.

[14] Yong, C. (2011) “A Virtual-Cam Based Control Methodology for Free-Piston Engines,” Ph.D. Dissertation, Vanderbilt University.

[15] Willhite, J. A., Yong, C., and Barth, E. J. (2012) “The high inertance free piston engine compressor part 1: dynamic modeling,” *ASME Journal of Dynamic Systems, Measurement and Control*, in revision 2012.

[16] Willhite, J. A. , Yong, C., and Barth, E. J. (2012) “The high inertance free piston engine compressor part 2: design and experimental evaluation,” *ASME Journal of Dynamic Systems, Measurement and Control*, in revision 2012.

[17] Hofacker, M. E.; Kumar, N.; and Barth, E. J. (2013) “Design and Validation of a Figure-Eight Free-Liquid-Piston Engine Compressor for Compact Robot Power,” *ASME/IEEE Transactions on Mechatronics*, In preparation.

5. An Experimentally Validated Figure-Eight Free-Liquid Piston Engine Compressor

Mark E. Hofacker, Nithin S. Kumar, and Eric J. Barth

Vanderbilt University

Nashville, TN

Status: To Be Submitted to *IEEE/ASME Transactions on Mechatronics*

January 2014

Prologue

This manuscript presents a more detailed description of the third-generation free piston engine compressor discussed in Chapter 4. Similar to Chapter 4, this work primarily considers the energetic source and the source impedance. Additionally, however, this work also describes the steps taken to improve the load impedance to increase the engine compressor's output pressure. The impedance view of this project becomes clear when the free piston engine compressor's dynamics are shown as a buck converter which shares many of its conceptual goals.

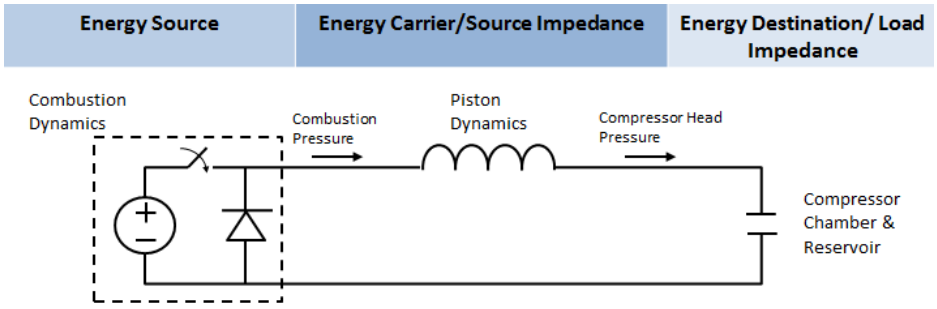

Figure 5.i – Electrical circuit approximation of the free-piston engine compressor as a buck converter

The primary energy domains addressed in this project include chemical, thermal, hydraulic, and pneumatic. The main source of power in this project was the chemical potential of the air/fuel mixture. Through the combustion process, the chemical potential is converted to heat and pneumatic potential, which in turn propels the liquid piston. This liquid piston then forces air from the compressor head and into the high pressure reservoir. The source impedance therefore includes the hydraulic and pneumatic domain in the form of the liquid piston and the compressor

head's pump chamber. The goal of this process is to deliver energy to the pneumatic domain and raise the pressure of the reservoir. The load impedance is therefore comprised of the high pressure reservoir and the flow restriction of the check valve between the compressor head's pump chamber and this reservoir.

This check valve and the combustion conditions were the primary barriers to efficient transfer. Both of these barriers were partially addressed by the utilization of a high inertia liquid piston. The inertia of the piston presents a high dynamic load such that compression is maintained until injection has finished and the spark can ignite the mixture.

The slower dynamics due to the use of the liquid piston places less demands on the check valve. By slowing the dynamics, the valve has more time to open and close and does not need to accommodate as high of a flow rate. Even with the slower dynamics enabled by the high inertance piston, this check valve was identified as a major limiting factor for the maximum pressure output of the previous, second generation free piston engine compressor. With the third prototype, steps were therefore taken to improve the match between the check valve and the dynamics of the combustion and the liquid piston by formulating a new time-to-saturate metric. As a result of these changes, the device was capable of producing compressed air at higher pressures than its previous iterations.

The free piston engine compressor described in this document is a continuation of work done by Willhite, Yong, and Riofrio [1i-3i] in creating an internal combustion, single cylinder, free piston engine compressor. New developments in the current prototype include a self-balancing figure-8 configuration, a high efficiency compressor head, and on board control and electronics. Although the need for a high inertance piston was recognized during the design of previous generations, the buck converter analogy showed the conceptual necessity of this inertia.

Other modern untethered pneumatic power supplies include a miniature free-piston two-stroke homogeneous charge compression ignition (HCCI) engine constructed by Tian et al., [4i] and a Stirling thermocompressor discussed later in this document. Tian's work with the HCCI engine focused on modification of the energy source and carrier impedance by optimizing the operational frequency and the natural frequency of the sprung piston.

The third generation engine compressor has advantages over the previous generations and alternative solutions as a power source for the compact rescue crawler robot. The device's high pressure output is well suited to the crawler's pneumatic actuators, its low weight makes it easy to carry, it is self-contained and only requires 12V DC power, which can be provided by the crawler's battery, and finally the device's low amounts of vibration make it well suited to be mounted on a mobile platform such as the rescue crawler or other similar untethered robot.

Alternatively, the electric motor paired to an air compressor could be utilized as a pneumatic power source for the rescue crawler robot. This approach was not pursued due to the lower energy density of batteries as compared to a hydrocarbon fuel source.

Abstract

This paper presents the design and control of a free-piston engine compressor. Internal combustion with a propane-air mixture in the engine combustion chamber is used to displace a liquid piston and efficiently compress air. This results in low temperature, high-pressure air for use as a high energy density power supply for untethered, compact robots. Traditional intake and compression strokes of a four-stroke engine are avoided by injecting compressed air and propane and by exploiting the dynamic loading of a high inertance, low mass liquid piston. Self-balancing of the single cylinder is achieved through the use of a liquid piston in a figure-8 configuration. The benefits of this configuration are demonstrated using simulated data and the Reynolds transport theorem. A closed loop controller is utilized to make intelligent decisions regarding the timing of air and fuel injection, the spark plug and the exhaust valve. The pumping pressure of the device is increased through improvement to the nozzles and to the pump chamber's outlet check valve. Experimental results are presented that demonstrate an increased pumping pressure over previous versions of this device.

I. Introduction

Current power sources for human scale robots (10-100 W) primarily use batteries and are actuated by DC motors. The advantages of the relative ease of DC servo motor control and low cost of lithium ion (Li-ion) and nickel-metal hydride (NiMH) batteries are outweighed by their limited useful mechanical work output before running out of charge, operating time duration, and the bulkiness of electromagnetic actuators for certain applications, leading to low energy and power densities [1]. The proposed propane-powered FLPEC has the potential to be energy dense, compact, and practical for use in tethered human scale robots.

Free piston engines (FPEs) are a class of linear engines, (as opposed to rotating crankshaft engines) wherein piston motion is dictated by the interaction of load forces and the forces of combustion gases. R. P. Pescara is credited with the development of the original free-piston engine with a patent detailing a single piston spark ignited air compressor in 1928 [2]. Pescara worked on spark ignited and diesel combustion prototypes and eventually constructed the free-piston air compressor and the multi-stage free-piston air compressor engine in 1941 [3]. The German company, Junkers, successfully developed their own free-piston air compressor, which was used in the German navy to launch torpedoes in 1936 [4]. The Societe Industrielle Generale de Mecanique Appliquee (SIGMA) in France developed an opposed free-piston, diesel powered gas generator, the GS-34 in 1944, which had a power output of 1000 kW at 613 rpm and was successfully used in 21 minesweepers of the French Navy [5-6]. General Motors (GM) developed the Hyprex engine in 1957, a diesel free-piston engine with a power output of 185 kW at 2400 rpm [7-8] and installed it in an automobile, the XP-500 (the world's first free-piston engine powered car), which unfortunately could not compete with contemporary engines, halting further

research into the field. The GTS William Patterson, a US Maritime Administration vessel, had an onboard marine power plant using six GM-14 (free-piston gas generators developed by GM based on the GS-34), which operated in the late 1950's with disappointing results [9]. Ford developed models for the design of a free-piston gas generator with a power output of 150 hp (112 kW) at 2400 rpm and constructed the Ford model 519 free-piston power plant [10]. This was implemented in a farm tractor and Ford reported the engine was more compact and lightweight than contemporary diesel engines, with higher torque values at lower speeds [11].

Recently, free-piston engines have been used in hydraulic systems and in free-piston engine generators. Innas BV, a Dutch company, has developed a diesel powered single piston, hydraulic free-piston engine for use in off-highway vehicles and forklifts. The CHIRON Free-Piston engine has a power output of 17 kW at 50% efficiency and is reported to consume 20% less fuel than conventional engine-pump units [12]. Researchers at Tampere University, Finland have designed and validated a dual piston hydraulic FPE prototype operating at 20% efficiency with combustion pressures up to 88 bar [13-14]. Furthermore, Clark et al. [15-19] at West Virginia University have developed a spark ignited dual piston engine with a prototype outputting 316 W at 23.1 Hz. Van Blarigan et al. [20] at Sandia National Laboratories have designed a homogeneous charge compression ignition (HCCI) dual piston free-piston engine generator with a power output of 40 kW.

Some industries have taken advantage of the reduced emissions, less complex design, and lower fuel consumption of free piston engines in their products. Pempek Systems, based in Australia have developed a Free Piston Power Pack (FP3) for use as an electric generator in hybrid electric cars, with a peak power output of 100 kW and maximum operating frequency of 30 Hz [21]. Sunpower, Inc. currently manufactures free-piston Stirling engines, with a variety of models such as the EE-35, with an output of 42 W at 32% efficiency, weighing 1.4 kg and the EG-1000, with an output of 1 kW at 32% efficiency, weighing 35 kg [22].

Regarding free piston engines in general, none of the previous works investigated directly coupling an air compressor with the engine. There were early designs of free piston engine compressors. Apart from these examples, there are no other notable attempts at a free piston engine compressor. It is worth revisiting these early attempts within the context of modern control electronics and advances in system modeling and model-based design.

The proposed internal combustion, single cylinder, free-piston engine compressor is designed to efficiently produce low temperature, high-pressure air (650-1100kPa), a dry weight of 1.5 kg, and an energy density exceeding 1500 kJ/kg. It requires a relatively small footprint [23] so that it can be mounted on a compact rescue robot.

Similar devices include iRobot's Small Unmanned Ground Vehicle (SUGV), Qinetiq's Dragon Runner, ICOR Technology's MK3-Caliber, and Boston Dynamics's BigDog. iRobot's 310 SUGV is a 13.2 kg reconnaissance, bomb disposal, and explosives detection robot and is powered by 2

military-grade BB-2557/U batteries (Li-ion, 28.8 V, 4.4 Ah at 12 V, 540 g) [24], which provides it with an operating time of 1.5 hrs [25]. A 100 Qinetiq Dragon Runner SUGVs are in operation in Afghanistan by the British army to detect roadside bombs [26]. These robots weigh 6.4 kg and are powered by a BB-2590/U battery (lithium ion battery, 33 V, 14.4 Ah at 15 V, 1.4 kg) [27], providing an operating time of 4-6 hours [28]. ICOR Technology's MK3-Caliber is a versatile surveillance robot with towing and dragging capabilities weighing 84 kg. It is powered by a 24 V DC, lead-acid battery providing an operating time of 3-5 hours [29]. Boston Dynamics's BigDog is a rough-terrain four-legged robot capable of walking, running, and climbing. The power supply for BigDog is a two-stroke internal combustion engine 11.2 kW (15 hp), which drives a hydraulic pump with an operation time up to 2.5 hours [30]. Hydraulic actuation is an effective power supply source for BigDog, which weighs 109 kg, but scaling down this power source is difficult since such systems require several components such as accumulators, reservoirs, control valves, hosing, and return lines.

Current state-of-the-art, battery powered, motor actuated, robots include the Honda Asimo, TOSY TOPIO 3.0, and Aldebaran Robotics Nao. The Honda Asimo is equipped with a 6 kg, 51.8 V Li-ion battery providing 1 hour of operating time and takes 3 hours to fully recharge. The ASIMO is actuated by DC servomotors, harmonic speed reducers, and drive units [31]. The current TOSY Ping Pong Playing Robot (TOPIO 3.0) is the third generation robot developed by the Vietnamese robotics firm, TOSY. It stands 1.88 m tall, weighs 120 kg, is powered by a 48 V, 20 Ah Li-ion polymer battery, and is actuated by brushless DC servomotors [32]. The Nao is a 4.5 kg mini-humanoid robot, actuated by brush DC motors and powered by a 21.6 V, 1.28 Ah Li-ion battery, which sustains it for 1.5 hours and takes 2 hours to recharge [33].

Pneumatic power is a favorable option for smaller scale applications due to the low weight of actuators and the ability to expel exhaust gases to the environment (eliminating the need for return lines). Since compressed air has a low energy density, it would be more practical to integrate an onboard compressor to serve as a power source for dog-sized robots. The proposed FLPEC uses propane for internal combustion due to its higher energy density relative to monopropellants (currently powering the CRR), and high vapor pressure, eliminating the need for a fuel pump. Aichlmayr reports a smaller-scale, compact engine compressor, which requires idle cycles that wastes fuel during periods of inactivity [34], which is eliminated in the proposed device.

The proposed engine compressor is designed, constructed, and controlled. Improvements over previous iterations of the device with regard to the compressor head, check valve, controller, and piston configuration are discussed in detail. Real time control is used to account for cycle-to-cycle variations and experimental results are presented. A picture of the device is shown in Fig. 5.1.

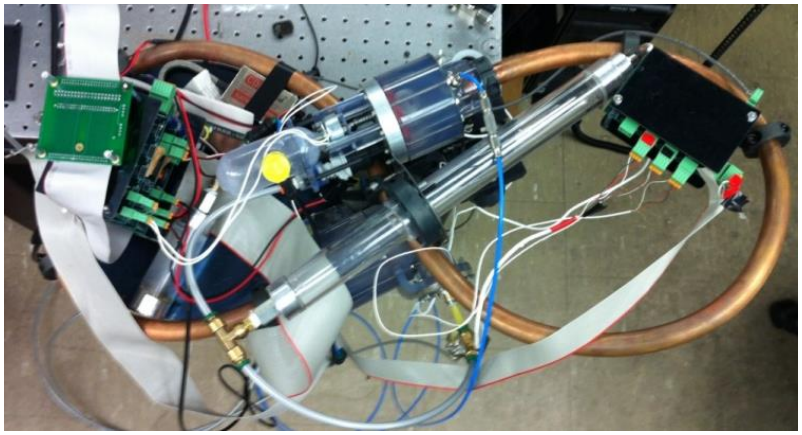

Figure 5.1 - Picture of Free Piston Compressor Engine with figure-8 high inertance liquid piston and onboard electronics and control.

The proposed FLPEC is a continuation of the work done by Riofrio [1], Willhite [35], and Yong [36]. Improvements and developments to earlier designs are presented including a figure-eight liquid piston configuration, a highly efficient compressor head, onboard control and electronics, and a real-time controller.

II. Experimental Setup

The FLPEC operates on an “inject and fire” cycle wherein intake, compression, and expansion are combined into one stroke, while the second stroke is used only for exhausting the working fluid. This is achieved through the use of compressed air, compressed propane, and a liquid piston consisting of water trapped between two elastic membranes. Fig 5.2 shows the engine-compressor with the liquid piston at top dead center (TDC).

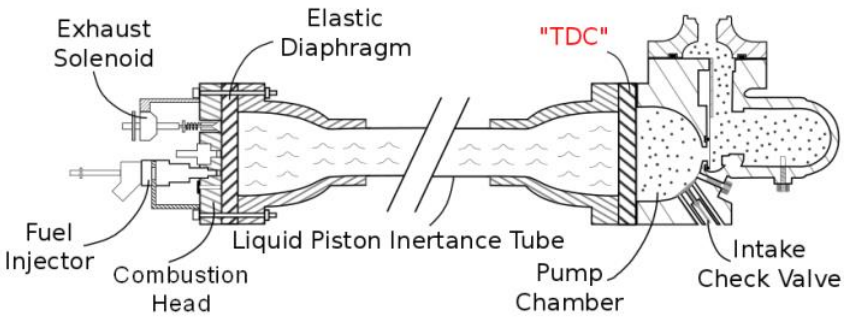

Figure 5.2 - Schematic [37] of free piston engine compressor at effective top dead center showing relaxed elastomers, a small combustion chamber, and a pump chamber with atmospheric air

The combustion chamber is the volume bounded by the aluminum combustion head and the elastic membrane. Compression is dynamically maintained during injection because the inertia of the piston prevents the piston from moving too quickly when the combustion chamber is pressurized. Following injection, a spark plug ignites the propane-air mixture and the forces of

combustion gases move the piston. Fig. 5.3 shows the engine-compressor at bottom dead center (BDC).

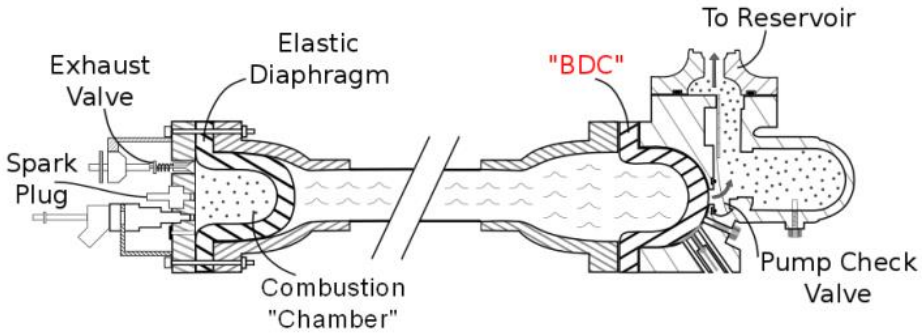

Figure 5.3 - Schematic [37] of free piston engine compressor at effective Bottom Dead Center with elastomers fully stretched, a fully expanded combustion chamber, and an emptied pump chamber

As the piston moves from top dead center to bottom dead center, air is forced from pump chamber and into the reservoir. When pumping is complete, a check valve inside the compressor head closes to prevent backflow into the reservoir. The operation of the compressor head is shown in Fig. 5.4.

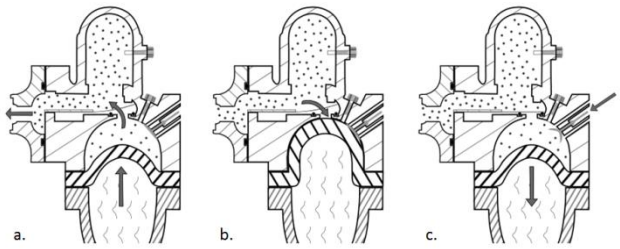

Figure 5.4 - (a) Compressor head while pumping (b) Compressor head at BDC (c) Compressor head during breathe-in [37]

After the combustion products are completely expanded and pumping is completed, the second stroke is initiated by opening an exhaust valve on the combustion head. This allows the elastomers to relax, expelling the exhaust products through the exhaust valve and breathing air into the pump chamber through the intake check valve. The exhaust valve closes when the piston reaches top dead center position so that the next cycle can begin.

III. Piston Inertia Considerations

Increasing the amount of piston inertia was vital to the efficient transer of power from the combustion chamber to the air reservoir. The intertia that the piston presents to the combustion process is conceptually similar to the role that the inductor plays in a buck converter. This relation is demonstrated below in Fig. 5.5.

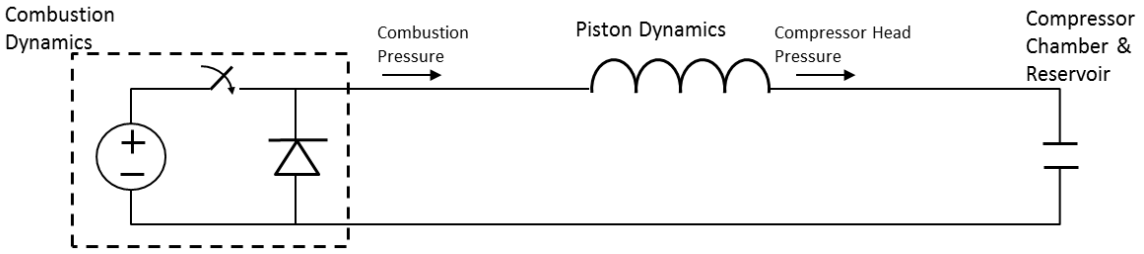

Figure 5.5 - Schematic of the free-piston engine compressor represented as circuit diagram of a buck converter.

In a buck converter, a high voltage/low current source is converted to a low voltage/high current across a load such as a capacitor at a high efficiency. In the free-piston engine compressor, more mass leaves the compressor head than enters the combustion head. The admitted air and fuel, when combusted, present a high pressure akin to the source voltage of the buck converter. This source then loads the high inertance piston and builds kinetic energy similar to the manner in which a buck converter temporarily loads the inductor before the switch opens. The kinetic energy stored in the piston is used to deliver large amounts of air to the high pressure reservoir. In a similar manner, the energy stored in the inductor is used to draw current from ground and deliver more charge, and hence a higher average current, to the load than was drawn from the voltage source.

Willhite [35] describes the operation of a similar engine compressor (1) and models the volume rate of change of the combustion chamber, Q, as a function of the difference of combustion pressure and compressor chamber pressure ΔP.

$$\Delta P = I\dot{Q} + A_C Q^2 + RQ + K(V_C - V_0)^{2.344} \tag{1}$$

In (1), K is nonlinear stiffness coefficient of the diaphragms, (V_c-V_0) is the swept volume of the combustion chamber, A_c is a geometry dependent coefficient, R is viscous losses coefficient, and I is the piston inertia. In other previous work on these free-piston engine compressors [1, 34, 35] the nonlinear character of the stiffness varied in form somewhat depending on the diaphragms used. Regardless of the exact nonlinear behavior, by linearizing equation (2), the engine compressor's dynamics can be expressed as (3).

$$\Delta P = I\dot{Q} + RQ + K\int Q \tag{2}$$

These dynamics are analogous to the dynamics of the buck converter (4) transferring energy to a capacitive load:

$$\Delta V = L\dot{I} + RI + \frac{1}{C}\int I \tag{3}$$

In both instances, the inertance temporarily carries energy from the source before it is delivered to the load.

The inertance also benefits the engine-compressor by helping maintain compression during injections. This could also have been addressed by increasing elastomer stiffness, but this leads to losses because the energy delivered to the elastomers cannot be recovered for compression of air to the reservoir.

It has been shown that piston inertia could be increased while reducing piston mass through the use of a variable cross sectional area liquid piston [38]. A schematic of this concept is shown in Fig. 5.6.

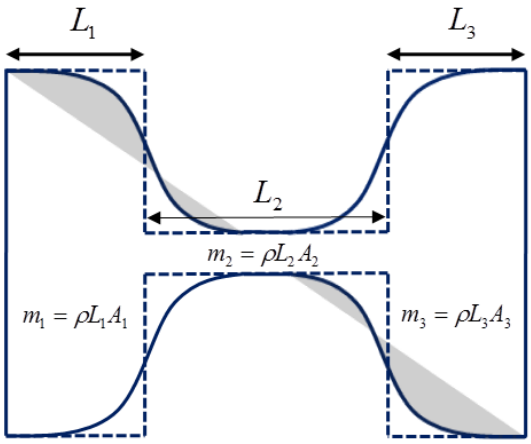

Figure 5.6 - Schematic [38] of liquid piston with converging and diverging nozzles and diaphragms on both ends

In this work [38], it was demonstrated that the inertia contained in such a liquid piston could be described by (4).

$$I = \left[\frac{\rho L_1}{A_1} + \frac{\rho L_2}{A_2} + \frac{\rho L_3}{A_3} \right] \tag{4}$$

For this scale of engine, the needed inertia was determined through simulation to be approximately 6.4 kg/mm^3 in order to achieve a reasonable balance between compression and weight. This inertia is achieved using 0.63 kg of water contained within a tube 1.524 long and 1.9 cm in diameter with nozzles on either end that expand from a diameter of 1.9 cm to 5.1 cm over a length of 7.62 cm. For comparison, if a straight pipe were used with the current initial piston surface area, the piston would need to be 10.9 meters long and weigh 21.7 kg. Alternatively, it would be impractical to simply use a small pipe with no reduction because there needs to be space for the injectors, spark plug, etc. on the combustion head.

IV. Self-Balancing Figure-Eight Liquid Piston

While imbalance is often an unavoidable problem for single cylinder engines, the unique properties of the liquid piston provided a mechanism for reducing engine vibration. By routing the liquid piston in various geometries, the inertia of the piston's movement can be made to mostly negate itself. The reduced vibration means that the engine can be mounted with less external bracing than is typically necessary for single-cylinder engines. This is especially important on a mobile platform such as the rescue crawler because strong shocks from the engine could cause the crawler to fall. The three configurations shown in Fig. 5.7 are the ones used by Riofrio [1], Willhite [35], and the figure-8 configuration described in this paper.

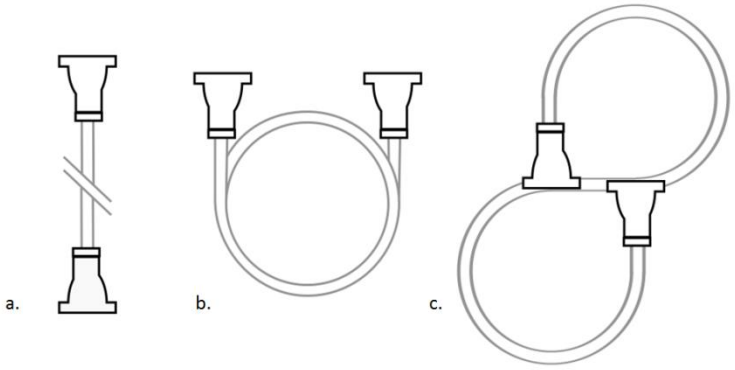

Figure 5.7 - a) Straight Configuration b) Loop Configuration c) Figure-8 Configuration

To reduce vibration, the liquid piston is redirected back on itself to minimize the net force. This canceling effect is a consequence of Newton's second law. Since the water inside the piston is incompressible, if the inlet and outlet are placed at the same point, the force on the external bracing is minimized and is applied on the pipe itself. The force on the external bracing increases as the inlet and outlet are positioned further away from each other. To minimize the magnitude of this force in the figure-8 design, the combustion and compressor head were positioned as close together as possible. A consequence of reducing the distance between the two heads is the necessity of bending the pipe as shown in Fig. 5.7b, which causes a net moment in the tube. However, in the figure-8 design, the torque caused by the water in the upper curve of the tube (see Fig. 5.7c) is cancelled by the corresponding negative torque of the same magnitude in the lower curve.

To calculate the moment and force in each of the three configurations, the Reynolds transport theorem (5) was used.

$$\frac{DB_{sys}}{Dt} = \frac{\delta}{\delta t}\int_{CV} \rho b d\forall + \int_{CS} \rho b(\vec{V}\cdot\hat{n})dA \tag{5}$$

It was assumed that the water inside the pipe was inviscid and incompressible and the engine was not accelerating. The volume is defined as $\forall$, the density as ρ, and *b* is the extensive form of the intensive property B. Substituting the velocity of the liquid, $\vec{V}$, for *b*, the $\frac{DB_{sys}}{Dt}$ term becomes the net external force acting on the control volume:

$$\sum F_{\substack{contents of the \\ control volume}} = \frac{\delta}{\delta t}\int_{CV}\vec{V}\rho d\forall + \int_{CS}\vec{V}\rho(\vec{V}\cdot\hat{n})dA \tag{6}$$

Further assumptions include constant cross-sectional area and constant pipe length. Applying these assumptions yield:

$$\sum F_{\substack{contents\ of\ the \\ control\ volume}} = \rho(\Delta\vec{x}\ddot{\forall} + A\vec{V}_{out}(\vec{V}_{out}\cdot\hat{n}_{out}) + A\vec{V}_{in}(\vec{V}_{in}\cdot\hat{n}_{in})) \tag{7}$$

The *A* is the cross-sectional area of the pipe, the $\hat{n}$ terms are unit vectors normal to the control surface at the inlet and outlet, and Δx is the distance between the inlet and outlet. The cross product of force (7) and the radius from the center of mass $\vec{r}$ is the moment exerted by the liquid on the support (8).

$$\sum(\vec{r}\times F)_{\substack{contents of the \\ control volume}} = \frac{\delta}{\delta t}\int_{CV}(\vec{r}\times\vec{V})\rho d\forall + \int_{CS}(\vec{r}\times\vec{V})\rho(\vec{V}\cdot\hat{n})dA \tag{8}$$

The figure-8 design, depicted in Fig. 5.7c, was selected to minimize the forces in (7) and moment from (8). To minimize the force it is necessary to minimize the distance between the inlet and the outlet.

To find the forces and moments exerted on the external bracing of the three designs, the model from Willhite [35] was used to find the volumetric velocities and acceleration inside of the piston. Simulated data was used because it was not possible to directly measure the flow of the water inside the piston. Using this data, Figure 5.8 below was created using (7).

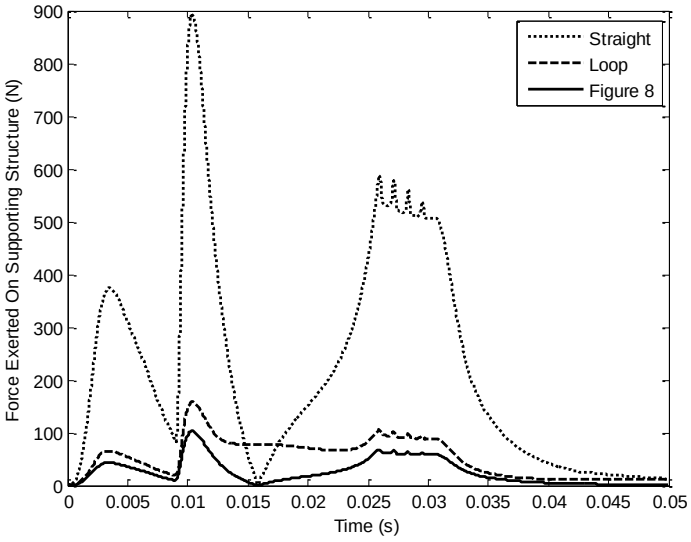

Figure 5.8 - Force exerted on engine support due to fluid motion during combustion and piston expansion

In the model, the amount of injected air and fuel was adjusted in the model until the liquid piston fully expands with a velocity close to zero. This represents ideal operating conditions where no fuel is being wasted on collisions with the compressor head.

The linear impulse, moment, and angular impulse were also calculated using (7) and (8) respectively and the same simulated data used to create Figure 5.8. The acceleration of the liquid changes signs mid-cycle, at about 0.015 seconds, so the impulses were calculated by integrating only over this initial period of time. The maximum values of the force, impulse, moment, and angular impulse during an engine cycle are shown below in Table 5.1.

Table 5.1 - External Effects for Various Liquid Piston Configurations

	Straight	**Loop**	**Figure-8**
Maximum Force (N)	894	159	103
Maximum Moment (Nm)	0	116	0
Maximum Impulse (Ns)	4.61	1.02	0.533
Maximum Angular Impulse (Nm-s)	0	0.567	0

The use of figure-8 configuration significantly decreased the force and impulse applied on the support, without generating a large moment and angular impulse and is therefore a good configuration to use aboard a mobile platform, such as the compact rescue robot.

V. Check Valve

A major limiting factor for the maximum pressure output of the previous free piston engine compressor by Willhite [35] and Yong [36] was the check valve in the compressor head that allows air to be compressed into the reservoir. This check valve, shown in Figure 5.9a, consisted of a metal cylinder that was pressed against an o-ring by a coil spring. The valve imposed a restriction upon the air entering the reservoir, was not sensitive to pressure changes due to pre-compression in the spring, and allowed backflow from the reservoir due to not closing quickly enough after pressure inside of the compressor head had dropped. This valve was replaced by the valve shown in Figure 5.9b to address these problems.

To design the check valve, it was modeled as a spring-mass-damper that responds to pressure differences between the compression head and reservoir. The displacement of the valve is considered proportional to the valve area up to a certain point where the effective valve area saturates and any further opening will not reduce the flow restriction. A metric was thus developed to guide the necessary factors in creating an optimal check valve, to minimize the time taken to reach saturation for a given differential pressure.

$$t_{saturate} \propto \frac{1}{\omega_n}\left(\frac{a_{saturate}}{1/k}\right) = a_{saturate}\sqrt{mk} \tag{9}$$

This was derived by considering a unit step response of a critically damped second order system, leading to a time constant of the reciprocal of the natural frequency (ω_n). The steady state value of a unit step response of a simple mass-spring-damper system is the reciprocal of the stiffness. The stiffness is that of the valve (*k*). It is assumed that the effective valve area is proportional to the displacement of the types of valves shown in Figure 5.9. For an infinitely thin plate with a hole of radius *r* covered by a plate at a height *h* above the hole, the flow area is dictated by a cylinder wall surface area ($2\pi rh$) while this is less than the area of the opening (πr^2). In a real valve opening covered by a poppet or reed valve, this will not be exactly the case since the discharge coefficient will also vary, but the proportionality between the effective flow area and the valve displacement still holds.

For a given displacement it can be assumed that the time to reach that displacement is inversely proportional to the natural frequency of the system. Therefore, the time ($t_{saturate}$) to reach saturation ($a_{saturate}$) is proportional to the product of the time constant $1/\omega_n$ and the fraction of the steady-state displacement $\frac{a_{saturate}}{1/k}$. With this metric, it becomes clear that it is desirable to minimize the valve mass (*m*) and the stiffness. These two design goals were achieved by combining the sealing surface and spring element into a single compliant mechanism. To achieve

low mass, the check valve was constructed using a thin piece of sheet metal. Stiffness was reduced by making the compliant part of the valve a thin, long cantilevered beam. A stop was incorporated in the design to stop the valve from exceeding saturation so that the time taken to close the valve was reduced.

The previous check valve of Figure 5.9a had a mass of 18.4 grams, a spring constant of 583000 N/m, and a natural frequency of 895.87 Hz. By using the cantilevered beam equation, the stiffness of the new valve shown in Figure 5.9b was calculated to be 4140 N/m, with an effective mass of 0.5 grams, leading to a natural frequency of 537 Hz. Though the new design has a lower natural frequency, the metric indicates that the new check valve takes two orders of magnitude less time to open. The model developed by Willhite [38] predicts that the maximum pumping pressure of this engine should increase from 552 kPa (80 psi) to 2170 kPa (315 psi) due to the implementation of the new check valve.

Figure 5.9 - (a) Previous Compressor Head Check Valve (b) Current Compressor Head Check Valve

The intricate geometries required to incorporate this check flap prompted the construction of the compressor head using stereolithography (SLA) shown in Figure 5.10. To minimize the possibility of fracture in the event of a collision with the piston, a tough, impact resistant, ABS-like material called Somos NeXt was used. The utilization of the SLA material for the compressor head also contributed to reduced weight over the previous device [39] (270g vs. 505g) due to its lower density. A silicon rubber umbrella-type check valve replaced the old breath-in valve for breathing in atmospheric air during the return stroke. The advantages of this valve include being soft enough to allow mass flow at low-pressure differences (to ensure there is not a significant partial vacuum during breath-in) and not damaging the piston membrane during collision when combustion occurs (since the valve is all rubber versus the previous design that used a small screw to secure the valve). Furthermore, it is vital to minimize flow restrictions immediately after the check valve opens (due to the large increase in mass flow rate), and so an intermediate reservoir was incorporated directly into the compressor head, to ensure that the freshly pumped air was not restricted by the tubing connecting the compressor head to the reservoir. In order for

real-time control from pressure variations, small pressure sensors were mounted into the reservoir and the compressor head.

Figure 5.10 - Picture of Compressor Head

VI. Onboard Components

The previous engine compressor required many external components for operation, which compromised its ability to serve as a practical power source for the rescue crawler. Improvements in functionality have been addressed in this design of the free piston engine compressor with the addition of key on-board components while minimizing electrical power consumption and weight.

A Diamond Systems Athena single board computer (shown in Fig. 5.11b) with onboard data acquisition was mounted on the compressor for monitoring pressure, executing the controller, and providing output signals to the injectors, the exhaust solenoid, propane buffer valve, and spark plug. The controller for the previous compressor had a sampling rate of 10 kHz, but due to the lower power microprocessor, the sampling rate was reduced to 1 kHz.

All the electronics used for signal conditioning and voltage regulation were mounted on printed circuit boards as shown in Fig. 5.11a. The electronics were designed to only need the 12 V power provided by the compact rescue crawler robot. Energy efficient switching DC/DC regulators were used to supply the electronics with ±12 V and 5 V. The specific components used for the voltage regulation are the Murata SKA1212SC and the LM2576T-005G.

Figure 5.11 - a) On Board Electronics b) Athena Single Board Microprocessor

Kulite miniaturized XTL-190 and XTYL-140 pressure transducers were used to measure the pressures in the compressor head, propane buffer tank, and reservoir. The signals were amplified using instrumentation amplifiers and filtered digitally inside the controller. The exhaust valve, manufactured by O.S. Engine is traditionally meant for use in remote control airplanes. It is motivated by a Ledex 124911-028 solenoid (shown in Fig. 5.12b), which is powered by an AMC servoamp model AZ20A8. The spark plug is powered using a RCEXL ignition box, which provides high voltage and allows precise control of the spark. The spark plug used is an NGK ME8 and the ignition box is a RCEXL Model A-01. Two Bosch fuel injectors (Part # 0280150842) are used for independent air and fuel injection. To increase the speed of response of the fuel injector and decrease power consumption, an injector drive controller from Texas Instruments (LM1949) was used. The injectors have no fittings for connecting and instead rely on an external manifold. To save weight and increase compactness, this manifold was integrated with an actively regulated propane buffer tank shown in Fig. 5.12a.

Propane regulation was necessary because the long sampling period and the relatively large fuel injectors made it impractical to accurately inject fuel at the propane's vapor pressure. By actively regulating using a solenoid valve, it is possible for the controller to change the injection pressure. The buffer tank was constructed out of Accura 60 material using an SLA process. This material has a low density that allows the tank to be lightweight while containing complex geometric features. The complex geometry accommodates compact valving and reduced the number of pneumatic fittings needed.

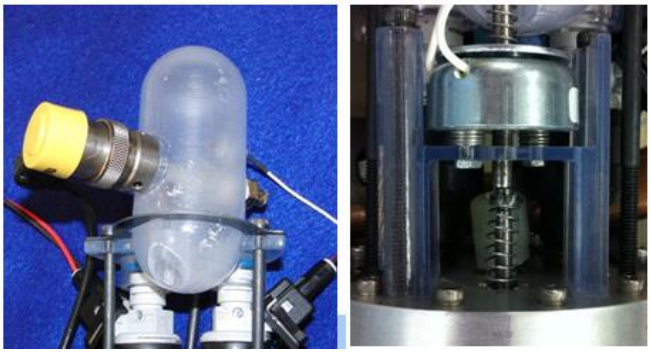

Figure 5.12 - a) Injector Manifold with Integrated Actively Regulated Propane Buffer Tank b) Exhaust Solenoid

VII. Controller

A controller was created using Stateflow to control the injectors, exhaust valve, buffer tank valve, and the spark plug. To prepare the engine-compressor for operation, the propane buffer tank was allowed to fill to the appropriate pressure. To ensure consistent injections, this buffer tank valve was closed while the propane was being injected into the combustion chamber. An external air source was used to fill the air reservoir and was then disconnected for the duration of operation.

Many of the controller's decisions were determined by estimating the position and velocity of the liquid piston. The position and velocity of the piston were estimated using the pressure inside the compressor head. The pressure is approximately proportional to the displacement of the liquid piston via the ideal gas law while no pumping is occurring.

The injection duration for the air and propane were adjusted for different trail runs but did not vary across cycles. As shown in Figure 5.13, the propane injection command is followed by the air injection command, after which the spark plug coil begins to charge for 18 ms. When the coil is subsequently disconnected, the inductor discharges to create the spark.

After the spark, the controller monitors the compressor head and checks if the pressure rises above 50 psig for a certain duration of time after the spark ignites. A combustion event will impart an impulse on the piston which will cause it to accelerate quickly towards the compressor head. Therefore, if a rapid rise in pressure is not detected, the controller deems the cycle a misfire and opens the exhaust for a predetermined amount of time to end the cycle.

If the combustion pressure is high enough, air will be pumped into the reservoir. It can be determined that pumping has occurred for a given cycle if the compressor head pressure rises above the reservoir pressure.

The controller attempts to open the exhaust valve immediately after pumping finishes, which occurs when the piston has reached its maximum displacement for that cycle. To accomplish this, the controller waits until the pressure in the compressor head has peaked and then commands the exhaust valve to open. This pressure peak and corresponding valve opening can be seen in

Fig. 5.13 which shows the pressure in the compressor head overlaid with the timings of the air, fuel, spark, and exhaust in a typical combustion cycle.

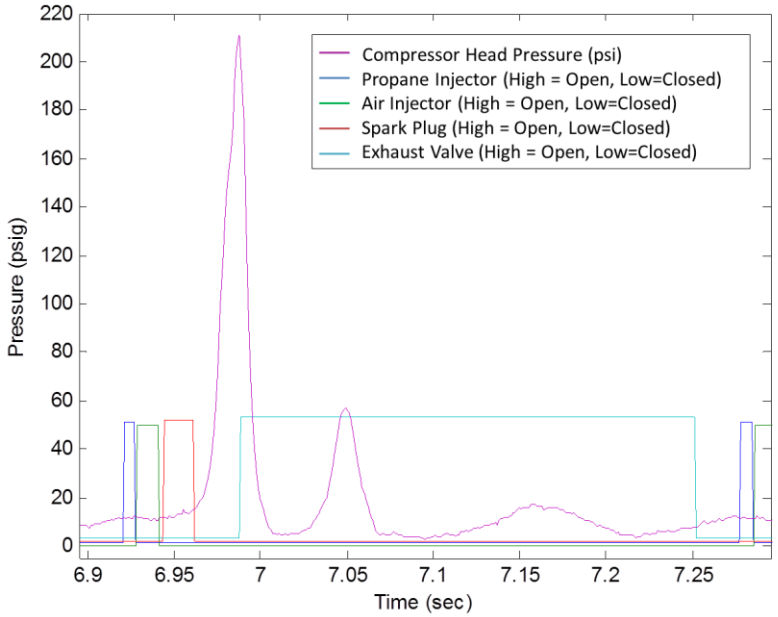

Figure. 5.13 - Reservoir pressure and command signals for a single combustion and exhaust event

As the combustion gasses are expelled from the combustion head, the elastic membranes retract. The “breathe-in” of fresh air into the pump chamber can be seen during periods of low pressure following combustion as the piston returns. The effectiveness of the breathe-in check valve can also be observed. Ideally the pressure inside of the compressor should drop to atmospheric pressure during breathe-in.

Due to the high inertance of the liquid piston and low damping, the membrane overshoots its relaxed position, collides with the combustion head, and bounces back. If the exhaust valve is left open, the piston oscillates 5 to 6 times before coming to rest. It was determined that consistent combustion was sensitive to the timings of the exhaust valve. Closing the exhaust valve largely stops piston motion and therefore determines the initial size of the combustion chamber, which will affect the compression ratio of the next cycle. Experimentally it was determined that consistent combustion occurred when closing the exhaust valve after the piston’s third collision with the combustion head. Essentially the exhaust valve is ideally responsible for “catching” the piston when the volume in the combustion chamber is at a minimum. When trying to trigger the exhaust closing to coincide with the minimum, such as shown near 7.22 seconds in Figure 5.13, the engine produced inconsistent combustions. Although not well enough instrumented to understand exactly why this was the case, it is conjectured that injecting air and propane while the piston’s membrane moved away from the combustion head may have helped draw the

injected gas into the combustion chamber in a more repeatable manner. Further instrumentation of the engine, such as optical position sensing of the membrane, would improve the performance. After the exhaust is commanded closed, the controller waits a short preset amount of time (on the order of 5 ms or less) before restarting the next cycle to ensure the exhaust valve was closed.

VIII. Experimental results

The following plots show the measured pressure from the reservoir and compressor head during operation at different pressures. Fig. 5.14 demonstrates consistent combustion and pumping which pressurized the reservoir from 781 kPa to 800 kPa.

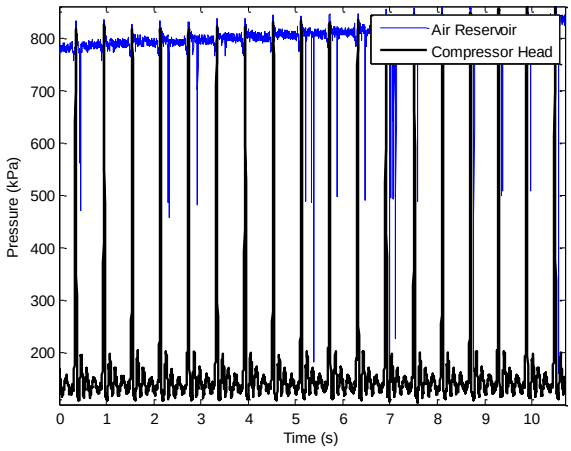

Figure 5.14 - Pressure inside compressor head and reservoir during run 1

Fig. 5.15 demonstrates consistent combustion and pumping which pressurized the reservoir from 922 kPa to 1005 kPa.

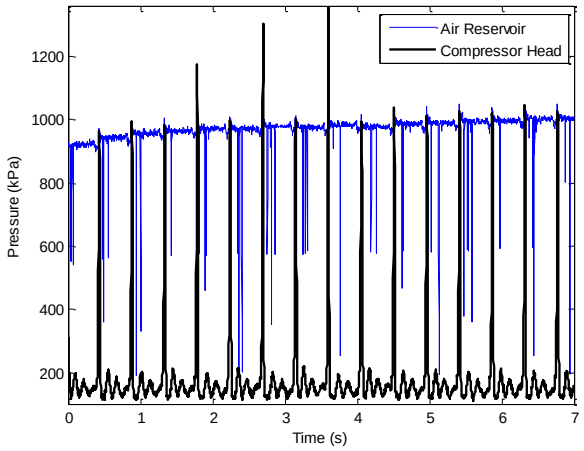

Figure 5.15 - Pressure inside compressor head and reservoir during run 2

Fig. 5.16 demonstrates combustion and pumping which pressurized the reservoir from 1129 kPa to 1187 kPa, and from 1160 kPa to 1177 kPa, with a misfire in between. The misfire can be seen at approximately 11 seconds into the run when the compressor head pressure does not exceed 400 kPa and the air reservoir drops. The pressure drops because air is needed for the next cycle's injection yet none was added to the reservoir. Therefore, this run also demonstrates the controller's ability to recover from a misfire.

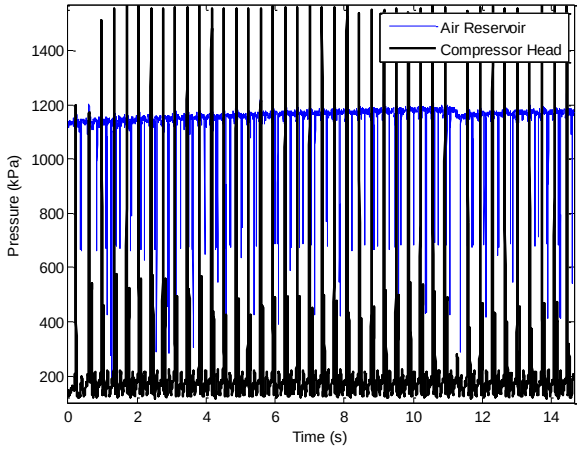

Figure 5.16 - Pressure inside compressor head and reservoir during runs 3 and 4

Table 5.2 summarizes the findings from the runs depicted in Fig. 5.14-Fig. 5.16. Figure 5.16 consists of runs 3 and 4 which are separated by a misfire.

Table 5.2 - Efficiency, power, and pressure for reservoir pressure for the runs presented in this paper

	Run 1	Run 2	Run 3	Run 4
Efficiency (%)	1.73	4.94	1.51	1.39
Mean Power (W)	2.40	6.08	2.88	2.98
Starting Pressure (kPa)	781	922	1129	1160
Ending Pressure (kPa)	834	1005	1187	1177

The limited reliability of various components of the engine compressor prevented further testing and optimization, which may have increased engine performance. Reliability was an issue with the membranes, which would break and require the engine to be disassembled for their replacement. Possible mechanisms for failure of the membranes were: (1) the strength of the membranes was inadequate, (2) the variability in the motion of the piston would periodically collide the membrane with the back of the compressor head causing a tear, (3) the spark plug inside the combustion head was sharp and tore the combustion-side membrane, (4) the membrane broke when the controller parameters were changed. All of these mechanisms were

observed during the operation of the engine compressor. Ultimately the compressor head cracked and prevented further testing. Due to the complex shape of the compressor head, it was not possible to refabricate the compressor head from a stronger material with the budget available.

Despite the low efficiency of the device, the goal of increasing the maximum output pressure was achieved. The output pressure of the device increased to 1187 kPa, which is higher than that of previous iterations. Riofrio [1], Willhite [35], and Yong [36] demonstrated closed loop pumping pressures up to 577 kPa, 589 kPa, 722 kPa, respectively.

IX. Conclusion

The free piston engine compressor described in this paper is an evolution of an engine developed by Riofrio [1], Willhite [35], and Yong [36]. The changes include moving all electronics onboard, implementing a new controller, and a figure-8 piston configuration which reduced the dynamic forces and moments on an external support. The dynamics of the engine compressor and the design requirements are shown to be similar to that of a buck converter. The Reynolds' transport theorem mathematically demonstrates the ability of the engine compressor to self-balance despite only having a single cylinder. A closed loop controller is utilized to determine the timings of air and fuel injection, the spark plug and the exhaust valve. The pumping pressure of the device is increased by improving the nozzles and the pump chamber's outlet check valve. This check valve was designed to satisfy a new criterion that evaluates the time required for the valve to fully open. Experimental results demonstrate an increased pumping pressure over the previous device from 722 kPa to 1187 kPa.

Acknowledgment

This work was supported by the Center for Compact and Efficient Fluid Power, an NSF Engineering Research Center, grant EEC-0540834.

References

[1i] Willhite, J. A. (2010). Dynamic Model-Based Design, Validation, and Characterization of a Compact, High-Inertance Free Liquid Piston Engine Compressor. Dissertation, Vanderbilt University. Retrieved from Vanderbilt University Electronic Theses and Dissertations (etd - 12102010-11502)

[2i] Yong, C. (2011). *A Virtual-Cam Based Control Methodology for Free-Piston Engines*. Dissertation, Vanderbilt University. Retrieved from Vanderbilt University Electronic Theses and Dissertations (etd – 07282011-114037)

[3i] Riofrio, J. A. (2008). *Design, Modeling and Experimental Characterization of a Free Liquid-Piston Engine Compressor with Separated Combustion Chamber*. Dissertation, Vanderbilt

University. Retrieved from Vanderbilt University Electronic Theses and Dissertations (etd - 12102010-11502)

[4i] L. Tian et al., "Miniature HCCI Free-Piston Engine Compressor for Orthosis Application", Proceedings of JSAE/SAE Small Engine Technology Conference 2009, Nov 3-5, 2009, Penang, Malaysia.

[1] J. A. Riofrio, “Design, Modeling and Experimental Characterization of a Free Liquid-Piston Engine with separated combustion chamber”, Ph.D. dissertation, Department of Mechanical Engineering, Vanderbilt University, TN, 2008.

[2] Pescara R. P., Motor compressor apparatus, US Patent 1,657,641, 1928.

[3] Pescara R. P., Motor compressor of the free piston type, US Patent 2,241,957, 1941.

[4] Toutant W. T., “The Worthington-Junkers free-piston air compressor”, Journal of the American Society of Naval Engineers”, 1952:64(3):583-594.

[5] Huber R., “Present state and future outlook of the free-piston engine”, Transactions of the ASME, 1958:80(8):1779-1790.

[6] London A. L, Oppenheim A. K., “The free-piston engine development – Present status and design aspects”, Transactions of the ASME, 1952:74(2):1349-1361.

[7] Underwood A. F., “The GMR 4-4 “HYPREX” engine – A concept of the free-piston engine for automotive use”, SAE Transactions 1957:65:377-391.

[8] Amann C. A., “Evaluating alternative internal combustion engines: 1950-1975”, Transactions of the ASME – Journal of Engineering for gas turbines and power, 1999:121:540-5.

[9] Specht D. H., “Evaluation of free piston-gas turbine marine propulsion machinery in GTS William Patterson”, SAE Paper 620280, 1962.

[10] Frey D. N., Klotsch P., Egli A., “The automotive free-piston-turbine engine”, SAE Technical Paper 570051, 1957.

[11] Noren O. B., Erwin R. L., “The future of the free-piston engine in commercial vehicles”, SAE Technical Paper 580032, 1958.

[12] Achten P. A. J., Van den Oever J. P. J., Potma J., Vael G. E. M., “Horsepower with brains: The design of the CHIRON Free Piston Engine”, SAE Technical Paper 2000-01-2545, 2000.

[13] Tikkanen S., Lammila M., Herranen M., Vilenius M., “First cycles of the dual hydraulic free piston engine”, SAE Technical Paper 2000-01-2546, 2000.

[14] Tikkanen S., Vilenius M., “Control of a dual hydraulic free piston engine”, International Journal of Vehicle Autonomous Systems, 2006:4(1):3-23.

[15] Clark N., Nandkumar S., Atkinson C., Atkinson R., McDaniel T., Petreanu S. et al., “Operation of a small-bore two-stroke linear engine”, Proc. of the fall Technical Conference of the ASME Internal Combustion Engine Division, 1998:31-1:33-40.

[16] Clark N., Nandkumar S., Atkinson C., Atkinson R., McDaniel T., Petreanu, S. et al., “Modeling and development of a linear engine”, ASME Spring Conference, Internal Combustion Engine Division, 1998:30(2):49–57.

[17] Famouri P., Cawthorne W. R., Clark N., Nandkumar S., Atkinson C., Atkinson R. et al., “Design and testing of a novel linear alternator and engine system for remote electrical power generation”, Proc. IEEE Power Engineering Society winter meeting, pp. 108–112, 1999.

[18] Clark N., Nandkumar S., Atkinson C., Atkinson R., McDaniel T., Petreanu S. et al., “Numerical simulation of a two-stroke linear engine-alternator combination”, SAE Paper 1999-01-0921, 1999.

[19] Clark N., Nandkumar S., Atkinson C., Atkinson R., McDaniel T., Petreanu S. et al., “Fundamental analysis of a linear two-cylinder internal combustion engine”, SAE Paper 982692, 1998.

[20] Van Blarigan P., “Advanced Internal Combustion Electrical Generator”, Proc. 2002 U.S. DOE Hydrogen Program Review, NREL/CP-610-32405, 2002.

[21] Carter D., Wechner E., “The Free Piston Power Pack: Sustainable Power for Hybrid Electric Vehicles”, SAE Technical Paper 2003-01-3277, 2003.

[22] SunPower Corp. (2013). High Performance Free-Piston Stirling Engines [Brochure]. Retrieved November 11, 2013 from http://www.sunpowerinc.com/library/pdf/productlit/Engine%20Brochure.pdf

[23] Center for Compact and Efficient Fluid Power. (2013). Free-piston Engine Compressor. Retrieved November 11, 2013 from http://www.ccefp.org/research/thrust-2-compactness/project-2b1

[24] Super Military Battery. (2009). Specification of Military Battery BB-2557/U Battery (Li-ion) [Brochure]. Retrieved November 11, 2013 from http://www.super-military-battery.com

[25] iRobot Corp. (2013). iRobot 310 SUGV [Brochure]. Retrieved November 11, 2013 from http://www.irobot.com/~/media/Files/Robots/Defense/SUGV/iRobot-310-SUGV-Specs.ashx

[26] SPG Media Ltd. (2012). UK Afghanistan Forces to get Dragon Runner Robots [Brochure]. Retrieved November 11, 2013 from http://www.army-technology.com/news/news70214.html

[27] SupplyNet, Inc. (2013). BB-2590/U Rechargable Lithium-Ion Battery with SMBus V1.1 [Brochure]. Retrieved November 11, 2013 from http://www.maifl.com/pdfs/BB2590.pdf

[28] QinetiQ Group. (2013). Dragon Runner SUGV [Brochure]. Retrieved November 11, 2013 from http://www.qinetiq.com/what/capabilities/land/Documents/Dragon-Runner-SUGV.pdf

[29] ICOR Technology, Inc. (2013). MK3-Caliber Medium EOD Robot [Brochure]. Retrieved November 11, 2013 from http://icortechnology.com/wp-content/uploads/2013/03/MK3-CALIBER-V.2013.01.14.pdf

[30] Raibert M., Blankespoor K., Nelson G., Playter R., "BigDog, the Rough-Terrain Quadruped Robot", Proc. 17th International Federation of Automatic Control (IFAC), vol. 17, 2008.

[31] American Honda Motor Corp. Inc., (2013). ASIMO Frequently Asked Questions [Brochure]. Retrieved November 11, 2013 from http://asimo.honda.com/downloads/pdf/asimo-technical-faq.pdf

[32] TOSY Robotics JSC. (2013). TOPIO TOSY Pingpong Playing Robot [Brochure]. Retrieved November 11, 2013 from http://topio.tosy.com/spec.shtml

[33] Aldebaran-Robotics. (2013). Nao H25 Humanoid Robot Platform [Brochure]. Retrieved November 11, 2013 from https://developer.aldebaran-robotics.com/nao/

[34] H. T. Aichlmayr, "Design Considerations, Modeling, and Analysis of Micro-Homogeneous Charge Compression Ignition Combustion Free-Piston Engines", Ph.D. dissertation, University of Minnesota, MN, 2002.

[35] Willhite, J. A. (2010). *Dynamic Model-Based Design, Validation, and Characterization of a Compact, High-Inertance Free Liquid Piston Engine Compressor*. Dissertation, Vanderbilt University. Retrieved from Vanderbilt University Electronic Theses and Dissertations (etd - 12102010-11502)

[36] Yong, C. (2011). *A Virtual-Cam Based Control Methodology for Free-Piston Engines*. Dissertation, Vanderbilt University. Retrieved from Vanderbilt University Electronic Theses and Dissertations (etd – 07282011-114037)

[37] M. E. Hofacker, M. Sun, E. J. Barth. "Design of a Figure-Eight free-liquid-piston engine compressor for compact robot power". *2012 ASME Dynamic Systems and Control Conference and Bath/ASME Symposium on Fluid Power & Motion Control (FPMC 2012),* pp. 595-607, September 12-14, 2012. Bath, U K.

[38] Willhite, J.A., Yong C, Barth E.J. "The High Inertance Free Piston Engine Compressor— Part I: Dynamic Modeling". Journal of Dynamic Systems, Measurement, and Control. 2013.

[39] Willhite, J.A., Yong C, Barth E.J. "The High Inertance Free Piston Engine Compressor— Part II: Design and Experimental Evaluation". Journal of Dynamic Systems, Measurement, and Control. 2013.

6. Dynamic Simulation and Experimental Validation of a Single Stage Thermocompressor for a Pneumatic Ankle-Foot Orthosis

Mark E. Hofacker, Nithin S. Kumar, and Eric J. Barth

Vanderbilt University

Nashville, TN

From: ASME/BATH Proceedings of the 25th Symposium on Fluid Power & Motion Control

Status: Published October, 2013

Prologue

This paper presents an experimentally validated Stirling thermocompressor. The impedance view of the Stirling thermocompressor is shown in Figure 6.i. In the overall impedance framework proposed by this dissertation, the work on the Stirling thermocompressor primarily considers modifying the energy source to offer a good match to the source and load impedances. The load impedance is largely fixed in terms of its dynamics, but optimization of the energy source and source impedance was possible. This optimization entailed enhancing the heat transfer through a novel in-cylinder heat exchanger configuration and by directly controlling the frequency of operation.

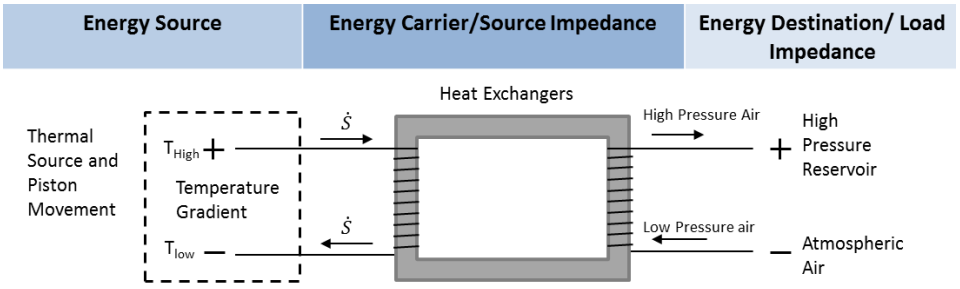

Figure 6.i – Electrical circuit approximation of the Stirling thermocompressor as a solid core transformer

A Stirling thermocompressor requires a cyclical temperature gradient to operate. In this way, the thermo compressor is similar to a solid core transformer as shown in Figure 6.i. With a solid core transformer, an AC source provides a means of raising the potential of the output even though no current from the source is delivered to the load. In a similar manner, the thermocompressor uses energy from the oscillating thermal gradient to raise the potential of

atmospheric air. With a solid core transformer this transfer of energy is accomplished through magnetic flux, whereas with the thermocompressor the energy is transferred through its heat exchangers. In both devices the carrier domain, magnetic and thermal, is a means to transfer energy to the desired output, electric and pneumatic.

The energy domains in the Stirling thermocompressor include the electrical, mechanical, chemical, thermal, and pneumatic. Two energy sources are required for operation of the thermocompressor. The first is a thermal source such as propane or electric heaters. The second energy source is electrical, specifically the batteries that were used to drive the electric motor which in turn drives the displacer piston. Together, the heater head and displacer piston create an oscillating thermal source. The thermocompressor's carrier domains include the thermal and pneumatic. The thermal and pneumatic domains serve to increase and decrease the pressure of the working fluid.

The design goals of this project are similar to that of the bridge vibration energy harvester in that both projects are trying to aid in the recovery of power from one domain (thermal and mechanical, respectively), while minimizing the amount of electrical power invested. In both projects, reducing electrical power consumption was pursued through unique decisions regarding mechanical design. With the bridge vibration energy harvester damping was reduced by utilizing compliant mechanisms which removed the need for a bearing surface. With the thermocompressor, the reciprocating lead screw was implemented so that the motor did not need to continuously change direction.

The thermocompressor shares design goals with the free piston engine compressor in that both projects seek to efficiently preserve the high energy density of a hydrocarbon fuel source when it is converted to pneumatic potential. In the case of the thermocompressor, it was the application of in-cylinder heat exchangers that allowed the thermal energy to be transferred quickly to the working fluid. In the case of the free-piston engine compressor, it was the piston's inertia that maintained compression and allowed for efficient combustion.

The primary bottlenecks addressed in this project are the interrelated issues of low operating frequency and limited rate of heat transfer to the working fluid. This was addressed through the inclusion of in cylinder heat exchangers which make high operating frequencies possible while still maintaining a high pressure ratio without significant additions to dead volume.

This manuscript therefore advances the field of Stirling devices through the active modulation of the displacer piston and through the inclusion of in-cylinder heat exchangers. Both of these contributions aid greatly in the pursuit of creating a useful and viable untethered Stirling thermocompressor.

Much of the work related to the design and control of a Stirling thermocompressor was performed decades ago in pursuit of creating an artificial heart [1i]. Since then, a majority of the work has focused on an advanced modeling and simulation [2i]. Edwards constructed a miniature

prototype Stirling thermocompressor and used it to characterize an analytical model [3i]. This device was not intended to be used as an untethered power supply and focused on the modeling and design of the regenerator. It did not seek to address practical considerations such as electrical power consumption, and pursued increases in rates of heat transfer through the use of helium and nitrogen as a working fluid.

Abstract

The mechanical design, modeling, and partial experimental validation of a prototype Stirling thermocompressor is presented in this paper. The thermocompressor is intended to serve as a compact and quiet, untethered 50 W, pneumatic power supply for an ankle foot orthosis. The goal of high efficiency at the target power density is pursued through the use of novel heat exchangers and high operating temperature and frequency. The motion of the displacer piston is controlled utilizing a brushless DC motor driving a continuous linear reciprocating screw. This paper presents the experimental validation of the heat transfer and pressure dynamics portions of the thermocompressor, leaving the modeling and validation of mass transfer to future work.

Nomenclature

γ Specific heat ratio of air
η Dynamic viscosity (Nm/s^2)
α Angular position of motor (rad)
A Heat transfer area (m^2)
A_c Cross sectional area of cylinder (m^2)
c_p Specific heat of air at constant pressure (J/kgK)
d Stroke length (m)
E_{pneum} Pneumatic energy (J)
f Frequency (Hz)
h Convective heat transfer coefficient (W/m^{2}K)
H Enthalpy of control volume (J)
L_{piston} Piston length (m)
m Mass in control volume (kg)
m_{pumped} Air mass pumped per cycle (kg)
P Pressure in control volume (Pa)
P_{atm} Atmospheric air pressure (Pa)
P_d Downstream pressure (Pa)
P_{pneum} Pneumatic power (W)
P_{res} Pressure of air reservoir (Pa)
P_u Upstream pressure (Pa)
$\dot{Q}$ Heat flow into control volume (J)
r_{piston} Piston radius (m)
R Universal gas constant (J/kgK)
s Diametral clearance (m)
T Temperature in control volume (K)
T_{flow} Temperature of $\dot{m}$ (K)
T_k Minimum temperature of air (K)
T_h Maximum temperature of air (K)
$T_{wall,\,h}$ Temperature of cylinder wall in V_h (K)
$T_{wall,\,k}$ Temperature of cylinder wall in V_k (K)
U Internal energy of control volume (J)
V Volume in control volume (m^3)
V_k Volume in cold chamber control volume (m^3)
$V_{k,\min}$ Minimum volume in V_k (m^3)
V_h Volume in hot chamber control volume (m^3)
$V_{h,\min}$ Minimum volume in V_h (m^3)
V_0 Initial volume in control volume (m^3)
W Mechanical work on control volume (J)
x Displacer piston position (m)
z Rotations per cycle

I. Introduction

Ankle-foot orthoses (AFOs) function as gait assisting devices for individuals suffering from ankle impairment. Commercially available passive AFOs are compact and durable but lack functionality since they cannot provide active motion control or generate net power. Their powered counterparts lack utility because they require tethered power supplies. The Center for Compact and Efficient Fluid Power (CCEFP) has proposed the development of a pneumatically powered, untethered and compact AFO to address the shortcomings of both passive and active AFOs. The initial prototype was powered by a 266 mL bottle of compressed CO_2 and achieved an operating time of 37.5 min for 1914 steps [1]. The proposed Stirling thermocompressor is intended to serve as a compact pneumatic power supply for the AFO, which would greatly improve its operating duration due to its energy dense hydrocarbon fuel source.

A thermocompressor directly uses thermal energy of a heat source to increase the pressure of its working fluid, without any mechanical work output (such as conventional IC engines powering a compressor). By storing the output of the thermocompressor in a high-pressure reservoir, this power supply and storage system would potentially extend the operating time of the AFO, by converting thermal energy of a high energy density hydrocarbon fuel source to pneumatic energy in the form of high-pressure air. For comparison, a 266 mL propane bottle would contain enough chemical energy to power the AFO for 4 hours at an efficiency of 6.6%. In order to meet the energetic requirements of the AFO, the thermocompressor would have to output air at 80 psig (for the pneumatic actuator), supply 50 W of pneumatic energy to the reservoir, and weigh less than 500 g to minimize external weight to an user's impaired ankle.

The concept of the thermocompressor was conceived by Bush who filed a patent in 1939 describing a direct thermal compressor, which converts thermal energy to potential energy of compressed gas without any mechanical interference [2]. The National Heart, Lung, and Blood Institute contracted several groups to conduct artificial heart research and development in the early 1960s; three groups developed experimental thermocompressors to function as miniature power supplies. In 1969, McDonald Douglas Corporation [3-4] demonstrated an argon filled 30 W thermocompressor operating at 10.5 Hz between 294 K and 924 K. Two years later, Air Products and Chemicals [5] built a helium-based 4.1 W thermocompressor operating at 13 Hz between 325 K and 830 K. More than a decade later, Aerojet [6-12] constructed a thermocompressor using helium as the working fluid operating between 320 K and 900 K with a radioisotope heat source and a power output of 6 W.

Developments since the 1980s have focused on the theoretical aspects of thermocompressors. In 1996, Kornhauser [13] analyzed a single stage thermocompressor using isothermal models and demonstrated that for temperature ratios greater than 2.5, the ideal thermocompressor requires less heat input than an Otto-driven compressor (for a compression ratio of 8). A year later, Arquès [14] developed a model of piston motion in an idealized

thermocompressor. His model integrated effects of heat transfer and variable mass and allowed for the calculation of working fluid temperature and pressure in both hot and cold volumes and piston position using models from Beans [15] and Berchowitz et al. [16]. In 2003, Karabulut [17] thermodynamically analyzed an ideal Bush engine and calculated the mass ratio (pumped mass/total mass) and pressure ratio (maximum pressure ratio/ambient pressure) as a function of temperature ratio with a cold side temperature of 300 K (for instance, a temperature ratio of 3.5 corresponds to a mass ratio of around 0.4 and a pressure ratio of 3.5). Karabulut also demonstrated that a Bush engine operating between 300 K and 1000 K at 1500 rpm (25 Hz) would generate 700 W specific power per liter stroke volume. In 2005, Edwards [18] developed an analytical model of the thermocompressor cycle, which accounted for dead volume in the cylinder and regenerator. The pressure ratios of his experimental prototype (tested with nitrogen and helium as working fluids) is around 75% of the temperature ratios. His prototype demonstrated pressures up to 22 psia (helium, 13 Hz, temperature ratio of 1.9). Yarger et al. [19] built a mesoscale two-phase thermocompressor, which demonstrated an average pressure swing of 51 psi (352 kPa) operating between room temperature and 423 K at 13 rpm, and reported that the cyclic pressure swing and pressure ratio decreased as operational frequency increased.

Other forms of compact power supplies for sub-human scale mobile devices that have been experimentally and commercially validated include batteries/motors, free piston compressors, homogeneous charge compression ignition (HCCI) engines, and hydraulic actuation-based engines.

The prevalence of electrochemical batteries as power supplies for untethered applications, such as humanoid robots is due to their low cost, availability, and the easy implementation of DC motor actuation. Honda's ASIMO runs on a 51.8 V Li-ion rechargeable battery, which weighs 6 kg, takes 3 hours to fully charge and provides the ASIMO with 1 hour of operation. Aldebaran's Nao robot has a 27.6 Whr battery, which takes 2 hours to fully charge and provides the Nao with 1.5 hours of operating time. Other programmable humanoid robots are similarly powered by NiMH or Li-ion batteries and actuated by DC servo motors. Using this form of power for applications such as the AFO poses challenges due to the low overall system energy density (~145-260 kJ/kg) [20] and bulkiness of electromagnetic actuators. These considerations are important since Tian et al. [21] estimate that an ankle requires 70 kJ per day (for a 10,000 step day). To avoid excessive stress on impaired ankles, a more energy dense solution is required.

Free piston compressors are an alternative form of onboard power supplies for untethered robotic applications. Initially used for large-scale power production, interest in this technology has renewed due to the potential for lower emissions, reduced fuel consumption and mechanically simpler designs relative to conventional IC engines. Willhite [22] reports the experimental validation of a free liquid-piston engine compressor, which uses the combustion of a propane-air mixture to produce high-pressure air to serve as a power supply for a pneumatic system such as

a rescue robot. His experimental prototype demonstrated an average isothermal power output of 17.9 W at an efficiency of 6.3%. However, the miniaturization of such a device would increase viscous friction, coulomb friction, leakage, quenching, and heat loss. Furthermore, other challenges include implementing an exhaust mechanism and fuel injection on a small scale, which requires complex designs and high production costs.

The miniature free-piston two-stroke homogeneous charge compression ignition (HCCI) engine constructed by Tian et al., [21] is a potential alternative to power the AFO. HCCI engines operate by compressing fuel and air until the mixture self-ignites and are usually characterized by rapid combustion, high efficiencies, and the reduction of certain emissions. However, Tian et al. report leakage (through the cylinder-piston gap), which increases as the engine is miniaturized, and ignition control difficulties at high speeds (above 40,000 rpm). The validated prototype was dynamically simulated with an overall system efficiency of 5.9%, which would result in higher power densities than batteries. The practical use of an HCCI engine compressor would require addressing the issue of noise caused by the operation of an IC engine (especially in close proximity to an AFO user).

Miniaturizing hydraulic systems would also pose several challenges. Though such systems have high volumetric power densities (~10 times that of battery and motor actuation) and are compatible with a variety of actuators, they require reservoirs, control valves, accumulators, and return lines, all of which would greatly increase the bulk of the device. A power supply using this form of actuation has been shown to be effective for larger applications such Boston Dynamics' BigDog, a four-legged, rough-terrain robot capable of walking, running, and climbing [23]. The 109 kg BigDog is powered by a two-stroke internal combustion engine (15 hp), which drives a hydraulic pump and has successfully operated continuously for 2.5 hours. However, for a device (on the order of kilograms) such as the AFO, this form of power and actuation is not feasible.

A Stirling thermocompressor, such as the proposed device, converts thermal energy from a heat source to pneumatic energy of high-pressure working fluid. This conversion process is efficient (theoretically at Carnot efficiency) because there is no intermediate conversion to mechanical energy. A limiting factor in Stirling engines is the heat transfer rate, the effects of which dominate at smaller cylinder diameters [24]. To enhance heat transfer, a novel in-piston heat exchanger mechanism is implemented in the thermocompressor and is discussed in this paper.

There has been much work done regarding heat exchangers in Stirling engines. In 1980, Rao [25] patented a heat exchanging assembly for use in Stirling engine heater heads to address the cracking of metal tubes under thermal and mechanical stresses during engine operation. His proposed assembly is made up a ceramic, fabricated by heating a cheap, extrudable material in a carburizing furnace, and can be used with working fluids up to 200 atm and 980°C. Fujiwara et al. [26] patented another form of heat exchanger for a Stirling engine in 1987, wherein a domed

cylinder serves as a high-temperature enclosure with an integrated regenerator and can withstand pressures up to 60 atm. Recently, Hirao et al. [27] have attempted to improve the specific power of Stirling engines by implementing a novel heating and cooling apparatus. The prototype heat exchanger consists of an inner and outer tube, between which the working fluid is free to flow. A combustor is placed at one end of the inner tube and heat is transferred to the working fluid through the heated wall. Fuel gas is used to cool the working fluid (using its heat of vaporization) and is then sent to the combustor, eliminating the need for a cooling mechanism (e.g., water or a radiator) thereby decreasing the weight of the system. The performance of the proposed heat exchanger is compared to multi-tube heat exchangers in a prototype Stirling engine. Experimental results indicate that the Stirling engine with the proposed heat exchanger outperforms the multi-tube heat exchanger with higher pressure swings (~120 kPa versus ~80 kPa), shaft torque (~0.3 Nm versus ~0.25 Nm at 50 Hz), and output power (95 W versus 75 W at 50 Hz). In this paper, a novel heat exchanger consisting of stacks of thin metal collapsible discs is described, simulated, and experimentally validated.

II. Operation of Thermocompressor

The proposed Stirling thermocompressor shuttles air between its heat source and a room temperature heat sink using a displacer piston. This cyclical heating and cooling of the working fluid results in the conversion of thermal energy to pneumatic energy. The loose-fit piston enables airflow between the heat source and sink as the piston is moved from TDC to BDC. As the working fluid is exposed to the heat source, its temperature and pressure increases and conversely, they decrease when the piston is at TDC. Check valves enable the transfer of atmospheric air into and transfer of high-pressure air out of the cylinder. Figure 6.1 illustrates this operating mechanism.

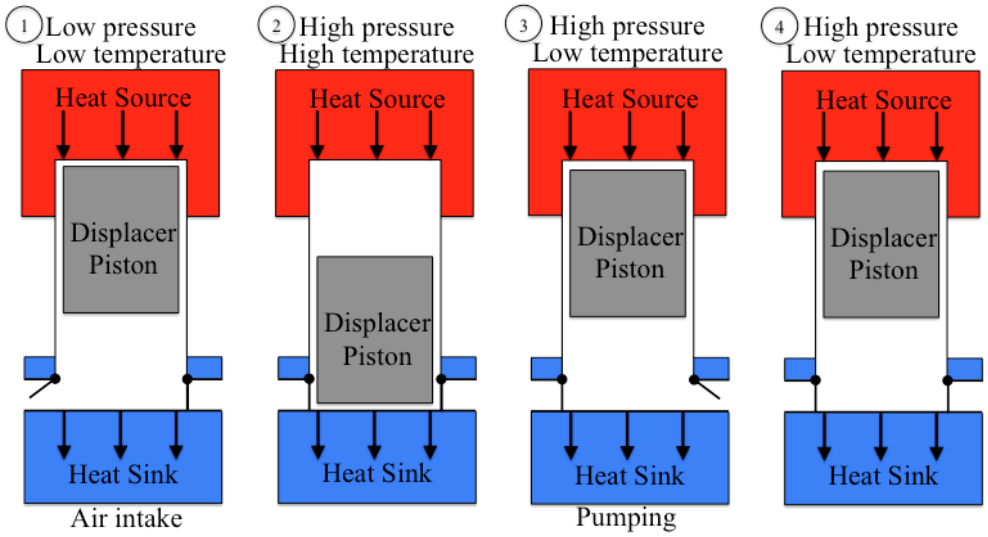

Figure 6.1 - Schematic illustrating the operation of single-stage thermocompressor

The pressure ratio of the thermocompressor, defined as the ratio of the output pressure to the intake pressure, is determined by the temperature ratio and the number of compression stages. For the single stage prototype discussed in this paper, the temperature ratio is maximized to obtain the highest pressure output.

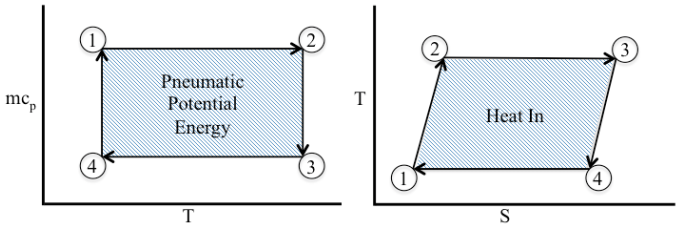

Figure 6.2 - Mass-temperature and temperature-entropy diagrams of Stirling thermocompressor operation

Figure 6.2 relates the operation of the proposed thermocompressor (Figure 6.1) to the changes in temperature, entropy, and mass of the working fluid in the cylinder. Air intake represents an increase in mass (stages 4 to 1) and heat addition represents a rise in temperature and entropy of the working fluid (stages 1 to 2). Pumping is a decrease in mass and an increase in entropy of air (stages 2 to 3). When the check valve closes with the displacer piston at TDC, the temperature of air decreases (stages 3 to 4).

III. Design of Thermocompressor

The final prototype thermocompressor is required to output air at 80 psig to power the AFO's pneumatic rotary actuator. For a single stage thermocompressor to reach this output pressure in a single stage, it would have to maintain a heat source temperature of over 1600°C, which is impractical for use with most common materials. Accordingly, the initial prototype is designed to

sustain the highest temperature heat source with non-exotic materials and is limited to a source temperature of 1000°C. At least two stages are required to reach the target pressure of 80 psig (with the output from the first stage reaching at least 23 psig). The device described in this paper is a single stage prototype intended as one of the two required stages.

A brushless DC motor is used to drive a continuous linear reciprocating screw, onto which the displacer piston is affixed. The reciprocating screw is similar to a lead screw but differs in that the screw has a "criss-crossed" left-handed and right-handed thread to enable reciprocating motion of the nut with unidirectional screw rotation. This enables the reciprocating screw to be driven at constant velocity, while the piston position-time graph resembles a triangle wave profile. This is beneficial since the use of the reciprocating screw reduces motor power consumption (a lead screw would require accelerating and decelerating the motor shaft every cycle) and is easy to control.

The reciprocating screw is the Abu Garcia 7000 series carriage screw (stroke of 1.7" with 20 turns per stroke). The brushless DC motor used in the thermocompressor prototype is the 9.3 W (max) Faulhaber 1226 with a 16:1 gearhead and a Hall effect sensor, capable of a no-load speed of 1700 rpm. The motor is controlled by an Advanced Motion Controls AZBE6A8 PWM servo drive. The displacer piston is made from Macor machinable ceramic, which was selected for its low thermal conductivity (1.46 W/mK at 25°C), high service temperature (1000°C), and machinability. A low thermal conductivity piston is crucial for the prototype, since significant heat flow from the heat source to the sink on a device of this scale leads to losses and low efficiencies. An exploded view of the mechanism used to drive the displacer piston is shown in Figure 6.3.

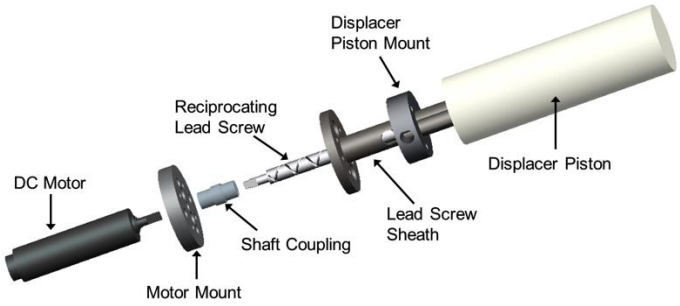

Figure 6.3 - CAD drawing of piston-motor assembly

The working fluid is bound between the heat source and sink by a fused quartz cylinder manufactured by Technical Glass Products. Fused quartz was chosen because of its ability to withstand high temperature and its low thermal conductivity (for reduced heat flow along the cylinder walls). Physical and thermal properties of the fused quartz include a strain point of 1120°C, a thermal conductivity of 1.4 W/mK at 20°C, and a coefficient of thermal expansion of 5.5×10^{-7} m/m°C. The cylinder is sealed to the heater head via a high temperature gasket (Klinger

Milam PSS 150).

The heat source for the final thermocompressor device will be hydrocarbon fuel. For this prototype, miniature high-temperature cartridge heaters are utilized for easy implementation. The controller for the heaters is the JLD612 Dual Display PID Temperature Controller (K-type thermocouple). The heater head is designed to accommodate six 60 W cartridge heaters.

The prototype incorporates openings for two valves and a pressure transducer in the cooler head as shown in the cross sectional view of the prototype in Figure 6.4 (pressure transducer opening not shown). There is no pumping of working fluid into or out of the thermocompressor so the two valve openings are plugged during testing and valve dynamics are not considered at this time. Future prototypes will utilize a high flow rate valve such as flapper-type that will minimize flow restriction.

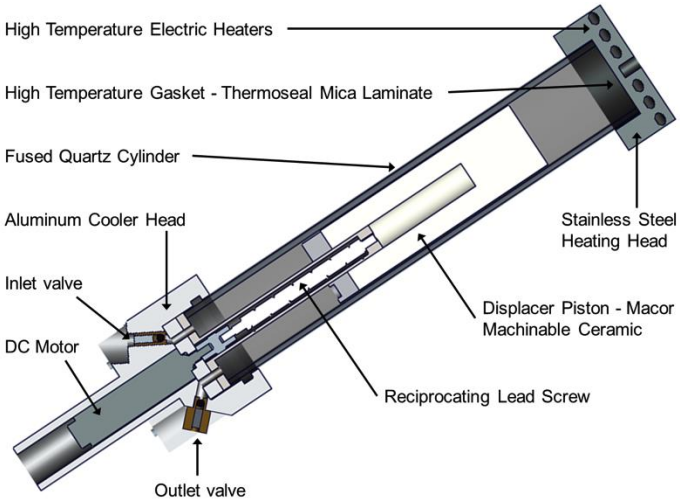

Figure 6.4 - Cross section of thermocompressor showing internal components

The heat exchangers used in the thermocompressor are stacks of thin, circular stainless steel shim stock. The steel is manufactured by Lyon Industries and each disc has a thickness of 0.002" and a thermal conductivity of 21.5 W/mK at 500°C. The relatively high thermal conductivity of the steel ensures that the discs rapidly heat soak at TDC (Figure 6.5) when they are in direct contact with the heat source.

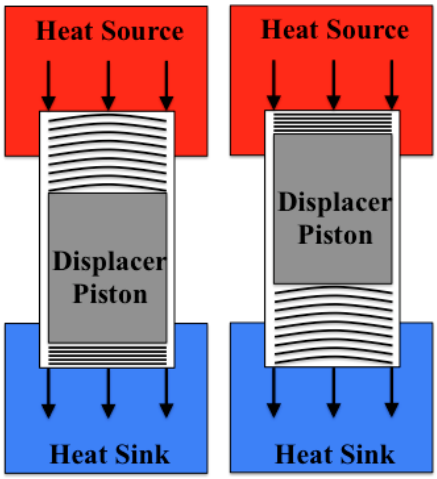

Figure 6.5 - Schematic of heat exchanger operation at BDC (left) and TDC (right)

The hot side heat exchangers are simply circular discs, but the cold side heat exchangers have a hole to accommodate the reciprocating screw housing piece (Figure 6.6).

Figure 6.6 - Collapsible, in-piston heat exchangers used in hot side (Left) and cold side (right)

The stack of discs acts akin to an accordion and bend into a dome when stretched (Figure 6.5). When the heat exchangers are stretched at BDC, there is increased surface area for air to gain thermal energy and increase its temperature and conversely, at TDC, the stretched heat exchangers below the displacer piston effectively increase the contact area between the hot, high-pressure air and the room temperature metal discs, which causes the working fluid to rapidly decrease its temperature.

A temperature compensated pressure transducer manufactured by Freescale Semiconductor model MPXA4250A is affixed onto the cooler head with an o-ring seal and is supported by two of the four tie rods that are parallel to the cylinder. The four tie rods serve to contain the working fluid within the fused quartz cylinder by maintaining compression using stiff coil springs. The retaining springs compensate for thermal expansion of the device. Due to the high temperature of the heat source, the heater head is made from stainless steel. The high service temperature

requirement is relaxed for the cooler head, which is made from aluminum for machining ease and its relatively high thermal conductivity. A photograph of the assembled thermocompressor, without heat exchangers and electric heaters, is shown in Figure 6.7.

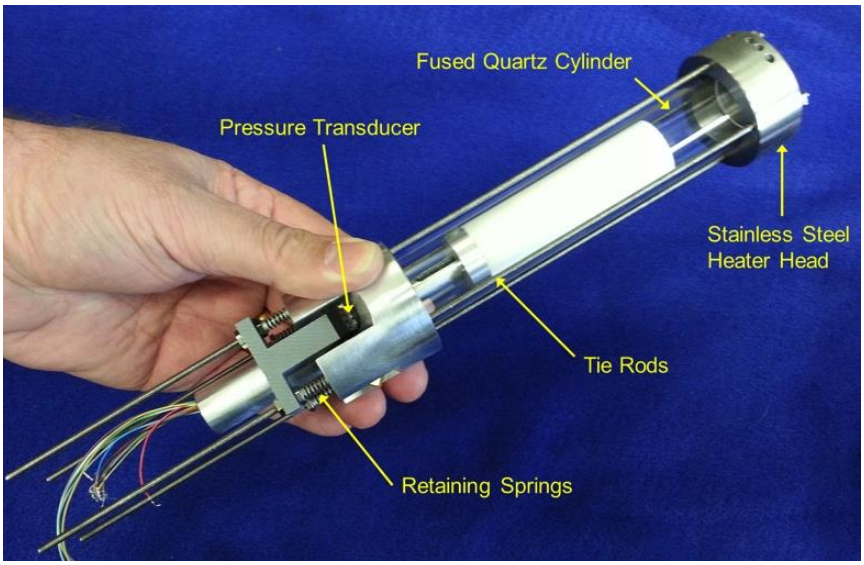

Figure 6.7 - Prototype thermocompressor without heat exchangers

IV. Dynamic Model

For the purposes of dynamic simulation, the operation of the thermocompressor is modeled as two control volumes of variable size. Each control volume represents the volume of working fluid in either the hot or cold side of the cylinder. Both control volumes are separated by a flow restriction, which represents airflow around the piston.

The input to the model is the angular position of the motor, which is run at constant angular velocity:

$$V = A_c d \,\mathrm{tri}\left(\frac{2\pi\theta}{z}\right) + V_0 \tag{1}$$

where the function $\mathrm{tri}(2\pi\theta/z)$ is a triangular wave of equal amplitude and frequency of its $\sin(2\pi\theta/z)$ analog. The walls and heat exchangers in the cold control volume (V_k) transfers thermal energy from the working fluid out of the thermocompressor and the walls and heat exchangers in the hot control volume (V_h) transfers thermal energy from the heat source to the working fluid. V_h and V_k are maintained at T_h and T_k, respectively, which represent the temperature of the conducting wall. The dead volume around the displacer piston is integrated in the model of V_h and the dead volume in the rest of the thermocompressor (in the reciprocating screw housing, check valve holes, and the motor) is added to V_k.

The pressure dynamics in the cylinder were derived by initially performing a power balance

on each control volume. Using a modification of the first law of thermodynamics, the rate of change in internal energy of the control volume is given by:

$$\dot{U} = \dot{H} + \dot{Q} - \dot{W} \tag{2}$$

Rearranging the terms and solving for the pressure dynamics inside the control volume yields:

$$\dot{P} = \frac{\sum \dot{m} c_p T_{flow} - \gamma P \dot{V} + hA\left(T_{wall} - T\right)}{V} \tag{3}$$

The mass flow restriction between the two control volumes was modeled using Grinnel's model of compressible fluid flow [28] in a thin passage, which is given by:

$$\dot{m} = \left(\frac{r_{piston} s^3}{12 \mu R T_{flow} L_{piston}} \right) \left(P_u^{\,2} - P_d^{\,2} \right) \tag{4}$$

The constants used in the implementation of Equations (1)-(4) are shown in Table 6.1.

Table 6.1 - Values of significant parameters

A_c = 491 mm^2	d = 44 mm
L_{piston} = 76.2 mm	r_{piston} = 11.95 mm
s = 1.1 mm	$T_{wall,\,h}$ = 1000ºC
$T_{wall,\,k}$ =50ºC	μ = 3.5×10^{-8} Ns/m^2
V_0 = 3700 mm^3	z = 8 rev/sec

The values of *h* and *A* are not listed in Table 6.1 since they were varied in simulation. Their values are shown in the experimental results section. The dynamic model implemented Equations (3)-(4) to demonstrate the effect of parameters such as inclusion of heat exchangers, temperature ratio, and operational frequency on the pressure in the thermocompressor. Since the prototype did not pump any working fluid, valve dynamics, and mass transfer into the device and to an external reservoir were not considered in the simulation.

V. Quasi-Static Model

A quasi-static model of the thermocompressor, similar to Schmidt's analysis of Stirling engines [29], was developed using the ideal gas law equation. This analysis presumes that pressure is only a function of displacer piston position, which is valid if the hot and cold sides are isothermally maintained, instantaneous heat transfer to and from the working fluid is achieved, pressure dynamics are slow enough for control volumes to achieve their steady-state temperatures, and if there is no mass flow restriction. These conditions are not always fulfilled since thermocompressor pressure is affected by less than instantaneous heat transfer rates when run at appreciable frequencies and mass flow restrictions around the displacer piston. Nevertheless, the quasi-static Schmidt temperature and the ideal gas law was applied to both control volumes to derive an expression for the working fluid pressure strictly as a function of position. This was done to find an upper bound representing complete and instantaneous heat transfer to/from the working fluid. The volumes of the hot and cold control volumes are given by:

$$V_h = V_{h,\min} + A_c(L_{piston} - x) \tag{5}$$

$$V_k = V_{k,\min} + A_c x \tag{6}$$

From the ideal gas law:

$$P = \frac{mR}{\left(\frac{V_h}{T_h} + \frac{V_k}{T_k}\right)} \tag{7}$$

Substituting Equations (5)-(6) into (7):

$$P = \frac{mR}{\frac{V_{h,\min} + A_c L_{piston}}{T_h} + \frac{V_{k,\min}}{T_k} + x\left(\frac{A_c}{T_k} - \frac{A_c}{T_h}\right)} \tag{8}$$

Equation 8 was implemented to derive a plot for the pressure as a function of position.

VI. Experimental Results

The dynamic and quasi-static models described above were validated using the experimental setup shown in Figures 6.3, 6.4, 6.6, and 6.7. The heater head was held at constant temperature and the piston was moved at constant velocity during testing. The frequency of the displacer piston was maintained at constant frequencies of 0.25, 1, or 2.8 Hz at each temperature. The highest frequency, 2.8 Hz, was chosen because it was the highest frequency that could be maintained without damaging the motor. Figure 6.8 below shows measured data from the thermocompressor compared to both the static and dynamic model described in the previous section of this paper.

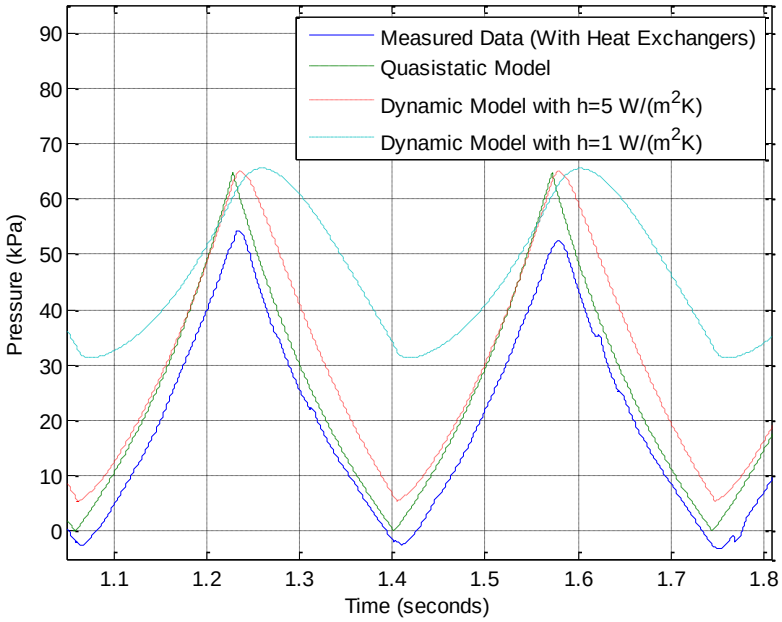

Figure 6.8 - Cold chamber pressure from experimental data and different models for 2.8 Hz operation and 600°C heater head temperature

It can be seen from this plot that both models are qualitatively similar to the recorded data. It appears that the rate of heat transfer is in the range 5-10 W/m^{2}K. The areas of heat transfer area in this model were calculated by estimating the amount of surface area presented by the heat exchangers and metal components inside of the compressor. It was determined that there was 1300 cm^2 of heat transfer area on the heater head and hot side heat exchangers and 990 cm^2 of heat transfer area on the cooler head and cold side heat exchangers. Although it was not physically detected, it is possible that there was a slow leak that prevented closer model match. It was difficult to maintain a seal at the heater head because of the high temperatures that it was exposed to.

To test the effectiveness of the heat exchangers and the accuracy of the model, the thermocompressor was operated without the heat exchangers. Figure 6.9 shows the predicted and measured response of the thermocompressor without heat exchangers.

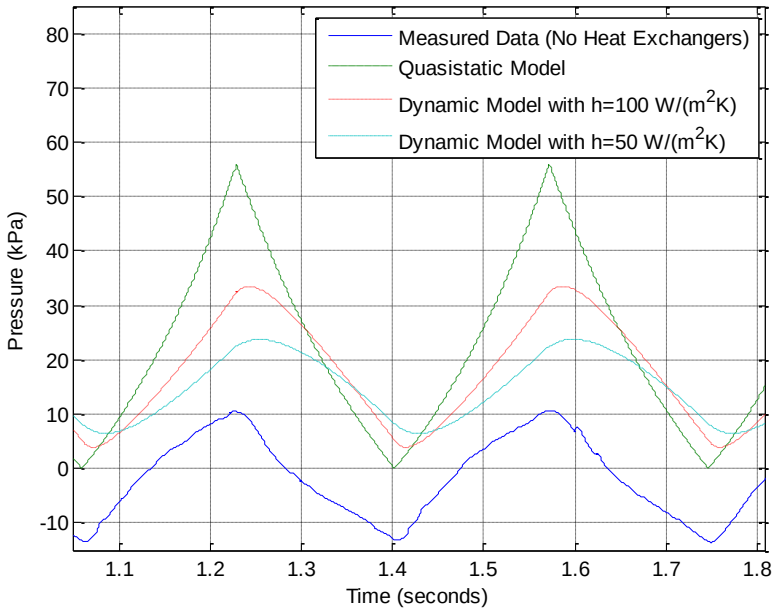

Figure 6.9 - Cold chamber pressure from experimental data and different models for 2.8 Hz operation and 600°C heater head with no heat exchangers present

Operating without heat exchangers, it was calculated that there was 4.57 cm^2 of heat transfer area on the hot side and 56.45 cm^2 of heat transfer area on the cold side. Even though the surface area was decreased, the coefficient of heat transfer appears to be greater than when the heat exchangers were present. During operation it was observed that some of the heat exchangers would stick together instead of fully expanding, which could explain this disparity. Nevertheless, overall heat transfer was shown to be significantly enhanced as indicated by comparing figures 6.8 and 6.9. It should be noted that the pressure swing of the quasi-static model was slightly lower for the case with no heat exchangers due to the slight increase in dead volume.

The thermocompressor was operated while the heater head was held at different temperatures ranging from 200°C to 800°C. The maximum temperature of 800°C was chosen because the insulation on the electric heater leads began to melt at elevated temperatures. With a burner instead of electric heaters, it is predicted that the thermocompressor could operate with a hot side temperature of 1000°C. Figures 6.10 and 6.11 below show the measured and predicted cold chamber pressure swings. The pressure swing was calculated by allowing the thermocompressor to reach steady state operation and taking the difference between the maximum and minimum pressure. For each temperature and frequency, measurements were taken by averaging three cycles. As shown in Figures 6.8 and 6.9, there is very little cycle to cycle variation, with the variation consistently under 10%.

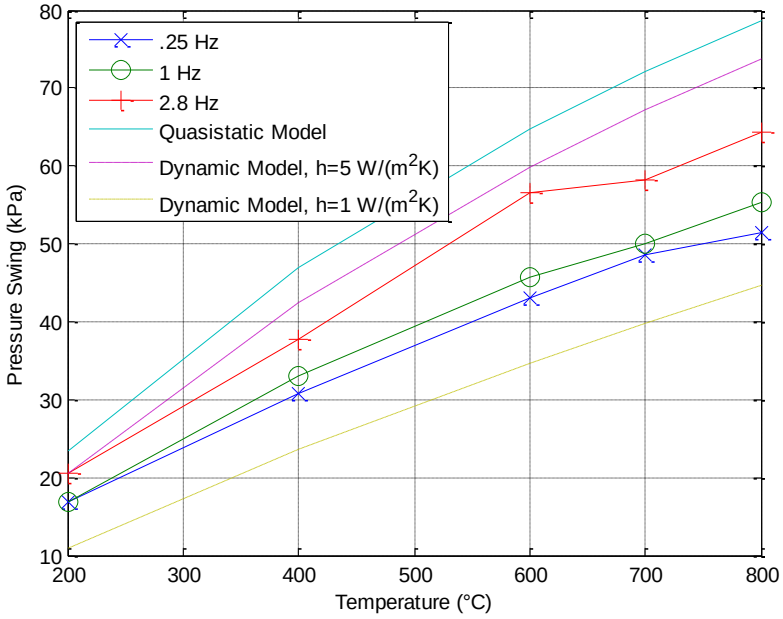

Figure 6.10 - Cold chamber pressure from experimental data at different operational frequencies and different models with heat exchangers

It can be observed from this figure that the pressure swing increases with increased frequency of operation. This is most likely due to a leak, because at higher frequencies there would be less time for the air to escape the thermocompressor. With a heat transfer coefficient of 5 W/m^{2}K the dynamic model generates a pressure swing that is close to the quasi-static model. This implies that with sufficient surface area for heat transfer, the heat transfer coefficient can be quite low. Conversely, Figure 6.11 shows that with a heat transfer coefficient of 100 W/m^{2}K, there is significant deviation from the quasi-static model, indicating a deficiency in the required heat transfer surface area.

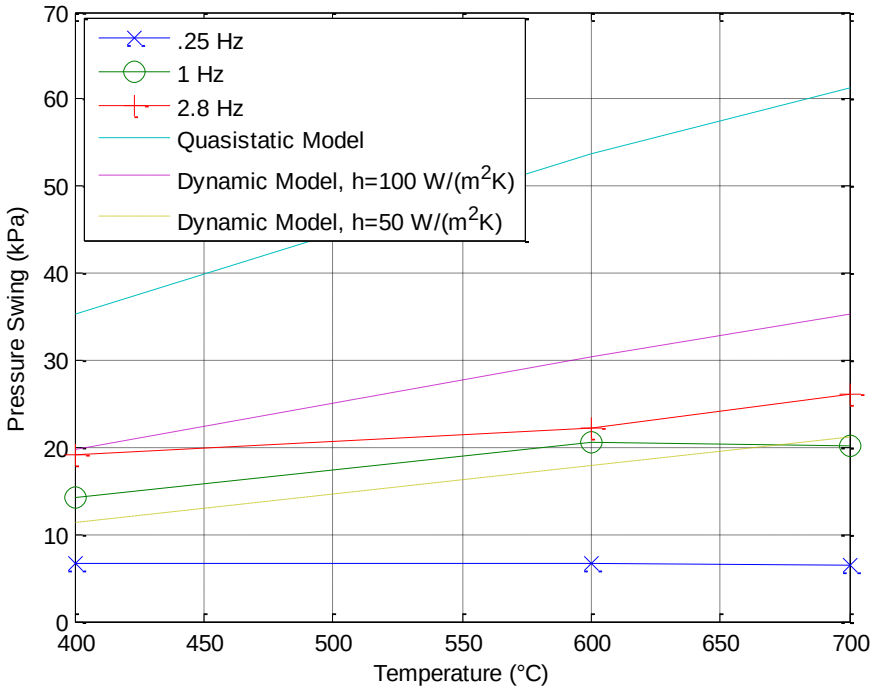

Figure 6.11 - Cold chamber pressure from experimental data at different operational frequencies and different models without heat exchangers

VII. Predicted Performance from Dynamic Model

The full benefits of the additional surface area provided by the heat exchangers with regard to further increasing the operational frequency were difficult to demonstrate experimentally because the frequency could not be increased above 2.8 Hz. Figure 6.12 utilizes the model described in Equations 3 and 4 to predict that higher heat transfer capabilities would allow greater pressure ratios at higher frequencies. This increased level of heat transfer can be used to increase the power output of the thermocompressor because more air can be pumped per cycle.

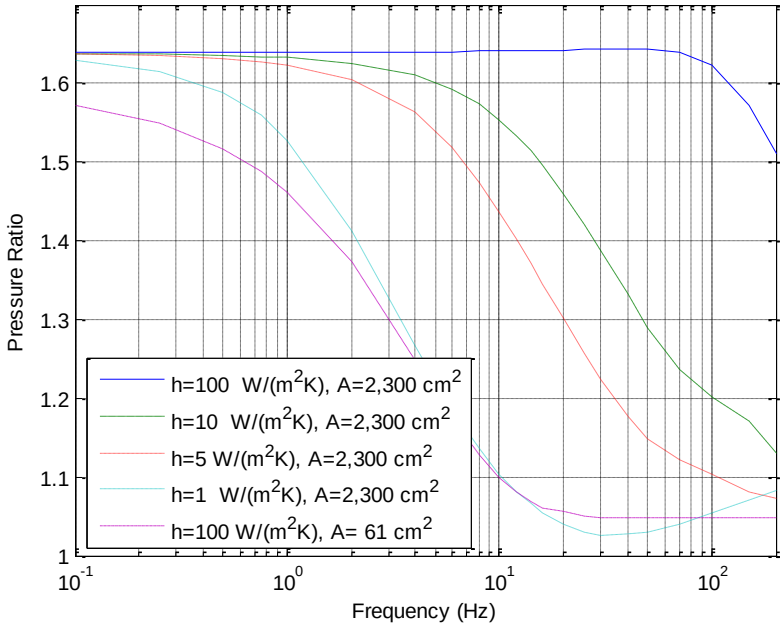

Figure 6.12 - Pressure increase from atmosphere for different heat transfer rates and operational frequency

The dynamic model is now extended to the case of pumping (mass transfer) to predict the performance of the device if it were allowed to pump. The energy produced per cycle is calculated using the following:

$$E_{pneum} = P_{res} V \ln\left(\frac{P_{res}}{P_{atm}}\right) \tag{9}$$

Utilizing the ideal gas law, the mass pumped per stroke can be described by Equation 10:

$$m_{pumped} = \frac{V}{R}\left(\frac{P_{atm}}{T_{low}} - \frac{P_{res}}{T_{high}}\right) \tag{10}$$

By combining Equations 9 and 10 and multiplying by the frequency of operation, the pneumatic power available for a given reservoir pressure can be described by the following:

$$P_{pneum} = m_{pumped} R T_{low} \ln\left(\frac{P_{res}}{P_{atm}}\right) f \tag{11}$$

Figure 6.13 below shows the pneumatic power output calculated by Equation 11 for differing frequencies of operation and different levels of heat transfer.

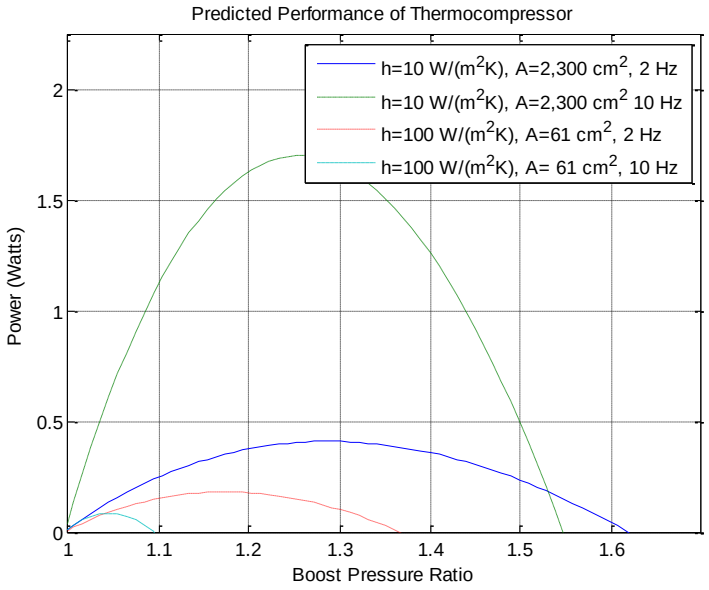

Figure 6.13 - Pneumatic power delivered as a function of the ratio of reservoir pressure (pumping pressure) to the low presure of the engine (suction pressure), for different heat transfer rates and operational frequencies

Figure 6.13 demonstrates that increasing the heat transfer area raises the amount of pneumatic power. It also shows that unless adequate heat transfer is provided, an increase in operational frequency may not increase the amount of power delivered. Figure 6.13 also shows that there is an optimal boost pressure ratio to maximize the power output.

VIII. Conclusions

In this paper the design and operation of a prototype, high heat transfer, Stirling thermocompressor is described. The implementation of novel, deformable, large surface area, low dead volume, in-piston heat exchangers is described. Experimental data from the thermocompressor is compared with two models. One model is dynamic and takes mass flow restrictions and heat transfer limitations into account. The other model is quasi-static, derived from the ideal gas law, and assumes that mass flow is unrestricted and that the control volumes inside the thermocompressor are isothermal.

The models match experimental data, but there is some disagreement, possibly due to an air leak in the thermocompressor. The presence of this leak would describe why experimentally higher operational frequencies result in larger pressure swings while the model predicts the opposite (Figures 6.10 and 6.11). Future efforts will seek to remove this leak, increase the

coefficient of heat transfer for the collapsible heat exchangers by preventing them from clumping, implement check valves, and refine the dynamic model.

It is demonstrated that higher rates of heat transfer are capable of producing larger pressure swings in the working fluid, and that the in-piston heat exchangers are capable of adding to this heat transfer capability.

Acknowledgement

This work was supported by the Center for Compact and Efficient Fluid Power, an NSF Engineering Research Center, grant EEC-0540834.

References

[1i] J. C. Moise et al., Thermocompressor Powered Artificial Heart Assist System, Proceedings of the 12th IECEC, Paper No. 779017, pp. 112-118, 1977.

[2i] P. Arquès, "Piston movement in thermocompressor", Proceedings of 32nd Intersociety Energy Conversion Engineering Conference, vol. 2, pp. 1003-1008, 1997.

[3i] M. J. Edwards, "Design, Modeling, and Performance of Miniature Reciprocating Thermocompressor", M.S. thesis, Department of Mechanical Engineering, Oregon State University, OR, 2005.

[1] K. A. Shorter et al., "A Portable Powered Ankle-Foot Orthosis for Rehabilitation", Journal of Rehabilitation Research and Development, vol. 48, No. 4, pp. 459-472, 2011.

[2] V. Bush, Apparatus for Compressing Gases, U.S. Patent No. 2,157,229, 1939.

[3] W. R. Martini et al., Development of a Simplified Stirling Engine to Power Circulatory Assist Devices, Proceedings of the 3rd IECEC, Paper No. 689102, pp. 733-749, 1968.

[4] W. R. Martini, The Thermocompresor and its Application to Artificial Heart Power, Proceedings of the 4th IECEC, Paper No. 69015, pp.107-114, 1969.

[5] B. M. Gibson et al., Bypass Gas Actuated Thermocompressor as an Implantable Artificial Heart Power Source, Proceedings of the 6th IECEC, Paper No. 719043, pp. 310-316, 1971.

[6] K. E. Buck et al., A Radioisotope-Power Stirling Engine for Circulatory Suport, Proceedings of the 3rd IECEC, Paper No. 689101, pp. 723-732, 1968.

[7] J. C. Moise et al., Development of a Thermocompressor Power System for Implantable Artificial Heart Application, Proceedings of the 8th IECEC, Paper No.739152, pp. 511-535, 1973.

[8] J. C. Moise et al., Status of a Thermocompresor Powered Implantable Artificial Heart System, Proceedings of the 9th IECEC, Paper No. 749118, pp. 799-804, 1974.

[9] J. C. Moise et al., Thermocompresor Powered Artificial Heart Assist System, Proceedings of the 10th IECEC, Paper No. 759183, pp. 1242-1245, 1975.

[10] J. C. Moise et al., Thermocompressor Powered Artificial Heart Assist System, Proceedings of the 11th IECEC, Paper No. 769024, pp. 150-156, 1976.

[11] J. C. Moise et al., Thermocompressor Powered Artificial Heart Assist System, Proceedings of the 12th IECEC, Paper No. 779017, pp. 112-118, 1977.

[12] J. A. Schneider et al., A Miniature TES Powered Stirling- Cycle Engine, Proceedings of the 19th IECEC, Paper No. 84918, p. 1917-1922, 1984.

[13] A. A. Kornhauser, "Analysis of an Idealized Thermocompressor", Proceedings of 31st IECEC, Paper No. 96422, pp. 1331-1336, 1996.

[14] P. Arquès, "Piston movement in thermocompressor", Proceedings of 32nd Intersociety Energy Conversion Engineering Conference, vol. 2, pp. 1003-1008, 1997.

[15] E. W. Beans, "A mathematical model for the Stirling engine cycle", Journal of Engineering for Power, vol. 103, pp. 505, 1981.

[16] D. M. Berchowitz et al., "A numerical model for Stirling cycle machine", Journal of Engineering for Power, vol. 102, pp. 757, 1980.

[17] H. Karabulut, "Thermodynamic Analysis of Bush Engine", G.U. Journal of Science, pp. 135-144, 2003.

[18] M. J. Edwards, "Design, Modeling, and Performance of Miniature Reciprocating Thermocompressor", M.S. thesis, Department of Mechanical Engineering, Oregon State University, OR, 2005.

[19] D. J. Yarger et al., "Experimental Study of a Mesoscale Two-Phase Thermocompressor", Paper presented at the 4th International Energy Conversion Engineering Conference, San Diego, CA, 2006.

[20] J. A. Riofrio, "Design, Modeling and Experimental Characterization of a Free Liquid-Piston Engine with separated combustion chamber", Ph.D. dissertation, Department of Mechanical Engineering, Vanderbilt University, TN, 2008.

[21] L. Tian et al., "Miniature HCCI Free-Piston Engine Compressor for Orthosis Application", Proceedings of JSAE/SAE Small Engine Technology Conference 2009, Nov 3-5, 2009, Penang, Malaysia.

[22] J. A. Willhite, C. Yong, and E. J. Barth. "The high inertance free piston engine compressor part 2: design and experimental evaluation," *ASME Journal of Dynamic Systems, Measurement and Control*. In Press

[23] M. Raibert et al., "BigDog, the Rough-Terrain Quadruped Robot", Proceedings of the 17th IFAC World Congress, 2008:17-1:10822-10825.

[24] J. D. Van de Ven et al., "Developments towards a liquid piston Stirling engine", Proceedings of the 6th International Energy Conversion Engineering Conference, Paper #5635, 2008.

[25] V. D. N. Rao, Heat exchanger for Stirling engine, U.S. Patent No. 4,183,213, 1980.

[26] M. Fujiwara et al., Heat exchanger for a Stirling engine, U.S. Patent No. 4,662,176, 1987.

[27] N. Hirao et al., “Improvement in specific power of Stirling engine by using a new heat exchanger”, Journal of the Japan Institute of Energy, vol. 88, pp. 1095-1100, 2009.

[28] Grinnell, S.K., “Flow of a Compressible Fluid in a Thin Passage”. ASME, 16 pages, 1954.

[29] Schmidt, G. "The Theory of Lehmann's Calorimetric Machine," Z. Ver. Dtsch. Ing, vol. 15, part 1

7. Conclusion

Summary

The major contribution of this work is the unique design and control of three energy conversion devices. A prototype bridge vibration energy harvester, free-piston engine compressor, and Stirling thermocompressor were modeled, designed and constructed. Each device was fully instrumented and experimental data was produced to validate its dynamic model and evaluate its performance.

Although these projects differ in many important ways, this dissertation described how to cast widely different energy conversion devices into a common impedance matching framework. The three energy conversion devices were presented and described in terms of this framework. Each device emphasized different aspects of the three major conceptual components of this approach: the energetic source, the source impedance and the load impedance. By considering the relevant conceptual components for each device, insights were gained into the fundamental mechanisms needed to transfer energy across energetic domains.

The steps taken for the projects described in this document could be applied to a great number of energy conversion devices. The first step in applying this framework is to create a simplified dynamic model of the system so that a bond graph can be used to concisely show the transfer of energy between components. Although converting the system dynamics into bond graph form requires simplification of complex dynamics, this form is useful because the barriers to fast and efficient energy transfer can be quickly identified. In this form it is clear where energy crosses energetic domains, which is where major bottlenecks are likely to occur. In this form it also becomes clear that the project's dynamics can be logically separated into common components. By converting the system to a Thevenin type electrical circuit, fundamental goals of the device become clear and decisions pertaining to active control or physical design can intelligently be made.

With some the energy conversion dynamics separated into an exogenous voltage source, this energetic source can be maximized without affecting the other dynamics. The components comprising the energy transporting source impedance can then be modified to properly mate the energy source to its intended destination. In some cases one or all three of the conceptual components are fixed and do not permit enhancement through design or control. In this instance it is important to identify these components' dynamics so that its adjacent components can accommodate it.

Contribution

As summarized above, this work describes the design and control of energy conversion

devices. The key contributions for the five manuscripts are listed as follows:

Bridge Vibration Energy Harvester

Manuscript 1 (Chapter 2): From: *Experimental Research Platform for Structural Health Monitoring*, Babjak, B., Szilvasi, S., Pedchenko, A., Hofacker, M., Barth, E. J., Volgyesi, P., & Ledeczi

- Presentation of prototype bridge vibration energy harvester
    - Compliant mechanisms utilized as low friction 1-DOF mechanism
    - Linear motor used for power generation, active control, and as proof mass
    - Fully instrumented with linear potentiometer, encoder, and accelerometer, servo amps, and data acquisition
- Derived control using the maximum power transfer theorem for simplified harvester
    - Validated in simulation and experimentally
    - Enables the collection of the maximum amount of available power across a broad spectrum of frequencies
    - Cancels complex part of harvester's impedance by eliminating inertial and stiffness elements

Manuscript 2 (Chapter 3): *Multi-Domain Impedance Matching Applied to a Bridge Vibration Energy Harvester*, Hofacker, M, Pedchenko, A, Barth, E. J.

- Determined canonical control law for a revised bridge vibrational energy harvester prototype
    - Verified analytically and in simulation
- Found control law to approximate ideal behavior
    - Stable, causal controller
    - Found through constrained optimization
    - Shown in simulation to produce significantly more power than passive canonical alternative

Free-Piston Engine Compressor

Manuscript 3 (Chapter 4): Design and Validation of a Figure-Eight Free-Liquid-Piston Engine Compressor for Compact Robot Power, Barth, E. J., Hofacker, M, Kumar, N, and **Manuscript 4 (Chapter 5)**: An Experimentally Validated Figure-Eight Free-Liquid-Piston Engine Compressor, Hofacker, M, Kumar, N, Barth, E. J.

- Presentation of functional third generation prototype free-piston engine compressor
    - Standalone device with onboard data acquisition, control, and voltage regulation
    - Constructed custom printed circuit boards for signal conditioning and voltage regulation

- Figure-8 Configuration
    - Demonstrated using Reynolds' transport theorem value of figure-8 configuration to balance device
- Compressor Head Improvements
    - Developed metric to determine check valve performance
    - Constructed compressor head to accommodate new check valve
- Experimental Results
    - Developed a finite state control scheme that utilizes the pumping chamber pressure as an indicator of liquid piston position
    - Achieved consistent combustion across a wide range of reservoir pressures
    - Demonstrated 60% increase in pumping pressure over previous devices

Controlled Stirling Thermocompressor

Manuscript 5 (Chapter 6): Dynamic Simulation and Experimental Validation of a Single Stage Thermocompressor for a Pneumatic Ankle-Foot, Hofacker, M, Kumar, N, Barth, E. J.

- Presentation of functional prototype Stirling Thermocompressor
    - Novel design utilizing reciprocating lead screw and electric motor
    - Design experimentally shown to be capable of withstanding extremely high temperatures (up to 800°C)
- Modeled pressure dynamics
    - Dynamic and quasi-static models compared against experimental data
- Presentation of novel in-cylinder heat exchangers
    - Shown experimentally to dramatically increase rates of heat transfer by an order of magnitude

It is the author's hope that each of the research projects discussed is a valuable contribution to their respective field and that together they provide a unique and useful lens through which to view energy conversion devices.